

Politecnico di Torino

ScuDo
Scuola di Dottorato ~ Doctoral School
WHAT YOU ARE, TAKES YOU FAR

Doctoral Dissertation
Doctoral Program in Materials Science and Technology (35^{th}cycle)

Unraveling CO_2 Reduction Mechanisms on Selective Electrocatalysts: Computational Insights for Efficient Valorization

By

Clara Salvini

******

Supervisors:
Prof. Giancarlo Cicero, Supervisor
Dr. Michele Re Fiorentin, Co-Supervisor
Dr. Angelica Chiodoni, Co-Supervisor

Politecnico di Torino
2023

Declaration

I hereby declare that, the contents and organization of this dissertation constitute my own original work and does not compromise in any way the rights of third parties, including those relating to the security of personal data.

Clara Salvini
2023

* This dissertation is presented in partial fulfillment of the requirements for **Ph.D. degree** in the Graduate School of Politecnico di Torino (ScuDo).

Acknowledgements

I would like to thank Prof. Giancarlo Cicero for his guidance during my academic path, Michele Re Fiorentin and Francesca Risplendi, whose advice and knowledge helped me grow in the world of scientific research.

I would also like to thank the Istituto Italiano di Tecnologia, and in particular Angelica Chiodoni, for giving me the opportunity to have this great experience and Prof. Hannes Jonnson of the University of Iceland for allowing me to spend several months under his supervision working with his research group.

Finally, I wish to acknowledge my family, and particularly my parents for the love and support I have gotten over the years.

Contents

Nomenclature viii

Introduction xii

1 Electrochemical CO_2 Conversion for Sustainable Chemicals and Fuel Production 1

1.1 Global warming and the role of carbon capture and conversion . . . 1

1.2 Electrochemical CO_2RR as a strategy to mitigate global warming . . 4

1.2.1 Fundamentals of electrochemical CO_2RR 5

1.2.2 The role of the electrocatalyst in CO_2RR 7

1.2.3 Assessing CO_2RR efficiency and selectivity 10

1.3 Classes of electrocatalysts for CO_2RR 11

1.3.1 Metal- and metal-oxide based catalysts 12

1.3.2 Metal-organic frameworks 15

1.4 The role of theoretical modelling in electrocatalysis 16

2 Methods for theoretical calculations 18

2.1 The many-body Hamiltonian and the Born-Oppenheimer approximation 18

2.2 Density Functional Theory 20

2.2.1 The Hohenberg-Kohn theorems 21

2.2.2 The Kohn-Sham equations . . . 22
2.2.3 Approximations to the exchange-correlation functional . . . 25
2.3 The Hellmann-Feynman theorem . . . 26
2.4 Aspects of DFT implementation . . . 27
2.4.1 Basis set . . . 27
2.4.2 Pseudopotentials . . . 29
2.5 Applying DFT to chemical reactions . . . 31
2.5.1 Exploring the potential energy surface . . . 32
2.5.2 Thermodynamic properties . . . 34
2.5.3 Theoretical approach to reaction kinetics . . . 39
2.5.4 Constant electrode potential . . . 42

3 Understanding the Active Surface Structure of SnO_2 Electrocatalyst for CO_2 Reduction 44

3.1 SnO_2 electrocatalyst for CO_2 reduction to HCOOH . . . 45
3.2 The SnO_2 active surface structure: a matter of debate . . . 46
3.3 Surface free energy analysis of low-index SnO_2 surfaces . . . 48
3.4 Possible electrocatalytic reduction reactions at the SnO_2(110) surface 50
3.5 The self-reduction of SnO_2(110) surface . . . 52
3.6 CO_2RR and HER at under-stoichiometric SnO_2 surfaces . . . 55
3.7 Conclusions . . . 57

4 Imidazole-Imidazolate Pair in ZIF-8 for CO_2 Capture and Conversion 60

4.1 ZIF-8 electro-organocatalyst for CO_2 capture and conversion . . . 61
4.2 Investigation of ZIF-8(110) surface terminations . . . 63
4.3 Designing carbon nanotube supported ZIF-8 electrocatalyst . . . 65
4.4 Elctrochemical CO_2RR on ImH/Im^- sites . . . 68

4.5 CO_2RR and HER on undercoordinated Zn metal center 71

4.6 Synthesis and electrochemical performace of ZIF-8 electro-organcatalyst guided by DFT predictions 72

4.7 Conclusions 76

5 Voltage-Dependent Activation Energy of CO_2RR on Ag and Zn Surfaces 78

5.1 CO_2RR and the binding energy of CO on Ag and Zn surfaces 78

5.2 Previous work on CO_2RR on Ag and Zn electrocatalysts 80

5.3 Thermodynamic investigation of CO_2RR on Ag and Zn low-index surfaces 81

5.4 Reaction mechanisms 83

5.5 Voltage-dependent activation energy calculations 86

5.5.1 Comparison between the Tafel and Heyorvsky mechanisms for CO_2RR 87

5.5.2 Kinetic barriers of the Volmer-Heyrovsky mechanism for HER 92

5.6 Conclusions 94

Conclusions 98

Bibliography 98

Appendix A Theoretical methods 119

A.1 CO_2, CO and OCO-molecules energy correction 119

A.2 Evaluation of solvation energy 122

A.3 Computed chemical potential of polyatomic molecules 122

A.4 Calculation of surface phase diagram 123

A.5 Calculation of relative surface energy stability 125

Appendix B Computational details 126

B.1 Quantum ESPRESSO and VASP software 126
B.2 Calculation of SnO_2 surfaces 127
B.3 Calculation of ZIF-8 and ZIF-8/CNT 129
B.4 Calculation of metal Ag and Zn surfaces 130

Nomenclature

Acronyms / Abbreviations

ΔG	Gibbs free energy difference
η	Overpotential
γ	Surface energy
μ_{O}	Oxygen chemical potential
C_p	Heat capacity at constant pressure
E^{DFT}	DFT ground-state electronic energy
E^{solv}	Solvation energy
E^{ZP}	Zero-point energy
FE	Faradaic efficiency
G	Gibbs free energy
j	Current density
S	Entropy
SCF	Self-consistent field
U_0	Equilibrium potential
U_{ext}	Applied potential
U_{onset}	Onset potential

*COOH CO_2RR carbon-bound intermediate

*OCHO CO_2RR oxygen-bound intermediate

*OCOOH Bicarbonate intermediate

*OH Hydroxyl intermediate

$(H^+ + e^-)$ proton/electron pair

C_2H_4 Ethylene

C_2H_5OH Ethanol

C_{sp^2} sp^2 carbon atom

CH_3OH Methanol

CH_4 Methane

$CO_2^{\bullet -}$ CO_2 radical anion

CO_2 Carbon dioxide

CO_2RR CO_2 reduction reaction

CO Carbon monoxide

H_2CO_3 Carbonic acid

H_2 Hydrogen gas

$HCOO^-$ Formate

HCOOH Formic acid

Im^- Imidazolate

ImH Imidazole

O_2 Molecular oxygen

O_{br} Bridging oxygen

O_{in-pl} In-plane oxygen

SnO_2 Tin dioxide

V_O Oxygen vacancy

C1 Single carbon

CEP Constant electrode potential

CHE Computational Hydrogen Electrode

CNT Carbon nanotube

DFT Density Functional Theory

GGA Generalized Gradient Approximation

GHG Greenhouse gases

HCAs Hydrocarbons

HER Hydrogen Evolution Reaction

IL Ionic liquid

LDA Local Density Approximation

M-O Metal oxide

MEP Minimum energy path

MOF Metal–Organic Framework

MWCNT Multi-Walled Carbon NanoTube

NEB Nudged elastic band

OER Oxygen evolution reaction

PBE Perdew-Burke-Ernzerhof

PDOS Projected Density of States

PES Potential energy surface

PET Proton-electron transfer

PP pseudopotential

PW Plane Wave

PWscf Plane-Wave Self-Consistent Field

QE QUANTUM ESPRESSO

RHE Reversible Hydrogen Electrode

SAC Single-Atom Catalyst

SHE Standard Hydrogen Electrode

TOF Turnover frequency

TS transition state

VASP Vienna *Ab-initio* Simulation Package

ZIF Zeolitic imidazolate framework

Introduction

Over the past century, anthropogenic emissions have caused a significant increase in the concentration of CO_2 in the atmosphere, pushing the planet towards an environmental catastrophe. This crisis has motivated the search for sustainable strategies that reduce CO_2 emissions and recycle it into valuable products. Scientists are confronted with the daunting challenge of converting CO_2 into chemicals and fuels without relying on fossil fuels but rather opting for alternative routes that are efficient, cost-effective, and environmentally sustainable.

The electrochemical reduction of CO_2 offers a promising pathway towards achieving carbon neutrality. Compared to other CO_2 reutilization strategies, this technology shows enhanced efficiency and selectivity and can be combined with renewable energy resources, thereby reducing dependence on fossil fuels. However, the primary challenge in this approach is to develop robust, active, and selective electrocatalysts for the CO_2 Reduction Reaction (CO_2RR). As a result, significant research efforts have been directed towards designing novel electrocatalysts that operate at low overpotentials, produce desirable products, and prevent competitive side reactions, such as the hydrogen evolution reaction (HER).

Understanding the structure-reactivity-selectivity relationship for a given electrocatalyst is challenging, as the process occurs at the interface between the solid electrode and the liquid electrolyte. To gain more insights into CO_2RR, electronic structure calculations based on Density Functional Theory (DFT) have proven to be indispensable. They allow for the analysis, elucidation, and guidance of experimental research in synthesizing materials that possess the ideal characteristics for CO_2 conversion at the atomic level.

In this thesis, DFT has been utilized as a powerful tool to understand and predict the physicochemical properties of electrocatalysts and the CO_2RR mechanism occurring at their surfaces. The approach has demonstrated that electronic structure calculations can work in synergy with experiments. The primary goal of this work has been to provide answers to open questions arising from experimental evidence and to offer guidelines for the development of efficient and selective catalysts. To achieve this, the thesis investigates both the thermodynamic and kinetic aspects of CO_2RR using electronic structure calculations combined with thermodynamics and rate theory.

The first part of this thesis presents a thermodynamic study of two electrocatalysts, SnO_2 and ZIF-8, which are known to selectively reduce CO_2 into formic acid (HCOOH) and carbon monoxide (CO), respectively. The surface structure of SnO_2 electrocatalysts during CO_2RR remains a topic of debate. This work provides new insights into this question by applying DFT, supplemented by atomistic thermodynamics, to investigate the stability under operating conditions of SnO_2 surfaces with varying degrees of reduction and analyzing their relative CO_2RR performances. In the case of ZIF-8 electrocatalysts, our computational investigation aimed to predict the active site and mechanism for the conversion of CO_2 to CO. Our thermodynamic study challenged the widely held view in the literature that the metal atom is the key reaction active site, instead highlighting the crucial role played by the organic ligand and the surface termination. The results of our study provided valuable guidelines for the experimental synthesis of ZIF-8.

A thermodynamic model alone provides useful insights into electrocatalysis, but offers an incomplete understanding of the reaction mechanism because it disregards reaction kinetics. For example, according to thermodynamics, Ag and Zn metal electrodes are expected to produce HCOOH and H_2, respectively, while experiments demonstrate that these metals have a high selectivity towards CO. Therefore, the final part of the thesis aims to comprehend how kinetics influences the selectivity of Ag and Zn metal electrodes. We estimated the activation energy for both CO_2RR and competitive HER as a function of applied potential, allowing us to determine the reaction pathway that occurs on the surface of Ag and Zn electrocatalysts.

The thesis is organised as follows. In Chapter 1, an introduction to the principles of electrochemical CO_2 conversion is given and the main classes of catalysts are

presented. In Chapter 2, DFT and the theoretical approaches employed throughout the thesis are discussed. The understanding of the active surface structure of SnO_2 towards CO_2 reduction to HCOOH is analyzed in Chapter 3. Chapter 4 discusses the mechanism of CO_2 capture and reduction on ZIF-8 electrocatalysts. Finally, Chapter 5 presents an investigation of the selective CO_2 conversion to CO on Ag and Zn metal electrodes from a kinetic perspective. Conclusions are presented in the final Chapter.

CHAPTER 1

Electrochemical CO_2 Conversion for Sustainable Chemicals and Fuel Production

In this Chapter, we present an overview of the electrochemical CO_2 reduction reaction (CO_2RR) and its possible role in mitigating global warming and climate change. In Section 1.1, we first discuss the advantages of an electrochemical approach to decrease the amount of CO_2 in the atmosphere compared to other technological solutions, then we discuss the basics principle of the electrochemical conversion in Section 1.2 focusing in particular on the key role of the electrocatalyst discussed in Section 1.3. Finally, in Section 1.4, we briefly introduce the role of theoretical calculations in the development of selective and efficient catalysts for CO_2RR and present the aim and subject of this thesis work.

1.1 Global warming and the role of carbon capture and conversion

Nowadays, one of the most urgent environmental issues is global warming, which refers to the long-term trend of increasing average global temperature, primarily caused by human activities, which release large amounts of greenhouse gases (GHG)

into the atmosphere [1]. Indeed, since the time of the industrial revolution until today, fossil fuel burning for industrial needs, together with deforestation and land exploitation and transformation, has caused the accumulation of carbon dioxide (CO_2) in the atmosphere, one of the major greenhouse effect gases. CO_2 emissions are a significant contributor to global warming since they trap heat in the Earth's atmosphere, leading to an increase of the planet's overall temperature. As more CO_2 and other greenhouse gases accumulate in the atmosphere, they form a layer that traps more heat, leading to rising temperature, changing weather patterns, and other impacts on the environment, such as sea-level rise, increased frequency of extreme weather events, and the loss of biodiversity. In 2021 the concentration of CO_2 in the atmosphere reached to 415 part per million (ppm), i.e. 45 % larger than the concentration before the advent of the industrial revolution and 31% larger than 60 years ago. If the global CO_2 emission continues at the level of the last few years, its atmospheric concentrations will reach 500 ppm by the end of this century, nearly double the preindustrial one (280 ppm) [2, 3]. The problem is further complicated because GHG remain in the atmosphere for a long time, having long lasting effects. The graph reported in Figure 1.1 clearly shows the exponential growth of CO_2 emissions after the advent of the industrial revolution.

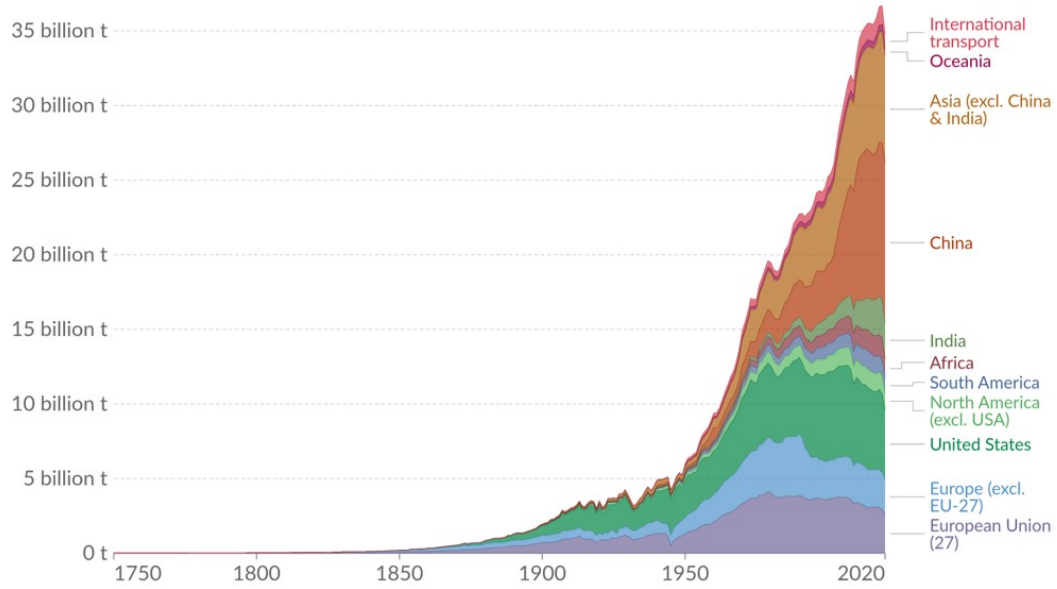


Figure 1.1 Annual CO_2 emissions from fossil fuels by world region, taken from Ref.[4].

Reducing CO_2 emissions is critical in addressing global warming and mitigating its impacts. The long-term solution would consist in a 'decarbonizing' industrial revolution towards affordable, accessible and ecological sources of energy. This could be achieved by promoting cleaner and more efficient energy sources, such as solar, wind, and geothermal power, improving energy efficiency in buildings, industry, and transportation, and adopting sustainable land-use practices to reduce deforestation and promote afforestation. In the short term, CO_2 could be captured, stored and transformed into added-value fuels and chemicals such as hydrocarbons (HCAs). This approach would reduce the dependence on newly extracted fossil fuels, and would represent an important step towards achieving a Circular Economy. To date, several strategies for converting CO_2 into useful products have been proposed in the literature, in particular:

- *Electrochemical conversion*, which consists of using an electrical current to convert CO_2 into chemicals, such as formic acid, methane, and carbon monoxide [5, 6]. This process should use renewable energy sources, such as solar or wind power, to power the electrochemical reaction.
- *Biological conversion*, which employs microorganisms, such as bacteria or algae, to convert CO_2 into useful products, such as biofuels, chemicals, and food products [7]. For example, algae can be grown in photobioreactors and used to produce biofuels, while bacteria can be engineered to produce useful chemicals from CO_2 [8].
- *Mineralization*, which involves using naturally occurring minerals, such as olivine or serpentine, to react with CO_2 and form stable carbonates [9, 10]. This process can be used to permanently store CO_2 underground, reducing its impact on the environment.
- *Chemical conversion*, which exploits chemical reactions to convert CO_2 into useful products, such as plastics, polymers, and building materials [11]. For example, CO_2 can be reacted with ethylene oxide to produce polyethylene carbonate, which can be used to make plastics and other materials [12].

To date, all strategies proposed to convert CO_2 suffer from certain drawbacks, such as high energy demands for activating CO_2 molecules and low conversion rate. Overall,

electrochemical conversion, the subject of this thesis work, offers several advantages, making it a promising approach for mitigating the impacts of global warming and reducing GHG emissions [13]. However, more research and development are needed to optimize the process and make it economically viable for widespread use.

In the following sections, we will present the basic principles of electrochemical CO_2 conversion, specifically focusing on its main advantages over alternative conversion routes and on the key role played by electocatalyst on the overall process efficiency.

1.2 Electrochemical CO_2RR as a strategy to mitigate global warming

Electrochemical CO_2 conversion powered by renewable energy sources is considered to be an attractive approach to mitigate climate change. Electrical energy is supplied to establish a potential difference between two electrodes, inducing CO_2 reduction to value-added chemicals under mild conditions. The great interest in the continuous development and implementation of electrochemical technologies is due to some exceptional advantages that this strategy inherently brings with it [14]. First, the electrocatalytic CO_2RR allows to obtain several chemicals and fuels by a multi-electron transfer process, performing as a versatile and efficient route to reduce CO_2 emissions, create value from waste streams and face the environmental and energy crisis. The electrochemical conversion of CO_2 can selectively produce valuable products by working at room temperature and choosing proper operative conditions, such as electrodes, applied external potential, electrolyte, solvent, pH, temperature and pressure. By controlling these conditions, electrochemical conversion has the potential to be highly efficient, with conversion rates of up to 99%. Moreover, as mentioned earlier, to reduce both the cost of the overall process and the environmental impact, the electric driving force required for CO_2RR can be coupled with renewable sources without any additional fossil fuel-based electric power. Finally, electrochemical conversion can be scaled up for industrial use, with large-scale electrochemical reactors being developed for CO_2 conversion [15].

1.2.1 Fundamentals of electrochemical CO_2RR

CO_2 reduction reaction takes place in an electrochemical cell or electrolyzer. The latter contains two electrodes, a cathode and an anode, immersed in a solution of salt electrolytes, which allows a rapid transport of ions. The two electrodes are typically in two different compartments linked by a salt bridge or, otherwise, an ion conducting membrane. In electrochemical cells, the two half-cell reactions, that is oxidation and reduction, occur simultaneously. More precisely, at the anode, a species is oxidized and releases electrons to the species at the cathode, where it is reduced by the electron transfer. In a CO_2RR cell, water oxidation to molecular oxygen (O_2), also known as oxygen evolution reaction (OER), occurs at the anode, whereas CO_2 is reduced to added value products [16] at the cathode. During the electrolytic reaction, ions are transported across the membrane from one side to the other and electrons travel through the external circuit. A reference electrode is usually used for potential measurement. Typical electrochemical cell configurations for CO_2RR (*H-type cell* [17] and *Flow cell* [18] electrolyzers) are schematically reported in Figure 1.2.

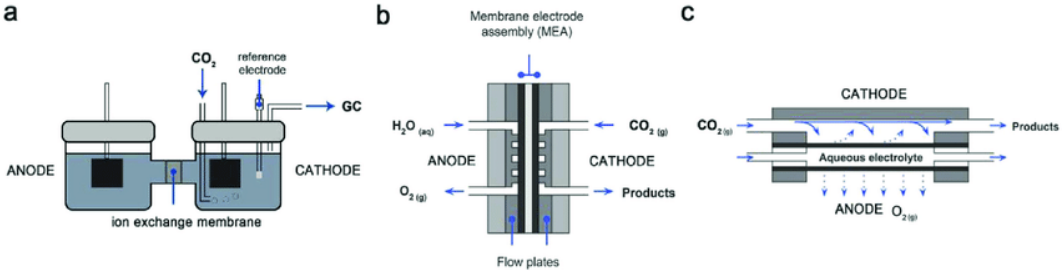


Figure 1.2 Schematic representation of common CO_2 electrolyzers: (a) H-type electrochemical cell, (b) and (c) flow-cells. Figure taken from Ref.[19].

An important parameter, that has to be considered when performing an electrolytic CO_2 transformation, is the thermodynamic electrochemical potential of CO_2 reduction, since it affects the selectivity and efficiency of CO_2 conversion to value-added chemicals. The selectivity of CO_2 reduction refers to the ability of the electrochemical system to convert CO_2 into a specific desired product, such as methane, ethylene, or formic acid, while minimizing the formation of unwanted byproducts, such as hydrogen. The electrochemical potential also relates to the amount of energy required to reduce CO_2 to a desired product, and it depends on

the specific reaction pathway followed during the reduction. A reaction occuring at a higher electrochemical potential typically requires more energy input, which can lead to lower energy efficiency and higher cost. In a CO_2RR process, it is important to minimize the electrochemical potential while maintaining high selectivity towards desired products.

Table 1.1 Theoretical electrochemical potentials of CO_2 reduction half reaction versus Standard Hydrogen Electrode (SHE), at pH 7, at 25 °C, 1 atm and 1.0 M concentration of other solutes.

Possible half-reactions of electrochemical CO_2 reduction	Electrode potentials (V vs SHE) at pH 7
$2H^+ + 2e^- \rightarrow H_2$	-0.41
$CO_2 + e^- \rightarrow {}^{\bullet}CO_2^-$	-1.90
$CO_2 + 2H^+ + 2e^- \rightarrow HCOOH$	-0.61
$CO_2 + H_2O + 2e^- \rightarrow HCOO^- + OH^-$	-0.43
$CO_2 + 2H^+ + 2e^- \rightarrow CO + H_2O$	-0.53
$CO_2 + H_2O + 2e^- \rightarrow CO + 2OH^-$	-0.52
$CO_2 + 4H^+ + 2e^- \rightarrow HCHO + H_2O$	-0.48
$CO_2 + 3H_2O + 4e^- \rightarrow HCHO + 4OH^-$	-0.89
$CO_2 + 6H^+ + 6e^- \rightarrow CH_3OH + H_2O$	-0.38
$CO_2 + 5H_2O + 6e^- \rightarrow CH_3OH + 6OH^-$	-0.81
$CO_2 + 8H^+ + 8e^- \rightarrow CH_4 + 2H_2O$	-0.24
$CO_2 + 6H_2O + 8e^- \rightarrow CH_4 + 8OH^-$	-0.25
$2CO_2 + 12H^+ + 12e^- \rightarrow C_2H_4 + 4H_2O$	+0.06
$2CO_2 + 8H_2O + 12e^- \rightarrow C_2H_4 + 12OH^-$	-0.34
$2CO_2 + 12H^+ + 12e^- \rightarrow C_2H_3CH_2OH + 3H_2O$	+0.08
$2CO_2 + 9H_2O + 12e^- \rightarrow C_2H_3CH_2OH + 12OH^-$	-0.33

In Table 1.1 the theoretical potentials versus Standard Hydrogen Electrode (SHE) at pH 7 for different CO_2 reduction products are reported. From an analysis of the reported values, it is apparent that different reduction products are characterized by similar thermodynamic reduction potentials. This highlights that when CO_2 is reduced at the cathode of an electrochemical cell, the process is not selective, since, at a given applied bias, several reaction products may be obtained at the same time depending on the number of electrons transferred [20]. High selectivity would mean that a high proportion of the reduced CO_2 is converted into a single desired product. This is an important aspect because unwanted by-products require additional separation and purification steps that are commercially unacceptable, and increase the cost of the final product [21]. Increasing CO_2RR selectivity is typically

achieved by covering the cathode with electrocatalyst materials which guide CO_2 reduction reaction towards a specific reduction product avoiding the formation of unwanted by-products [22]. The mechanism by which electrocatalysts increase selectivity is briefly summarized in the following section.

1.2.2 The role of the electrocatalyst in CO_2RR

Electrocatalytic CO_2RR requires the employment of electrocatalysts deposited on the cathodic side of the electrolizer. They can play a crucial role in increasing the selectivity, decreasing the overpotential, and speeding up the electrochemical reactions. Selectivity is achieved through the promotion of specific reaction pathways and the concurrent suppression of competing reactions that produce undesired byproducts. An example of such effect is given in Figure 1.3. The scheme illustrates how, under an applied external bias, some electrocatalysts favor the chemisorption of CO_2 through its oxygen atom while others induce molecular binding through its carbon atom. Once CO_2 is activated, its reduction proceeds towards the production of gaseous and liquid chemicals according to the number of proton/electron pairs, $(H^+ + e^-)$, transferred to the CO_2 [20]. The two most common reduction pathways lead to single carbon (C_1) products, such as formic acid (HCOOH)

$$CO_2 + 2\,(H^+ + e^-) \longrightarrow HCOOH \tag{1.1}$$

and carbon monoxide (CO)

$$CO_2 + 2\,(H^+ + e^-) \longrightarrow CO + H_2O. \tag{1.2}$$

In the first case, the reduction reaction typically proceeds with the evolution of HCOOH upon transfer of an $(H^+ + e^-)$ couple to the CO_2 and the formation of an oxygen-bond intermediate, *OCHO. In the second case, the reaction proceeds via the formation of a *COOH bound to the catalyst surface that is then transformed into CO by water elimination. Therefore, reactions (1.1) and (1.2) can be split in two steps [23],

$$CO_2 + (H^+ + e^-) \longrightarrow {}^*OCHO \tag{1.1.a}$$

$$^*OCHO + (H^+ + e^-) \longrightarrow HCOOH \tag{1.1.b}$$

and

$$CO_2 + (H^+ + e^-) \longrightarrow {}^*COOH \tag{1.2.a}$$

$${}^*COOH + (H^+ + e^-) \longrightarrow CO + H_2O \tag{1.2.b}$$

respectively. Moreover, once formed, CO can either desorb from the surface or be further reduced to form hydrocarbons, such as methane (CH_4) or multicarbon products as ethylene (C_2H_4) and alcohols, such as methanol (CH_3OH) and ethanol (C_2H_5OH) [23].
In the following sections we will show that metal electrocatalysts can be classified according to their main product [20]. For example, metals like Sn and Pb mainly generate HCOOH in aqueous solutions, while metals like Au, Ag, Zn tend to produce CO. In comparison, Cu is able to produce alcohols and hydrocarbons with CO being an intermediate.

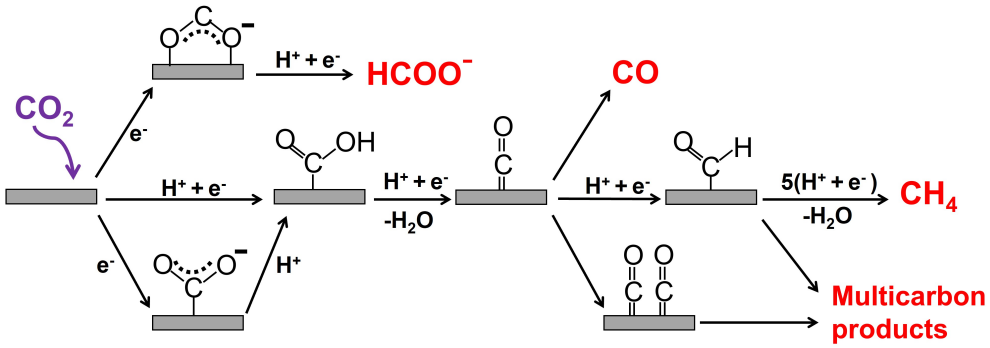


Figure 1.3 Scheme of electrochemical CO_2 reduction pathways toward different chemical products.

Electrocatalysts are also important since they typically decrease the overpotential, also known as overvoltage, which corresponds to the additional potential that must be applied to an electrochemical reaction beyond its thermodynamic value to achieve a desired current density or reaction rate. As noticeable from the values reported in table 1.1, in the case of CO_2 high overpotential values are mainly due to the initial activation of CO_2 molecule, i.e. the formation the carbon dioxide radical anion ($CO_2^{\bullet -}$), occurring at -1.90 V vs SHE [20]. This high overpotential can limit the energy efficiency and economic viability of CO_2RR technologies, as it requires large energy input to achieve the desired rate of CO_2 conversion. Moreover, a high

overpotential value can bring about side reactions and, consequently, unwanted products. An example of a process competing with CO_2RR is the the Hydrogen Evolution Reaction (HER), which leads to the generation of hydrogen gas (H_2) [24]

$$2\,(H^+ + e^-) \longrightarrow H_2, \tag{1.3}$$

and introduces a major challenge to achieve efficient and selective CO_2 electrochemical reductions. The overpotential can be significantly minimized by tuning the used electrocatalyst so that specific reaction intermediates are stabilized. In particular, a catalyst should reduce the activation barrier for CO_2RR with respect to HER, selectively leading to CO_2 conversion at low overpotential with high reaction rates.

In the last decades, several homogeneous [25] and heterogeneous catalysts [26] have been reported to promote the CO_2RR.

Homogeneous catalysis for electrochemical CO_2RR has been extensively studied [27] since the 1970s. In homogeneous catalysis, the electrocatalyst is a metal complex (molecular catalyst) in the same phase of the reactants and acts as a redox transfer between the electrode and CO_2. Catalysts belonging to this class take electrons from the electrode, donate them to CO_2 in solution, and return to the initial state [28].

Heterogeneous electrocatalysis has instead received much attention in recent years thanks to its low cost and eco-friendly properties [29]. In heterogeneous catalysis, the electrocatalyst is in the solid phase, the CO_2 is activated on the catalytic surface, it is reduced by proton-electron transfers (PET) and, eventually, the products are desorbed into the solvent [30]. Both catalytic approaches have advantages and disadvantages [25]. For instance, the use of heterogeneous catalysts increases the efficiency in terms of product separation, effluent treatment, and stream recycle. Despite this, heterogeneous systems are characterised by a huge variety of different active sites, which makes it difficult to reach high selectivity for a specific product. In contrast, homogeneous catalysts make it easier to study the relationship between structure and reactivity, optimizing the selectivity. A common limit for both approaches is the degradation of the catalyst. Indeed, in heterogeneous catalysis, the main challenge is represented by electrode poisoning by either intermediates,

byproducts, or impurities, while molecular catalysts go towards slow decomposition owing to undesired side reactions.

In this thesis, we will mainly focus on the optimization and understanding of heterogeneous catalyst reaction mechanism by means of theoretical calculations, with the aim of achieving increased CO_2RR performance.

1.2.3 Assessing CO_2RR efficiency and selectivity

To characterize the performance of a CO_2RR electrochemical process, several figures of merit are commonly used experimentally. Among others, the most employed are the onset potential, the overpotential, the current density, the turnover frequency, the Faradaic efficiency, the energetic efficiency, and the process stability [21, 31]. Here I recall the definition of the process parameters that will be referred to in this thesis to asses electrocatalyst functionality.

The onset potential (U_{onset}) is the external potential applied for the reaction to take place, while the difference between the equilibrium thermodynamic potential (U_0) and the onset potential defines the overpotential (η).

At a given potential, the ratio between the current flow and the active electrode area defines the current density, j. The current density is a measure of the catalytic activity, that is the electrochemical reaction rate per area of electrode.

The Faradaic efficiency for product i, FE_i, defines the selectivity of reducing CO_2 to that product, and can be calculated as

$$FE_i = \frac{z_i \cdot n_i \cdot F}{Q} \tag{1.4}$$

where z_i represents the number of electrons involved in the reduction reaction to product i, n_i is the number of produced moles of product i, and Q is the total charge consumed overall during the reduction process. F is Faraday's constant $F = 9.648 \cdot 10^4\,\mathrm{C\,mol^{-1}}$. Generally, during an electrochemical reaction, one of the main targets is to get a high Faradaic efficiency for a specific product, which is equivalent to achieving high selectivity.

Overall, promising electrolyzers for CO_2RR should display a low overpotential, a high current density and high selectivity towards a desired product.

1.3 Classes of electrocatalysts for CO_2RR

As previously mentioned, two macro classes of electrocatalysts for CO_2RR exist: homogeneous and heterogeneous catalysts. In this section the attention is narrowed down to heterogeneous catalysts, since they show unique advantages, such as low toxicity, long lifetime and easy recyclability, increasing interest in their future application on a large scale [32, 33].

Generally, heterogeneous electrocatalytic reduction of CO_2 takes place at the interface between the solid electrode and the aqueous electrolyte. The mechanism usually includes three main steps: (*i*) CO_2 chemisorption on the surface of the cathode; (*ii*) cleavage of C–O bonds for the formation of O-H bonds as well as establishment of C-H bonds and C–C coupling by means of electrons exchange and protons movement; and (*iii*) rearrangement of the intermediates to the final chemicals, followed by their desorption from the catalytic surface and leakage into the electrolyte [34]. The whole process hinges on the physical and chemical properties of the electrode and electrocatalyst used, since its chemical nature and morphology enable the activation of the CO_2 reducing the overpotential values. In the last few years, many efforts have been dedicated to the development of novel, cost-efficient catalysts to increase the selectivity of CO_2RR at low overpotentials and with long-term stability.

An important class of electrodes is represented by metallic materials. Indeed, during the past few decades, metal-based electrocatalysts have been widely used for CO_2 conversion, starting from the pioneering research by Hori [35], who studied the relationship between the metal species and the corresponding selectivity towards specific reduction products. Metal electrodes can be classified into three groups [36]: (*1*) *precious metal* (Ag, Au, Pd)-based and Zn-based electrodes selective for the formation of CO [37–39]; (*2*) *post-transition metal* (In, Sn, Pb)- based catalysts usually ideal for the production of formate ($HCOO^-$) and formic acid (HCOOH) [40]; (*3*) *copper* (Cu)-based materials, which, interestingly, have the unique ability to generate a multitude of single- and multi-carbon species [41].

Emergent electrocatalysts which have gradually got attention are inorganic metal compounds, such as metal oxides, and carbon-based materials. The moderate energy efficiency of fully or partially oxidized metal electrodes is due to the binding nature of the active sites during the interaction with CO_2 or with other reaction intermediates, resulting in a potential improvement in terms of selectivity and activity, although instability problems exist [42]. To address the problems of instability and high costs, promising cheaper alternatives instead of precious noble metals are carbon-based materials like graphene, carbon nanotubes, porous carbon, and carbon fibers [43]. In addition to the excellent chemical stability and affordable costs, this category of electrodes possesses many intrinsic advantages, including high surface area, environmental sustainability, and high conductivity, becoming increasingly attractive for CO_2 conversion [44, 45]. In this context, there has been a growing interest in the development of metal-doped carbon materials, in which heteroatoms, commonly B, N, P, and S, are introduced in the carbon support and coordinate the metals in isolated active centers, hence the name single atom catalysts (SACs) [46–49].

Finally, a further approach consists in the employment of metal-organic frameworks (MOFs) owing to their versatile nature, unique porous structure, and large specific surface area [50–52]. In MOFs, the stabilization of metal active sites (cations) occurs via organic ligands in crystalline structure. In addition, physical and chemical properties of this compound class are highly tunable by easily changing the metal nodes and the organic linkers. Nonetheless, the limited conductivity and stability may inhibit the catalytic performance of these materials [53].

In this thesis, we will present the results of investigations performed on electrocatalysts belonging to the classes of metals, metal oxides and MOFs. The main characteristics of these classes are discussed in the following sections.

1.3.1 Metal- and metal-oxide based catalysts

A variety of metal electrodes have been investigated for CO_2RR and have been generally classified in relation to the reduction products obtained during the reduction process [54].

Among all metals, copper is unique, because it is the only species able to generate a variety of CO_2 reduction products including multi-carbon molecules [55].

In aqueous electrolytes, Cu typically produces CO, but, since the CO binding energy to the copper surface is high enough, CO does not readily get desorbed and can be further reduced to either alcohols or hydrocarbons [56]. Unfortunately, typical limitations of Cu electrodes are large overpotentials, which imply unsatisfactory energy efficiency, poor selectivity and fast deactivation [57–60]. Many studies have provided various strategies to enhance the performance of Cu catalysts. One approach involves the employment of different morphologies of Cu nanocrystals, like nanowires [58], fibers [59] and nanoparticles [57], which increase the number of active sites (surface planes, edges, and corners) and present a large surface area. An alternative approach consist in alloying Cu with other metallic species. The role of the heteroatoms is to tailor the binding strength of specific reaction intermediates on the catalyst surface, thus driving the reduction towards desired products [60].

Post-transition metals like Sn, Pb, and In are characterized by a high oxygen and low hydrogen binding strength, and are known to produce HCOOH [60]. At the surface of these metals, the reaction proceeds through the oxygen-bound *OCHO intermediate, due to their high oxygen affinities, and for this reason the reduction reaction gives formic acid. On the contrary the interaction with the *COOH intermediate is weak and CO formation is hindered. Most of these electrochemical catalysts are characterized by high HER overpotentials, weak CO adsorption, and weak stabilization of CO_2 ions [30]. To improve the CO_2RR performance of these electrodes, recent studies have focused on engineering the catalyst structure by either increasing the number of active sites at the surface (forming for example 3D porous electrodes or nanocomposite structure [61] confined in graphene [62]), or by employing bimetallic alloys [63–65].

Many transition metal electrodes such as Au, Ag, Zn, Pd and Ni are selective towards the formation of CO [66]. This reduction product is interesting as a feedstock in the Fischer–Tropsch synthesis, and can be used as building block to synthesise a wide variety of hydrocarbon fuels and chemicals [67, 68]. On these metal surfaces, the reaction proceeds via the formation of the *COOH intermediate, followed by the cleavage of the C-OH bond once the hydroxyl group is reduced by an electron-proton pair to form H_2O and CO. To produce CO, the surface catalyst has to weakly adsorb CO, so that the molecule can easily desorb from the surface once formed [66]. Au, in its polycrystalline form, possesses the highest selectivity and activity toward CO [69],

but it is a rare and expensive element, limiting its application at the industrial scale, while a less expensive promising alternative to Au electrodes is Ag [70]. Finally, Zn is reported as a promising catalyst for CO production thanks to its earth-abundancy and low-cost. However, the stability of Zn electrodes must be improved and their FEs lie between 40% and 80% [35] because of surface contamination or impurity of the electrolyte affecting Zn selectivity toward CO [71]. To get a better insight into the selectivity of transition-metal electrodes, the HER and CO_2RR mechanisms on Ag and Zn surfaces have been investigated in this work and will be presented in Chapter 5.

The catalytic performance of some metal electrodes can be significantly improved if they are employed in their oxidized (M-O) form [72]. A possible strategy to enhance the M-O activity, is the chemical introduction of defects (point, planar, line, and bulk defects) and oxygen vacancies, which increase the conductivity and generate active CO_2 adsorption sites characterized by low CO_2RR energy barriers [73, 74]. A suitable engineering of M-O morphology can also significantly affect the product selectivity, energy efficiency, and reaction rate. For example, a robust, highly porous morphology provides large catalytic surface areas and exposes a greater number of active sites, while advanced structures, like nanosheets and nanofibers, promote charge transfer and decrease the overpotential [75]. Metal oxides of the p-block, such as Sn and Bi oxides, have been widely reported for the production of formate [76, 77], while Cu oxide-based electrodes are known to assist formation of C-C bonds for the synthesis of hydrocarbons [78, 79]. The catalytic activity of these materials may originate from the reconstruction of reduced M-O surface when the electrode is subject to negative operating potentials. However, under working electrode conditions, even though the reduction of the M-O is thermodynamically expected, both metal and oxide phases may be still present. This co-existence makes it difficult to identify which is the active phase of the electrocatalyst under operating conditions. In this regard, the catalytic surface structure of SnO_2 has been investigated and presented in Chapter 3.

1.3.2 Metal-organic frameworks

Metal–organic frameworks (MOFs) are highly porous crystalline materials built from repeating structural units of inorganic nodes coordinated through organic ligands chosen from a wide range of linkers [80].

Metal species reside in the inorganic nodes of the crystal and are thought to act as catalytic centers. They are homogeneously dispersed throughout the material and interconnected to each other by organic linkers, which contain donor atoms such as N, O or S. The type of metal and its coordination number, the nature of ligands, and the surrounding chemical environment influence the catalytic properties of the active site as well as the electronic features of the catalyst [81, 82]. The structural diversity and versatile nature of these materials attracted the attention of the scientific community [50, 83]. The major advantages in using MOFs over existing electrocatalysts lie in their high surface area, which leads to a considerable increase in the number of active sites [51, 84]. Moreover, the porous structure facilitates the transport of reactant species to the active sites in the material by reducing mass transport limitations [53, 52, 85].

To date, MOF-based materials have shown encouraging performance in electrocatalytic CO_2RR [86, 87]. To obtain MOFs electrocatalysts suitable for CO_2 conversion, the selection of a proper metal center is essential. In the literature, a wide range of node species have been explored as catalytic sites to get selected final products in CO_2RR. For example, MOFs electrocatalysts containing noble-metals, Co and Zn produce CO, while Cu nodes releases multi-carbon chemicals [88–90]. Structural changes to the organic linkers can alter transport since they determine the shape and diameter of the pore and channels [91].

Compared to heterogeneous inorganic electrocatalysts, the catalytic performance of pristine MOFs materials is lower because of their limited electrical conductivity and poor stability [92]. To overcome this issue, the MOFs electrocatalyst can be grown on conductive support such as carbon paper, graphene, and carbon nanotube (CNT) to facilitate the transfer of electrons to the electrocatalyst surface [93, 94, 89, 95]. The direct pyrolysis of MOFs and their composites represents an alternative procedure which forms metal nanoparticles or/and single atom species uniformly distributed throughout the electrocatalyst and the incorportation of defects [96–98].

A subclass of MOFs is represented by zeolitic imidazolate frameworks (ZIFs), microporous materials with tetrahedral frameworks composed of metal ions and imidazolate ligands [99]. These materials show good stability in aqueous media and high selectivity [100, 101]. Commonly, ZIFs contain Zn atoms as metal nodes [102] and one of the most studied systems belonging to this subclass is ZIF-8, characterised by a sodalite topology and a $Zn(Mim)_2$ stoichiometric unit, where *Mim* represents the 2-methylimidazolate linker. The employment of ZIF-8 in various fields, from gas sensing to heterogeneous catalysis, is mainly due to its well-defined porous structure, manageable morphology and high content of nitrogen atoms contained in the organic ligands [103, 104]. The pioneering work of Wang et al. [105] explored the use of ZIF-8 as possible electrocatalyst for CO_2RR, followed by other studies which highlight the high selectivity for CO production investigating various Zn-ZIF systems which have the same sodalite topology, but differ in the imidazole linkers [106].

The mechanism which leads to the selective reduction of CO_2 to CO in this type of catalysts was unknown and is addressed during this thesis work, as discussed in Chapter 4.

1.4 The role of theoretical modelling in electrocatalysis

In the field of electrocatalysis, there is an increasing use of a combination of theoretical calculations and experimental investigations. Electronic structure calculations using, for example, Density Functional Theory (DFT) combined with rate theory, can be particularly powerful in explaining experimental results and providing guidelines for synthesizing highly active, well-defined, and stable electrocatalysts in the laboratory. With the constant progress of computational tools, the use of reliable electrocatalytic models is advancing more and more through DFT-based theories and methods, which can: *i)* determine the atomic structure and chemical-physical properties of the electrocatalytic surface under working conditions; *ii)* investigate the *thermodynamics* and *kinetics* of electrocatalytic reaction pathways.

In electrocatalysis, the external applied potential, U_{ext}, and the pH conditions may affect the surface structure of the electrode and, consequently, the selectivity of the material towards specific reaction products. In this regard, first-principles theoretical calculations are able to account for U_{ext}, pH, and solvation parameters to provide reliable models of electrocatalytic systems. Furthermore, the analysis of the energy landscape of a electrocatalytic reaction at the surface of the electrode by a thermodynamic approach can highlight the working conditions at which the reaction becomes spontaneous. In this perspective, the computational hydrogen electrode (CHE) method [107] allows to estimate the Gibbs free energy profile of the electrocatalytic reaction, predicting the catalytic activity of the electrocatalyst and the relative U_{onset}. Nonetheless, thermodynamic predictions may not be enough to interpret experimental observations. To gain a complete understanding of a reaction at the electrocatalyst surface, further insights must be obtained through the calculation of kinetic energy barriers, which can be computed using commonly used methods, such as the nudged elastic band (NEB) and dimer methods [108–110], albeit at a high computational cost.

The role of theoretical calculations in elucidating experimental results and guiding experiments, represents the main purpose of this thesis. In this thesis work, we will present the powerful contribution of theoretical modeling to deepen the knowledge of current unexplained findings of electrocatalytic materials, such as their structural properties and activity, and predict realistic models of performing electrocatalysts as guidelines for their experimental realization. In the first part of the thesis, we carried out a thermodynamic investigation to understand the active surface structure of SnO_2 electrocatalyst towards HCOOH production. The purpose of this work was to provide a theoretical interpretation of the experimental measurements from the literature. The same approach was then employed to determine the selective reaction mechanism for CO_2 capture and reduction to CO in ZIF-8 material and how to tune the catalytic activity of the electrocatalyst. The obtained DFT results have been confirmed by experimental investigations. Finally, in the last part of the thesis, the limits shown by thermodynamics in the interpretation of the selectivity of Ag and Zn electrodes towards CO production led us to gain a deepen insight into the reaction mechanisms at these metals. In particular, we investigated the kinetic energy barriers of CO_2RR and the competing HER and suggest a link with the experimental findings.

CHAPTER 2

Methods for theoretical calculations

In recent decades, electronic structure calculations have evolved as promising tools to estimate physical properties of macroscopic system based on a quantum description of electrons. Density Functional Theory (DFT) is one of the strategies developed to solve the Schrödinger equation of a many-body system. In this Chapter, we present an overview of the theoretical principles that underpin several of the topics addressed in this thesis. We introduce the fundamental concepts of DFT and then move on to discuss the main technical aspects of its implementation. We also explore the methods used to predict both the thermodynamics and kinetics of electrochemical reactions.

2.1 The many-body Hamiltonian and the Born-Oppenheimer approximation

Ab initio, or *first-principle*, methods are a powerful tool to obtain an accurate quantum description of many-particle systems, such as molecules and solids, based only on fundamental physical properties, without resorting to empirical inputs.

A many-body system, e.g. a solid, is composed of electrons and nuclei, coupled by Coulomb interactions. The quantum mechanical description of such systems lies

on the *ab initio* Hamiltonian of the system

$$\hat{H} = \hat{T}_n + \hat{V}_{n-n} + \hat{T}_e + \hat{V}_{e-n} + \hat{V}_{e-e}. \tag{2.1}$$

Here, $\hat{T}_n$ represents the kinetic energy of the L nuclei[1],

$$\hat{T}_n = -\frac{1}{2}\sum_I \frac{\nabla^2_{\mathbf{R}_I}}{2M_I}, \tag{2.2}$$

where $\mathbf{R}_I$ and M_I are the coordinates and the mass of the I-th nucleus. $\hat{V}_{n-n}$ gives the repulsion among nuclei

$$\hat{V}_{n-n} = \frac{1}{2}\sum_{I\neq J} \frac{Z_I Z_J}{|\mathbf{R}_I - \mathbf{R}_J|}, \tag{2.3}$$

where Z_I is the atomic number of the I-th nucleus. $\hat{T}_e$ describes the kinetic energy of the N electrons

$$\hat{T}_e = \frac{1}{2}\sum_i \nabla^2_{\mathbf{r}_i}, \tag{2.4}$$

where $\mathbf{r}_i$ are the coordinates of the i-th electron. $\hat{V}_{n-e}$ represents the interaction between nuclei and electrons

$$\hat{V}_{n-e} = -\sum_{i,I}^{L} \frac{Z_I}{|\mathbf{r}_i - \mathbf{R}_I|}, \tag{2.5}$$

while $\hat{V}_{e-e}$ describes the Coulomb interaction among electrons

$$\hat{V}_{e-e} = \frac{1}{2}\sum_{i\neq j} \frac{1}{|\mathbf{r}_i - \mathbf{r}_j|}. \tag{2.6}$$

With the Hamiltonian in Eq. (2.1) the stationary Schrödinger equation reads

$$\hat{H}\Phi_a(\{\mathbf{r}_i\},\{\mathbf{R}_I\}) = E_a\Phi_a(\{\mathbf{r}_i\},\{\mathbf{R}_I\}), \tag{2.7}$$

The full, many-body wavefunction of the system is a function of all electron and nuclei coordinates $\Phi(\mathbf{r}_1,\ldots,\mathbf{r}_N,\mathbf{R}_1,\ldots\mathbf{R}_L) \equiv \Phi(\{\mathbf{r}_i\},\{\mathbf{R}_I\})$ and solves the

[1]For simplicity we adopt Hartree atomic units.

Schrödinger equation

$$\hat{H}\Phi(\{\mathbf{r}_i\},\{\mathbf{R}_I\}) = E\Phi(\{\mathbf{r}_i\},\{\mathbf{R}_I\}). \tag{2.8}$$

The Born-Oppenheimer approximation [111] allows to simplify Eq.(2.8). It amounts to decoupling the electronic from the nuclear motion, relying on the different energy scales of the two types of motion. This is achieved by the factorization of the full wavefunction Φ in a nuclear wavefunction $\chi(\{\mathbf{R}_I\})$ and an electron wavefunction $\Psi(\{\mathbf{r}_i\};\{\mathbf{R}_I\})$ that depends *parametrically* on the nuclear coordinates

$$\Phi(\{\mathbf{R}_I\},\{\mathbf{r}_i\}) = \chi(\{\mathbf{R}_I\})\,\Psi(\{\mathbf{r}_i\};\{\mathbf{R}_I\}). \tag{2.9}$$

The electronic wavefunction is a solution of the electronic Schrödinger equation

$$\left[\hat{T}_e + \hat{V}_{n-e} + \hat{V}_{e-e}\right]\Psi(\{\mathbf{r}_i\};\{\mathbf{R}_I\}) = E(\{\mathbf{R}_I\})\Psi(\{\mathbf{r}_i\};\{\mathbf{R}_I\}), \tag{2.10}$$

which is an eigenvalue problem for any given set $\{\mathbf{R}_I\}$. The obtained eigenvalues $E(\{\mathbf{R}_I\})$ can be then regarded as potential terms in the Schrödinger equation for the nuclear motion

$$\left[\hat{T}_n + \hat{V}_{n-n} + E(\{\mathbf{R}_I\})\right]\chi(\{\mathbf{R}_I\}) = E_n\chi(\{\mathbf{R}_I\}). \tag{2.11}$$

Despite the simplifications introduced by the Born-Oppenheimer approximation, the solution of the electronic Schrödinger equation, (2.10) remains a complex quantum many-body problem, due to the interaction term $\hat{V}_{e-e}$ and the dependence on $3N$ space variables, of the electronic wavefunction $\Psi(\{\mathbf{r}_i\})$. An approximate method to handle the electronic problem is described in the following section.

2.2 Density Functional Theory

Density Functional Theory (DFT) is the most popular approach to describe the ground states of interacting, many-electron systems with relatively small computational cost. In contrast to wave function based methods, such as Hartree-Fock and post-Hartree-Fock, based on the full electronic wave function, $\Psi(\{\mathbf{r}_i\})$, the

fundamental breakthrough of DFT is to focus instead on the electronic density, $n(\mathbf{r})$, thus reducing the dimensionality of the problem from $3N$ to 3.

In 1927, the quantum mechanical theory proposed by Llewllyn Thomas and Enrico Fermi [112, 113] laid the foundations of DFT, describing the electronic structure in terms of electron density. The Thomas-Fermi model approximates a multi-electron system with a non-interacting uniform gas, where the kinetic energy is an explicit functional of the density which is equal to the local density at any given position. Shortly after, Dirac provided a further improvement to Thomas-Fermi model formulating the local approximation for exchange [114]. However, the fundamental advancements due to the Hohenberg and Kohn theorems [115] and Kohn and Sham method [116] established the birth of DFT, with the formalism is presented in this section.

2.2.1 The Hohenberg-Kohn theorems

Consider a system of N electrons in the presence of a time-independent local external potential $V(\mathbf{r})$. In case of a system composed of a fixed number of particles and known electron density $n(\mathbf{r})$, the first Hohenberg-Kohn theorem states that $V(\mathbf{r})$ is determined by the electronic ground state density $n(\mathbf{r})$, up to an additive constant. Hence, $n(\mathbf{r})$ univocally defines the external potential and, in turn, the Hamiltonian in Eq. (2.10) and all the electronic properties of the underlying system. The expectation value of any observable on the ground state is therefore a functional of the electronic density. In particular, the total energy of the system is

$$E[n] = F[n] + V[n] = F[n] + \int n(\mathbf{r})v(\mathbf{r})d\mathbf{r}, \tag{2.12}$$

where $F[n]$ is a universal functional containing the kinetic term and the electron-electron interactions.

The second Hohenberg-Kohn theorem provides the definition of an energy functional for the system and demonstrates that the latter is minimized by the the correct ground state electron density n_0

$$E_0 \equiv E[n_0] \leq E[n], \tag{2.13}$$

for any $n(\mathbf{r}) \neq n_0(\mathbf{r})$.

By the variational principle in Eq. (2.13), the ground state density can be obtained through variation of the energy with respect to the density $n(\mathbf{r})$

$$\frac{\delta}{\delta n(\mathbf{r})}\left\{E[n]-\mu\left[\int n(\mathbf{r})d\mathbf{r}-N\right]\right\}=0, \tag{2.14}$$

with the constraint imposed on the number of electrons. This leads to

$$\mu=\frac{\delta E_v[n]}{\delta n}=v(\mathbf{r})+\frac{\delta F[n]}{\delta n}, \tag{2.15}$$

where the Lagrange multiplier μ is the chemical potential.

2.2.2 The Kohn-Sham equations

In principle, Eq. (2.15) determines the ground state electron density, however the exact form of Hohenberg-Kohn functional $F[n]$ is unknown. To overcome this issue, in 1965, Kohn and Sham [116] developed a method to study a system with interacting electrons considering an auxiliary system of non-interacting electrons with the same electron density of the interacting one.

The Hohenberg-Kohn theorems are valid for any many-electron systems, irrespective of the specific form of the electron-electron interaction. Therefore, they can also be applied to noninteracting systems, in which $\hat{V}_{e-e}=0$, and, in this case, the total energy functional reads

$$\begin{aligned} E_s[n] &= T_s[n]+V_s[n] \\ &= T_s[n]+\int v_s(\mathbf{r})n(\mathbf{r})d\mathbf{r}, \end{aligned} \tag{2.16}$$

where $T_s[n]$ is the kinetic energy functional of the noninteracting system and $v_s[n]$ is an *external* potential. A minimum principle holds for $E_s[n]$ for any $n(\mathbf{r}) \neq n_{0s}(\mathbf{r})$ as

$$E_s[n_{0s}] \leq E_s[n], \tag{2.17}$$

where $n_{0s}(\mathbf{r})$ is the ground state density of the noninteracting system. The wavefunction of the noninteracting system has the form of a Slater determinant of single-

particle orbitals that solve the equation

$$\left[-\nabla^2 + v_s(\mathbf{r})\right] \psi_i(\mathbf{r}) = \varepsilon_i \psi_i(\mathbf{r}), \tag{2.18}$$

and give the electron density of the noninteracting system as

$$n_{0s}(\mathbf{r}) = \sum_i |\psi_i(\mathbf{r})|^2. \tag{2.19}$$

The noninteracting kinetic functional $T_s[n]$ can also be expressed in terms of the single-particle orbitals, which can be seen, in turn, as functionals of the density $\psi_i[n](\mathbf{r})$.

We can now turn to the real, interacting system with an external potential $v(\mathbf{r})$ and assume that its ground state density $n_0(\mathbf{r})$ is also the electron density of the ground state of an auxiliary, noninteracting system with a yet to find external potential $v_s(\mathbf{r})$

$$n_0(\mathbf{r}) \equiv n_{0s}(\mathbf{r}). \tag{2.20}$$

The ground state density of the interacting system can then be obtained from Eqs. (2.17) and (2.16) by finding the suitable external potential v_s. To this end, the functional $E[n(\mathbf{r})]$ can be decomposed as

$$E[n(\mathbf{r})] = T_s[n(\mathbf{r})] + E_{\mathrm{H}}[n(\mathbf{r})] + V[n(\mathbf{r})] + E_{\mathrm{xc}}[n(\mathbf{r})], \tag{2.21}$$

where the Hartree term

$$E_{\mathrm{H}} = \frac{1}{2} \int d\mathbf{r} \int d\mathbf{r}' \frac{n(\mathbf{r}) n(\mathbf{r}')}{|\mathbf{r} - \mathbf{r}'|}, \tag{2.22}$$

contains the classical interaction energy between the electrons as well as self-interaction. The new functional $E_{\mathrm{xc}}[n(\mathbf{r})]$, *defined* in Eq. (2.21), is called exchange-correlation (xc) energy functional and wraps all the complicated many-body effects contained in $F[n]$ which are not accounted for by $T_s[n]$ and $E_{\mathrm{H}}[n]$.

Variations of Eq. (2.21) with respect to the density lead to the condition

$$\int d\mathbf{r} \left[v_s(\mathbf{r}) - \int d\mathbf{r}' \frac{n_0(\mathbf{r}')}{|\mathbf{r} - \mathbf{r}'|} - v(\mathbf{r}) - \left. \frac{\delta E_{\mathrm{xc}}[n]}{\delta n(\mathbf{r})} \right|_{n=n_0} \right] \delta n(\mathbf{r}) = 0, \tag{2.23}$$

that must be valid for any arbitrary variation $\delta n(\mathbf{r})$, so that

$$v_s(\mathbf{r}) = v(\mathbf{r}) + v_{\mathrm{H}}[n_0](\mathbf{r}) + v_{\mathrm{xc}}[n_0](\mathbf{r}). \tag{2.24}$$

This defines the external potential v_s of the noninteracting system in terms of the external potential of the interacting one $v(\mathbf{r})$, the Hartree potential

$$v_{\mathrm{H}}[n](\mathbf{r}) = \int d\mathbf{r}' \frac{n(\mathbf{r}')}{|\mathbf{r}-\mathbf{r}'|}, \tag{2.25}$$

and the exchange-correlation potential

$$v_{\mathrm{xc}}[n](\mathbf{r}) = \frac{\delta E_{\mathrm{xc}}[n]}{\delta n(\mathbf{r})}. \tag{2.26}$$

The external potential of the noninteracting system is therefore a functional of the density. Eq. (2.19) must then be solved self-consistently together with the Kohn-Sham equations for the single-particle wavefunctions

$$\left[-\frac{1}{2}\nabla^2 + v(\mathbf{r}) + v_{\mathrm{H}}[n_0](\mathbf{r}) + v_{\mathrm{xc}}[n_0](\mathbf{r})\right] \psi_i(\mathbf{r}) = \varepsilon_i \psi_i(\mathbf{r}), \tag{2.27}$$

Once $n(\mathbf{r})$ is obtained, all the other observable can be derived. Although DFT is an exact theory of the ground state, the exchange and correlation potential is not known explicitly and DFT methods differ on the treatment of this term. Literature presents different formulations. John P. [117] proposed a ranking of DFT approximations according to the so called Jacob's Ladder (Figure 2.1), where one can expect an improvement in accuracy of the method, but, at the same time, the usage of progressively more complicated approximations by climbing the steps of the ladder. The lowest step corresponds to the simplest one so-called Local Density Approximation (LDA), followed by the Generalized Gradient Approximation (GGA), meta-GGA (m-GGA) and, finally, hybrid-GGA (h-GGA) forms which occupy the highest step of the ladder.

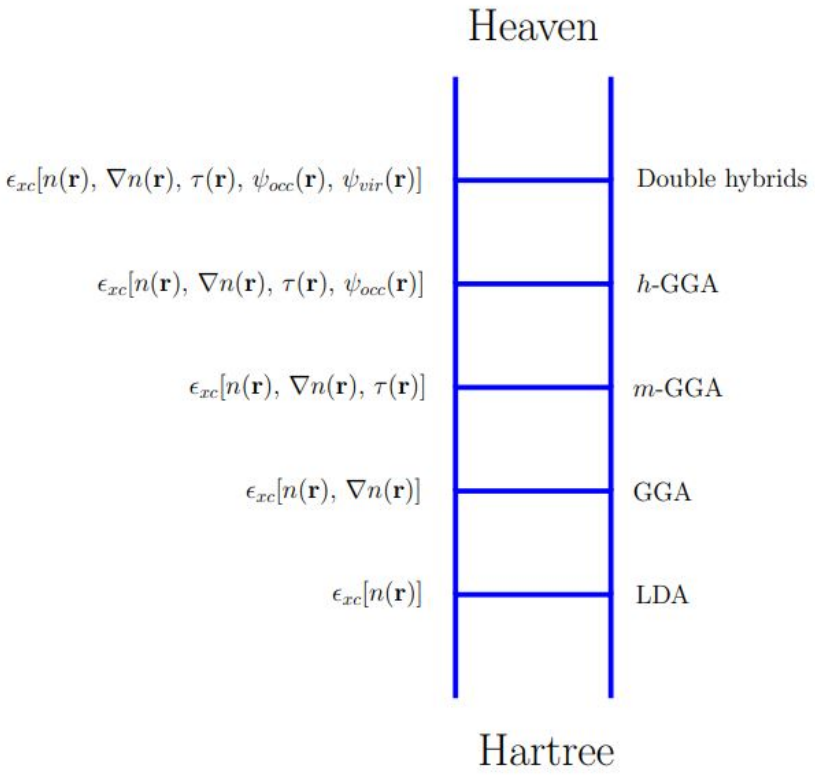


Figure 2.1 Schematic representation of DFT methods classification according to the Jacob's Ladder. The accuracy of the method increases moving from the bottom (LDA) to the top (Double Hybrids) of the ladder.

2.2.3 Approximations to the exchange-correlation functional

The critical part of the whole formalism consists in finding an expression for the exchange and correlation potential v_{xc}, Eq. (2.26). The simplest approach to v_{xc} is the Local Density Approximation (LDA) [118, 119]. According to this method, considering constant the density of a uniform gas of interacting electrons, the total $E_{\mathrm{xc}}[n]$ is given by multiplying exchange-correlation energy per particle $\varepsilon_{\mathrm{xc}}(n)$ as function of the density by the total number of electrons N in the gas:

$$E_{\mathrm{xc}}[n] = N\varepsilon_{\mathrm{xc}}(n). \tag{2.28}$$

LDA analogously deals with the non-uniform electron gas. In this case, each part of the non-homogeneous gas is treated as locally uniform and contributes to the the

total $E_{\mathrm{xc}}[n]$ in the form

$$E_{\mathrm{xc}}^{\mathrm{LDA}} = \int n(\mathbf{r}) \varepsilon_{\mathrm{xc}}^{\mathrm{hom}}(n(\mathbf{r}))\, d\mathbf{r}. \tag{2.29}$$

$\varepsilon_{\mathrm{xc}}^{\mathrm{hom}}$ is the sum of the exchange ($\varepsilon_{\mathrm{x}}^{\mathrm{hom}}(n)$) and correlation energy ($\varepsilon_{\mathrm{c}}^{\mathrm{hom}}(n)$) per electron in the homogeneous electron gas of density n.

LDA functionals provide good results in the description of systems with delocalized electrons, such as metals. In other cases, the LDA approximation tends to over delocalize the electrons, underestimating bond distances and overestimating binding energies.

The Generalized Gradient Approximation (GGA) [120] gives a more accurate description of the electron density by introducing the first derivatives of the density

$$E_{\mathrm{xc}}^{\mathrm{GGA}} = \int f(n, \nabla n) d\mathbf{r}. \tag{2.30}$$

The Perdew, Burke and Ernzerhof (PBE) exchange-correlation functional [121] is probably one of the most used GGA methods in condensed matter physics, in which the correlation term is expressed as a local correlation plus an additive contribution both of which depend upon the density gradient. More accurate approximations of the exchange and correlation functional exist beyond the GGA, but they require a demanding computational cost. Throughout this work, we carried out the DFT simulations in the GGA-PBE functional. The choice to use GGA-PBE functional is due its large utilization in literature [122], and it has been carefully supported by preliminary tests in which the Heyd–Scuseria–Ernzerhof (HSE06) hybrid functional was used [123, 124].

2.3 The Hellmann-Feynman theorem

Consider a system with a fixed configuration of nuclei $\{\mathbf{R}_I\}$ and suppose its ground state eigenfunction $\Psi(\{\mathbf{R}_I\}) = \langle\{\mathbf{R}_I\}|\Psi\rangle$ is known. The energy will be given by

$$E = \frac{\langle\Psi|\hat{H}(\mathbf{R})|\Psi\rangle}{\langle\Psi|\Psi\rangle}. \tag{2.31}$$

The negative gradient of the energy with respect to $\mathbf{R}_J$ provides the force acting on a nucleus J

$$\mathbf{F}_J = -\nabla_{\mathbf{R}_J} E = -\nabla_{\mathbf{R}_J} \left[\frac{\langle \Psi | \hat{H}(\mathbf{R}) | \Psi \rangle}{\langle \Psi | \Psi \rangle} \right]. \tag{2.32}$$

On the right hand side of Eq. (2.32), both the Hamiltonian and the ground state depend on the coordinates $\{\mathbf{R}_I\}$. Since $|\Psi\rangle$ is an eigenstate of the Hamiltonian, the energy is at a minimum with respect to small variations in the wave function and is normalizable, the contributions to Eq. (2.32) due to variations of $|\Psi\rangle$ with respect to $\mathbf{R}_J$ vanish. Therefore, Eq. (2.33) reduces to

$$\mathbf{F}_J = -\frac{\langle \Psi | \nabla_{\mathbf{R}_J} \hat{H}(\mathbf{R}) | \Psi \rangle}{\langle \Psi | \Psi \rangle}, \tag{2.33}$$

and implies that the knowledge of the explicit dependence of the Hamiltonian on the system nuclear coordinates is enough to determine the forces acting on the atoms in a particular geometric configuration. Once the latter are known, it is possible to integrate the classical equation of motion and study the evolution of the geometry of the system.

2.4 Aspects of DFT implementation

In the following paragraphs some practical aspects regarding DFT implementation in computer codes will be discussed, in particular, the use of a plane-wave basis sets (Section 2.4.1) to expand the system wavefunction and the use of pseudopotentials (Section 2.4.2).

2.4.1 Basis set

To solve the Kohn-Sham equations, Eq. (2.27), and find the ground state wavefunction the single electron wavefunctions can be expanded on a complete basis set of functions $\{\phi_i(\mathbf{r})\}$ as

$$\psi_i(\mathbf{r}) = \sum_{j=1}^{\infty} c_j \phi_j(\mathbf{r}), \tag{2.34}$$

It is possible to distinguish two main classes of basis functions: plane waves, which are a combination of sine and cosine functions filling uniformly the space of the simulation cell, and localized basis sets, such as Gaussian or Slater-like functions. Different basis sets have their own advantages and disadvantages depending on the type of system being studied. Gaussian functions are commonly used for molecular systems, whereas plane wave basis sets are preferred for periodic systems. In our calculations, we focus on periodic systems and therefore exclusively employ plane wave basis sets.

Plane wave basis set

In a perfect crystal, the arrangement of the nuclei is periodic. Consequently, also the external potential $v(\mathbf{r})$is periodic, as $v(\mathbf{r}) = v(\mathbf{r} + l\mathbf{a})$, where $\mathbf{a}$ is a lattice vector and $l \in \mathbb{Z}$. In this cases, the Bloch theorem holds and the wavefunction is the product between a cell-periodic and a wave-like parts

$$\psi_{i,\mathbf{k}} = u_{i,\mathbf{k}}(\mathbf{r}) e^{i\mathbf{k}\cdot\mathbf{r}}, \tag{2.35}$$

where $u_{i,\mathbf{k}}(\mathbf{r})$ is a function that encodes the lattice periodicity. The periodic part of the wavefunction can be expanded in plane waves characterised by wave vectors $\mathbf{G}$ which are the reciprocal lattice vectors of the crystal

$$u_{i,\mathbf{k}}(\mathbf{r}) = \sum_{\mathbf{G}} c_{i\mathbf{k},\mathbf{G}} e^{i\mathbf{G}\cdot\mathbf{r}}. \tag{2.36}$$

Therefore, each electronic wavefunction can be expressed as a linear combination of plane waves (PW) as

$$\psi_{i,\mathbf{k}} = \sum_{\mathbf{G}} c_{i,\mathbf{k}+\mathbf{G}} e^{i(\mathbf{k}+\mathbf{G})\cdot\mathbf{r}}. \tag{2.37}$$

The $c_{i,\mathbf{k}+\mathbf{G}}$ are unknown and must be determined for each case of interest. Generally, the plane-waves basis set is infinite, but it is actually reduced to a finite number by truncating the sum over $\mathbf{G}$ to involve only those plane waves with a kinetic energy $E_k = \frac{1}{2}(\mathbf{k}+\mathbf{G})^2$ smaller than a given energy cutoff (E_{cut}), leading to an error in the computed total energy. Contrary to other methods (and basis sets), it is possible to control the convergence of the plane-wave basis set and the accuracy by merely changing the cutoff energy value.

2.4.2 Pseudopotentials

The Coulomb potential of the nuclei causes rapid oscillations of the single-particle wavefunctions $\psi(\mathbf{r})$ near the nucleus (dashed blue line in Figure 2.2), whose description requires a very large number of plane waves in the expansion of the wavefunction. This issues can be solved by noticing that only outer valence electrons participate in chemical bonding, while inner, core electrons are insensitive to the chemical environment. The relevant properties are therefore determined by the valence electron wavefunctions outside the core region, $r > r_c$. It is then possible to replace the strong Coulomb potential with a weaker pseudopotential (PP) [125] which gives valence wavefunctions (red line in Figure 2.2) that are identical to the true wavefunction for $r > r_c$, but do not oscillate in the core region. The wavefunction obtained with the PP can be represented by fewer plane-waves.

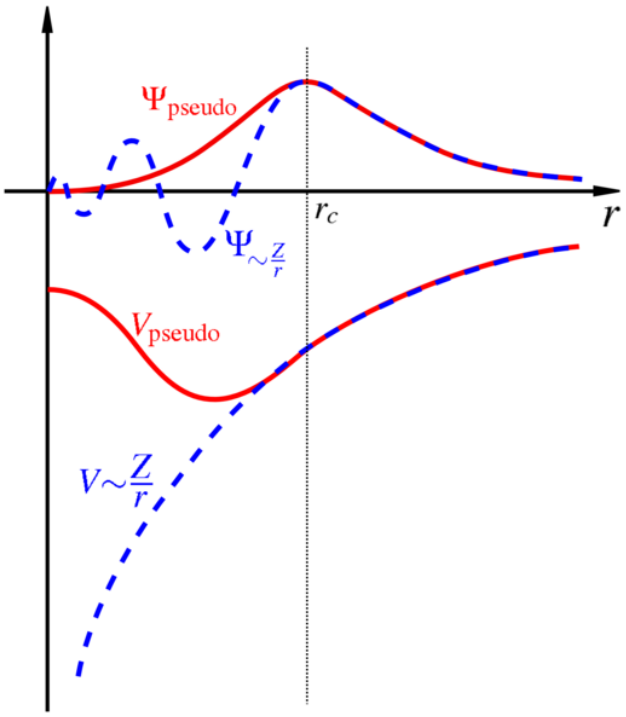


Figure 2.2 Comparison of a wavefunction in the Coulomb potential of the nucleus (blue) to the one in the pseudopotential (red). The real and the pseudo wavefunction and potentials match above a certain cutoff radius r_c.

It is possible to identify different classes of PPs, the most important ones being norm-conserving and ultrasoft PPs.

Norm-conserving pseudopotentials

Norm-conserving PPs satisfy the following conditions [126]:

- For a given atomic configuration, the valence eigenvalues of the true all-electron potential and the PP are the same.
- Outside a chosen core radius r_c, the valence eigenfunctions of the true all-electron potential and the PP are the same.
- The total charge of the true all-electron and pseudo eigenfunctions inside core radius r_c are the same.

$$4\pi \int_0^R |\psi_{\text{real}}(\mathbf{r})|^2 d\mathbf{r} = 4\pi \int_0^R |\psi^{\text{PS}}(\mathbf{r})|^2 d\mathbf{r} \tag{2.38}$$

- The logarithmic derivative and the energy derivative of the logarithmic derivative of the true all-electron and pseudo eigenfunctions match for $r > r_c$.

For a single atomic configuration, the first condition states that the true all-electron potential and the PP will give the same eigenenergy values ε_i. Along the bonding region, which means far way from the core shell, the second condition guarantees that the wavefunctions match as well. Furthermore, the fourth condition assures the equivalence of energy derivatives which requires that the scattering of the PP and the true all-electron potential both at ε_i and at energies close to ε_i. Since bonding with neighboring atoms will change the eigenergies away from the atomic energies ε_i, PP satisfying this requirement should give a good description of the bonding properties. The third requirement affirms that the electrostatic potential of the true all-electron and pseudo wavefunction are the same. Therefore, if the total charge within some core radius r_c is the same for two different radial potentials $V(r)$, then the energy derivatives of the logarithmic derivatives of their eigenfunctions will be the same.

Ultrasoft pseudopotentials

Vanderbilt [127] proposed to relax the norm-conserving requirement developing the so-called ultrasoft PPs, obtaining much smoother pseudo-wavefunctions thus reducing considerably the the number of plane waves needed for convergence. This approach is based on the generalization of the norm-conserving PPs to include an overlap operator $\hat{S}$ that appears on the right hand side of the secular equation

$$\left[-\frac{1}{2}\frac{d^2}{dr^2}+\frac{l(l+1)}{2r^2}+\hat{V}_{PS}\right]\psi_{l\tau}^{\mathrm{PS}}(r)=\varepsilon_{l\tau}\hat{S}\psi_{l\tau}^{\mathrm{PS}}(r), \tag{2.39}$$

turning this equation into a generalized eigenvalue problem. Here, the τ index discriminates between multiple solutions for the same value of l. Contrary to the norm-conserving scheme, where constraints on the pseudo wavefunction are imposed to reproduce correctly the energy derivative, in this case the operator $\hat{S}$ is defined in such a manner that the energy derivative of the logarithmic derivative of the pseudo wavefunction will be reproduced for an arbitrary choice of the pseudo wavefunctions ψ_i^{PS}. For this reason, the choice of the the pseudofunctions ψ_i^{PS} is less restricted in the ultrasoft scheme, becoming smoother than the norm-conserving one.

2.5 Applying DFT to chemical reactions

DFT has emerged as a powerful tool for investigating a wide range of phenomena, spanning from materials science to chemistry and biology. In this context, DFT has been extensively applied to the study of chemical reactions. By analyzing the *potential energy surface* (PES), which describes the energy of a system as a function of its atomic coordinates, DFT can provide valuable insights into the reaction mechanism and the stability of the reactants, intermediates, and products. Moreover, the energy surface coming from DFT calculations can also be utilized to calculate the thermodynamics of a reaction, including the reaction enthalpy and Gibbs free energy, which are crucial for predicting whether a reaction is thermodynamically feasible. Finally, the energy surface obtained from DFT calculations can enable the

study of reaction kinetics, such as the rate constant and activation energy, which are essential for understanding the reaction mechanism and designing catalysts.

In the following paragraphs, we will provide an overview of these types of calculations.

2.5.1 Exploring the potential energy surface

The potential energy surface (PES) describes the energy of a system as a function of the positions of the nuclei, $E(\{\mathbf{R_I}\})$.

In order to minimize the energy of the whole system and achieve zero forces on the atoms, the geometry optimization process iteratively moves the atoms along the PES of the system.
As a result, it is possible to think of the PES as a hyperspace with $3N$ dimensions, where N is the number of atoms of the system or, more generally, its degrees of freedom. Each point of the PES represents a specific set of coordinates for the atoms in the system. Figure 2.3 shows a model of PES, and the corresponding 2-

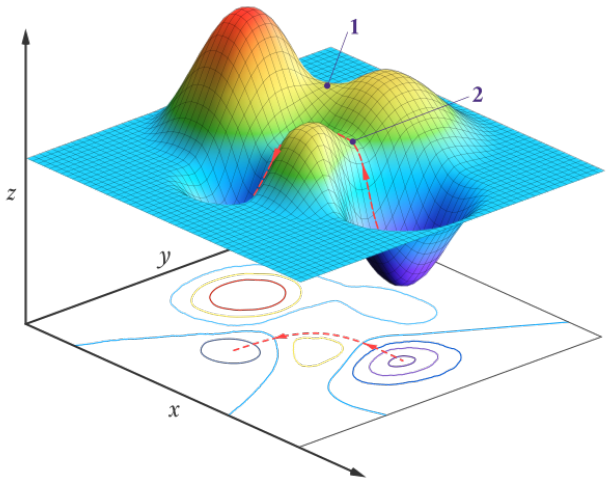


Figure 2.3 A 2-D contour map and corresponding PES model for a hypothetical endothermic reaction. The color scheme of the PES has the same meaning as that of the 2-D contour map - red is high potential energy and violet is low potential energy. Points "1" and "2" represent the transition states at the saddle points of the PES. Figure taken from Ref. [128].

dimensional contour map, for a possible endothermic reaction, where the dashed red line displays the minimum energy pathway from the reactants towards the products. The potential energy decreases as the color along the PES changes from red to violet. The PES can be imagined as a mountainous landscape: the valleys are the energy minima (deep hole in the PES and the smallest, violet oval in the contour map) representing reactants, intermediates and products, while the points 1 and 2 are saddle points on the energy surface representing a 'mountain pass' for an alternative and favoured reaction processes, respectively. The optimal atomic coordinates of a chemical species corresponds to a minimum. There may be several minima along the PES, representing conformers and isomers of a molecule or species involved in a reaction, for instance. Hence, the latter can be represented as the transfer from the 'valleys' of reactants to the 'valleys' of products, and a specific pathway through the PES determines the reaction mechanism. The highest point on the reaction pathway given by a minimum energy path is a saddle point on the energy surface. It represents the minimal energy needed to switch between reactants and products.

Both minimum and transition structures can be identified through geometry optimization. A Self-Consistent Field (SCF) calculation is required for each optimization step, since the system leads to a different structure during the minimization procedure with respect to the previous ones.

Efficient mathematical tools to perform geometry optimization make use of the first derivatives of PES with respect to geometric parameters. When the gradient is approximately to zero, the optimization is completed and a stationary point is identified. However, to classify it, it is necessary to calculate the Hessian matrix, that is the second derivatives of the energy with respect to atomic coordinates. The eigenvalues of the Hessian are related to the harmonic vibrational frequencies and eigenvectors corresponding to the normal modes of vibration of the atoms. If all the eigenvalues of Hessian matrix are positive, all the frequencies are real and the configuration of the atoms corresponds to a minimum on the energy surface. Else, if one eigenvalue is negative the this corresponds to a first order saddle point on the energy surface and the negative eigenvalue can be considered to correspond to imaginary frequency.

2.5.2 Thermodynamic properties

The investigation of chemical reactions, as in catalysis and electrocatalysis, must start from the study of the reaction thermodynamics. This implies evaluating the appropriate thermodynamic potential of each reaction step: reactants, intermediate states and products.

We can consider a generic electrochemical reaction occurring in two steps

$$\mathrm{A\,(g)} + 2(\mathrm{H^+} + \mathrm{e^-}) + * \rightarrow {}^{*}\mathrm{AH} + (\mathrm{H^+} + \mathrm{e^-}) \rightarrow \mathrm{AH_2(aq)} + *, \tag{2.40}$$

where the * marks the electrocatalyst surface, A is a gas phase reactant which undergoes a first PET resulting, in an adsorbed intermediate *AH, which is then reduced via a second proton-electron transfer to the product AH_2 released into the aqueous medium. Each step is associated with a value of a thermodynamic potential, which provides physical information about the system under certain temperature and pressure conditions.
Assuming that the reaction in Eq. (2.40) occurs at constant pressure p, temperature T, and number of particles N, the suitable thermodynamic potential is the Gibbs free energy $G(p,T)$. The process is *endergonic* if the overall reaction requires energy and is not spontaneous or unfavorable and the difference between the Gibbs free energy of products and reactants, ΔG is positive. On the contrary, the reaction is *exergonic* if it releases energy and hence is a spontaneous process ($\Delta G < 0$).

The Gibbs free energy of a system is defined as

$$G(p,T) \equiv U - TS + pV, \tag{2.41}$$

in which U is the internal energy, while TS and pV are the entropic and volumic terms. Referring to the example reaction in Eq. (2.40), the Gibbs free energy of the reactants G_{R}, intermediate state G_{I} and products G_{P} states are

$$G_{\mathrm{R}} = G_{\mathrm{A\,(g)}} + 2[G_{\mathrm{H^+}} + G_{e^-}] + G_*, \tag{2.42}$$

$$G_{\mathrm{I}} = G_{{}^{*}\mathrm{AH}} + [G_{\mathrm{H^+}} + G_{e^-}], \tag{2.43}$$

$$G_{\mathrm{P}} = G_{\mathrm{AH_2(aq)}} + G_*. \tag{2.44}$$

From the energy differences between the G_i of each state it is possible to determine the thermodynamic free energy profile of the reaction investigated. The following sections will discuss how to estimate the various terms in Eqs. (2.42)-(2.44).

Gibbs free energy estimation

The general definition in Eq. (2.41) can be reformulated as

$$G = E^{\mathrm{DFT}} + E^{\mathrm{ZP}} + \int_0^T C_p \, dT \; - TS. \tag{2.45}$$

Here, the total internal energy U has been replaced by E^{DFT}, the ground-state electronic energy calculated by means of DFT, and E^{ZP}, the zero-point energy. The volumic term pV in Eq. (2.41) has been rewritten by means of the heat capacity at constant pressure C_p.
The form of G can then be further specialized for each composing term in Eqs. (2.42)-(2.44), according to its phase.

Starting from the catalyst surface, its Gibbs free energy can be simplified to

$$G_* \simeq E_*^{\mathrm{DFT}} + E_*^{\mathrm{ZPE}} - TS_*^{\mathrm{vib}}, \tag{2.46}$$

where the volumic term has been dropped since it is negligible for solid surfaces and E_*^{ZPE} and S_*^{vib} can, in principle, be obtained from the phonon dispersion of the solid.

For a single molecule in the gas phase A(g), Eq. 2.45 provides its chemical potential [129, 130]

$$\mu_{\mathrm{A(g)}} = E_{\mathrm{A(g)}}^{\mathrm{DFT}} + E_{\mathrm{A(g)}}^{\mathrm{ZPE}} + \left[H_{\mathrm{A(g)}}(T) - H_{\mathrm{A(g)}}(0)\right] - TS_{\mathrm{A(g)}}. \tag{2.47}$$

The enthalpic $\left[H_{\mathrm{A(g)}}(T) - H_{\mathrm{A(g)}}(0)\right]$ and entropic $S_{\mathrm{A(g)}}$ contributions at standard conditions can be obtained from thermochemical tables [131]. The zero-point energy is obtained from the vibrational normal modes of the molecule with N atoms

$$E_{\mathrm{A(g)}}^{\mathrm{ZPE}} = \frac{1}{2}\sum_{i=1}^{M} \hbar\omega_i, \tag{2.48}$$

where $M = N - 5$ if the molecule is linear, otherwise $M = N - 6$.

If the species is in aqueous or liquid phase, under standard conditions its chemical potential can be obtained from the corresponding gas phase by correcting the free energy with experimental data as

$$\mu_{\mathrm{A(aq/l)}} = \mu_{\mathrm{A}(g)} + \Delta^f G_{\mathrm{A(aq/l)}} - \Delta^f G_{\mathrm{M\,(g)}}, \tag{2.49}$$

where $\Delta^f G_{\mathrm{A(aq/l)}}$, $\Delta^f G_{\mathrm{A\,(g)}}$ are the Gibbs free energy of formation of the molecule in liquid/aqueous phase or in the gas phase, respectively. Their values are found in thermochemical databases [132].

When dealing with an intermediate anchored to the electrode surface, such as *AH in Eq. (2.40), the vibrational contributions of the surface and the adsorbate can be assumed to decouple. Moreover, since the intermediate is bound to the surface, all its degrees of freedom can be treated as vibrational. Therefore, we have

$$G_{*\mathrm{AH}} = E^{\mathrm{DFT}}_{*\mathrm{AH}} + E^{\mathrm{ZP}}_{*|\mathrm{AH}} + \int_0^T C^{\mathrm{vib}}_{p,*|\mathrm{AH}}\, dT \; - T S^{\mathrm{vib}}_{*|\mathrm{AH}} + E^{\mathrm{ZP}}_{*} - T S^{\mathrm{vib}}_{*}, \tag{2.50}$$

where the subscript $^*|$AH indicates that the relative quantity is referred to the adsorbed molecule only. The vibrational quantities related to the adsorbate are most easily estimated with the harmonic approximation as

$$E^{\mathrm{ZPE}}_{*|\mathrm{AH}} = \frac{1}{2}\sum_k \hbar\omega_k, \tag{2.51}$$

$$S^{\mathrm{vib}}_{*|\mathrm{AH}} = k_B \sum_k \left[\frac{\hbar\omega_k}{k_B T (e^{\hbar\omega_k/k_B T} - 1)} - \ln\left(1 - e^{-\hbar\omega_k/k_B T}\right) \right], \tag{2.52}$$

$$\int_0^T C^{\mathrm{vib}}_{p,*|\mathrm{AH}}\, dT = k_B T + \sum_k \frac{\hbar\omega_k}{(e^{\hbar\omega_k/k_B T} - 1)}, \tag{2.53}$$

where k_B is the Boltzman constant and ω_k are the normal modes of the adsorbate only. Finally, since we assume that all the electrochemical reactions occur in an aqueous environment, the interaction of the solvent with the catalyst surface and its adsorbed species is considered by the solvation energy $E^{\mathrm{solv}}_{*\mathrm{AH}}$ term and Eq. (2.50) becomes

$$G_{*\mathrm{AH}} = E^{\mathrm{DFT}}_{*\mathrm{AH}} + F^{\mathrm{vib}}_{*} + F^{\mathrm{vib}}_{*|\mathrm{AH}} + E^{\mathrm{solv}}_{*X}, \tag{2.54}$$

where F^{vib}_{*} and $F^{\mathrm{vib}}_{*|\mathrm{AH}}$, respectibely enclose all the vibrational terms of the surface and the adsorbate in Eq. (2.50). The evaluation of $E^{\mathrm{solv}}_{*\mathrm{AH}}$ can be very challenging, and

different methods can be used: (i) the employment of an implicit solvent with a static dielectric constant ε which simulates the aqueous medium without explicit hydrogen bonds, (ii) the application of semi-explicit corrections obtained by calculating with DFT the energy of a hydrogen bond between the adsorbate and water molecules and evaluating the average number of bonds with classical molecular dynamics, and (iii) the use of a fully explicit solvent introducing different water layers and atom configurations sampled with dynamics based on atomic forces coming from DFT. According to the system investigated, in this thesis we estimated the $E^{\mathrm{solv}}_{*\mathrm{AH}}$ by employing semi-explicit DFT simulations or implicit solvent.

Due to the decoupling assumption in Eq. (2.50), when computing physically meaningful free energy differences between the intermediate state and reactants or products, the vibrational contributions of the catalyst surface cancel out. It is not necessary to compute the phonon dispersion of the surface, thus reducing the computational cost. However, it is important to notice that the validity of the decoupling approximation should always be checked, especially in case of catalysts consisting of light atoms (e.g. graphene).

The calculation of the free energy of reaction for an electrochemical process is complex due to the presence of electrolyte molecules and electric field in the real electrochemical system. Therefore, it is computationally very demanding to simulate the adsorption process at the catalyst surface with the full details of electrolyte-catalyst interface. In the next section, the Computational Hydrogen Electrode model is presented to describe the $(G_{\mathrm{H}^+} + G_{e^-})$ term and determine the reaction free energy of the electrochemical system at a given external potential applied (U).

The Computational Hydrogen Electrode

The Computational Hydrogen Electrode (CHE) model [107] is a strictly thermodynamic approach which allows to predict the free energy profile of a reaction at a certain potential. This model relies on the following fundamental assumptions: *(i)* the bulk of the electrolyte is in equilibrium; *(ii)* the electrode surface is in equilibrium with the bulk of the electrode and of the electrolyte; *(iii)* the adsorption energy on the surface is independent of the electric field.

In an electrochemical cell, at the Reversible Hydrogen Electrode (RHE), by definition the reaction

$$\frac{1}{2}\mathrm{H_2(g)} \rightleftharpoons \mathrm{H^+ + e^-} \tag{2.55}$$

is in equilibrium, implying

$$\frac{1}{2}\mu^{\circ}_{\mathrm{H_2(g)}} = \mu^{\mathrm{ref}}_{\mathrm{H^+}} + \mu^{\mathrm{ref}}_{\mathrm{e^-}}, \tag{2.56}$$

where $\mu^{\circ}_{\mathrm{H_2}}(g)$, $\mu^{\mathrm{ref}}_{\mathrm{H^+}}$, and $\mu^{\mathrm{ref}}_{\mathrm{e^-}}$ are the chemical potentials of the molecular hydrogen in the gas phase at standard conditions, the proton in solution and the electron in the reference electrode, respectively.

At the cathode, where the relevant reduction reactions take place, the chemical potential of protons ($\mu_{\mathrm{H^+}}$) and the chemical potential of electrons ($\mu_{\mathrm{e^-}}$) are generally different. However, the assumptions *(i)* and *(ii)* of the CHE ensure that the electrolyte and the surface of the electrocatalyst are in equilibrium, so that

$$\mu_{\mathrm{H^+}} = \mu^{\mathrm{ref}}_{\mathrm{H^+}}. \tag{2.57}$$

The chemical potential of the electrons on the cathode is given by the chemical potential of the electrons in the RHE modified by the applied potential U_{RHE} referred to the RHE

$$\mu_{\mathrm{e^-}} = \mu^{\mathrm{ref}}_{\mathrm{e^-}} - eU_{\mathrm{RHE}}, \tag{2.58}$$

where e is the elementary positive charge. Hence, by combining of Eqs. (2.56), (2.57) and (2.58) the $(G_{\mathrm{H^+}} + G_{\mathrm{e^-}})$ term becomes

$$\mu_{\mathrm{H^+}} + \mu_{\mathrm{e^-}} = \frac{1}{2}\mu^{\circ}_{\mathrm{H_2(g)}} - eU_{\mathrm{RHE}}. \tag{2.59}$$

At standard conditions and zero applied electric potential vs RHE (U_{RHE} = 0 V), the method assumes that the half chemical potential of a hydrogen molecule in the gas phase ($\frac{1}{2}\mu^{\circ}_{\mathrm{H_2(g)}}$) replaces the chemical potential of each proton-electron couple ($\mathrm{H^+}$ + $\mathrm{e^-}$). At non-zero potentials ($U_{\mathrm{RHE}} \neq 0$ V), the chemical potential of each ($\mathrm{H^+}$ + $\mathrm{e^-}$) couple is shifted by an amount $-eU_{\mathrm{RHE}}$.

Gibbs free energy reaction profile

The CHE model predicts the reaction Gibbs free energy change ΔG of each step involving a coupled electron-proton transfer. The Gibbs free energy variation between two reaction states s (starting) and f (final) can be written as

$$\Delta G^r_{s\to f} = G_f - G_s + (n_f - n_s)\left(\frac{1}{2}\mu^\circ_{\mathrm{H_2(g)}} - eU_{\mathrm{RHE}}\right), \tag{2.60}$$

where G_f and G_s do not contain the free energy contributions of proton-electron couples, whose numbers in the starting and final states are n_s and n_f, respectively. Therefore, at standard conditions, $\Delta G^r_{s\to f}$ depends only on the potential U_{RHE}. Consequently, by varying U_{RHE}, the value of $\Delta G^r_{s\to f}$ and thus the thermodynamic reaction steps can be varied

$$\Delta G^r_{s\to f}(U_{\mathrm{RHE}}) = \Delta G^r_{s\to f}(U_{\mathrm{RHE}} = 0V) - (n_f - n_s)eU_{\mathrm{RHE}}. \tag{2.61}$$

A simple, approximate criterion for a spontaneous reaction is that all steps in the reaction have $\Delta G \leq 0$. The potential limiting step is the reaction step which requires the highest negative potential value to make the process feasible and determines the thermodynamic U_{onset} of the reaction as

$$U_{\mathrm{onset}} = -\max\left(\frac{\Delta G^r_{m\to n}}{e}\right), \tag{2.62}$$

in which $\Delta G^r_{m\to n}$ is the free energy variation of a reaction step from state m to state n.

2.5.3 Theoretical approach to reaction kinetics

The feasibility of a catalytic reaction depends on both the thermodynamic cost of each step in the process and the kinetic aspects related to the energy barriers between different states in the reaction pathway. To comprehensively assess a chemical reaction, it is necessary to consider kinetic energy barriers, which can be determined by analyzing the PES of each step. Finding the activation energy and the transition state (TS) for a specific reaction step is one of the most significant challenges in

catalysis. A TS is a narrow subspace that separates the initial and final states of a reaction step in such a way that all reactive trajectories necessarily go through it. Within the harmonic approximation, the TS is a hyperplane going through the first order saddle point on the energy surface in between the two minima corresponding to initial and final states. The saddle point is the energetically highest point along the minimum energy path (MEP) on the PES. Within that approximation, the energy of the saddle point minus the energy if the initial state gives the (forward) activation energy barrier of the process. Several computational methods have been developed to search for TS and MEPs. These transition state search tools are usually classified based on the required information, such as a predefined final state geometry or a guess of the transition state. In the following section, the methods employed in this thesis for the TS search, that is the *nudged elastic band* [109, 110] and the *dimer* [108] methods, are presented.

Nudged elastic band method

Given an initial and final state of a reaction, the nudged elastic band (NEB) method is an efficient tool for finding the saddle point through which the system has to advance. According to this method, an initial path is generated by a set of images of the system created and placed along some path that connects the initial and final structures.
Each image is iteratively moved according to the projection of the atomic force perpendicular to the path. Hence, calling $\hat{\mathbf{u}}_{\parallel}$ the unit vector tangent to the path, the atomic force perpendicular to the path at image j is

$$\mathbf{F}^{p}_{\perp,j} = \nabla E(\mathbf{R}_j) - \left(\nabla E(\mathbf{R}_j)\cdot\hat{\mathbf{u}}_{\parallel}\right)\hat{\mathbf{u}}_{\parallel}. \tag{2.63}$$

The distribution of the images along the path is controlled by a restraint method where harmonic springs are inserted between neighboring images. Their role is to maintain a specified spacing of the images along the direction parallel to the path. This is accomplished by the spring force, defined as

$$\mathbf{F}^{s}_{\parallel,j} = \hat{\mathbf{u}}_{\parallel}\left[k^{s}_{j+1}\left(\mathbf{R}_{j+1}-\mathbf{R}_j\right) - k^{s}_{j}\left(|\mathbf{R}_j-\mathbf{R}_{j-1}\right)\right]\cdot\hat{\mathbf{u}}_{\parallel}, \tag{2.64}$$

where k^{s}_{j+1}, k^{s}_{j} are the spring constants. If all the spring constants are equal, a uniform spacing of the images is obtained. The effective force acting on image j is

the *nudging* force

$$\mathbf{F}_j = \mathbf{F}^s_{\parallel,j} + \mathbf{F}^p_{\perp,j}. \tag{2.65}$$

The direction of the fictitious spring forces, parallel to the path, ensures that the images are evenly spaced without interfering with the actual relaxation dynamics of the path towards the MEP.

To force the highest energy image to actually reach the saddle point, the climbing image NEB (CI-NEB) is used, where the image characterised by the highest energy is released from the spring system and displaced along a reversal of its true force along the direction of the path. In this way, the image maximizes its energy along the path, and minimizes it in all other directions.

Dimer method

The dimer method is a local saddle-point search algorithm based on the employment of first derivatives of the potential energy of a pair of images, known as dimer, of the system displaced slightly by a fixed distance (ΔR) from the midpoint ($\mathbf{R}$)

$$\mathbf{R}_i = \mathbf{R} \pm \Delta R \hat{\mathbf{u}}_N, \qquad i = 1,2, \tag{2.66}$$

where the vector $\hat{\mathbf{u}}_N$ is a unit vector along the dimer axis.

From the energies (E_1, E_2) and the forces ($\mathbf{F}_1$, $\mathbf{F}_2$) acting on the two images, it is possible to calculate the energy (E_0), the force acting on the midpoint of the dimer ($\mathbf{F}_R$) and the curvature of the potential (C) along the dimer axis, as

$$E_0 = \frac{E}{2} + \frac{\Delta R}{4}(\mathbf{F}_1 - \mathbf{F}_2) \cdot \hat{\mathbf{u}}_N, \tag{2.67}$$

$$\mathbf{F}_R = \frac{(\mathbf{F}_1 + \mathbf{F}_2)}{2}, \tag{2.68}$$

and

$$C = \frac{(\mathbf{F}_1 - \mathbf{F}_2) \cdot \hat{\mathbf{u}}_N}{2\Delta R} = \frac{(E - 2E_0)}{(\Delta R)^2}, \tag{2.69}$$

where E is the energy of the dimer.

The saddle-point search algorithm of this method involves two operations, namely rotating and translating.

In the first step, the dimer axis is rotated into the lowest curvature mode of the potential energy at the midpoint of the dimer **R**. The rotational force can be calculated by

$$\mathbf{F} = \frac{(\mathbf{F}_1^{\perp} - \mathbf{F}_2^{\perp}) \times \hat{\mathbf{u}}_\theta}{\Delta R}, \tag{2.70}$$

where $\hat{\mathbf{u}}_\theta$ is the rotational direction perpendicular to $\hat{\mathbf{u}}_N$ within the plane of rotation. After the convergence of the rotation, that is after identifying the lowest curvature mode, the dimer is translated for a certain step length moving up the potential surface searching for the saddle point at the maximum along the lowest curvature mode. The $\mathbf{F}_R$ in Eq. (2.68) is the net translation force, which pulls the dimer towards a minimum. Therefore, a modified force, $\mathbf{F}^t$, is defined, where the force component along the dimer is inverted

$$\mathbf{F}^t = \mathbf{F}_R - 2\mathbf{F}^{\parallel}, \tag{2.71}$$

and the movement of the dimer along $\mathbf{F}^t$ pushes it towards the saddle point.

2.5.4 Constant electrode potential

Kinetic energy barriers are strongly affected by the application of an external potential, which implies the presence of a charge at the surface of the electrocatalyst. From a thermodynamic perspective, the CHE approach is computationally suitable to predict electrochemical reactions, but it neglects the effect of the charge on the surface of the electrode. By a self-consistent procedure, the constant electrode potential (CEP) model addresses this issue by varying the number of electrons (N^e) in the simulation cell, so that the Fermi level (E_F), which is equal to the chemical potential of the electrons, matches the desired electrode potential with respect to the vacuum level [133].

The aqueous electrolyte is generally included in the simulation via an implicit solvation model[2]. The employment of an implicit solvent means that water molecules are not present in the simulation box, but their effect is considered via an effective dielectric constant. When the electrode potential is different from the potential of zero charge, it is important to include a counterion charge distribution through the use of the generalized Poisson-Boltzmann equation. In DFT calculations, the

[2]For instance, available in VASP through the VASPsol extension [134, 135].

method controls the electrode potential by alterating N^e along with changing the concentration of counterions in the surrounding, implicit electrolyte.

Most available codes and implicit-solvent modules do not yet fully support grand-canonical DFT calculations. Instead, the number of electrons N^e is adjusted in between successive iterations in the electronic structure calculation, as

$$N^e_{i+1} = N^e_i - a[\mu^e_i - \mu^e_{\text{target}}], \tag{2.72}$$

where the a parameter can be taken to be on the order of 1 V^{-1}. In this way, as the structure optimization proceeds, the electronic chemical potential (μ^e) converges to the target value (μ^e_{target}). The electronic chemical potential μ^e is calculated as $\mu^e = E_F - V_{bulk}$, that is the difference between the Fermi level (E_F) and the potential in the bulk electrolyte (V_{bulk}), since the implicit solvent model uses the V_{bulk} as reference and sets it to zero. The μ^e_{target} is obtained as

$$\mu^e_{\text{target}} = -\Phi_{SHE} - U, \tag{2.73}$$

for a desired potential U with respect to the Standard Hydrogen Electrode (SHE), where Φ_{SHE} is the work function of the SHE, equal to 4.43 V.

Finally, to compare energy differences of two configurations at the same electrode potential, U, but different N^e, the computed energies have to be corrected by the cost(gain) of removing (adding) electrons as

$$\Omega = E_{\text{DFT}} - N^e \mu^e(U) \tag{2.74}$$

where Ω is an electronic grand-potential.

In Chapter 5, the CEP model has been employed to estimate the activation energy of the various elementary reaction steps as a function of applied potential.

CHAPTER 3

Understanding the Active Surface Structure of SnO_2 Electrocatalyst for CO_2 Reduction

The following Chapter is aimed to understand the catalytic active surface structure of SnO_2 under working electrocatalytic conditions for CO_2 reduction. To perform this investigation, we employed the $SnO_2(110)$ surface as model of the oxide electrode. We studied how the reactivity and selectivity of this structure towards CO_2RR changes at varying stoichiometry. Details on the computational details on the *ab initio* calculations performed to achieve the above mentioned goal are provided in Appendix B, Section B.1.

The Chapter is organized as follows: after a brief introduction on the use of SnO_2 electrocatalyst and the current open questions in Sections 3.1 and 3.2, respectively, the choice of the surface model to investigate electrocatalytic activity of the SnO_2 electrode is presented in Section 3.3. The investigated reduction reaction mechanisms are presented in Sections 3.4, while their thermodynamic analysis are discussed in Sections 3.5 and 3.6. Finally, short conclusions are summarised in Section 3.7.

3.1 SnO_2 electrocatalyst for CO_2 reduction to HCOOH

A broad spectrum of electrocatalysts for CO_2RR consists of metals and metal oxide-based materials, as reported in Section 1.3.1 of Chapter 1. The wide application of this class of catalysts is mainly due to several inherent advantages of their synthesis process, which are typically characterized by lower costs and more standard preparation conditions compared to other electrocatalyst classes such as SACs and MOFs [54]. As previously introduced, metals and their relative oxides are principally classified according to their selectivity towards specific electrochemical CO_2 reduction reaction products and, among these, HCOOH is one of the most interesting at industrial level. The CO_2 conversion to HCOOH is an attractive pathway, because HCOOH may serve as chemical fuel for direct formic acid fuel cells [136] as well as liquid raw material for H_2/CO storage, which can be released through the catalytic decomposition of HCOOH [137–139].

P-block post-transition metals-based electrocatalysts, such as Sn, In, Pb, and Bi, show particularly high selectivity for CO_2 reduction to HCOOH [40]. In particular, Sn is a low-cost and eco-friendly element, whose abundance in the Earth's crust as well as high activity and selectivity have recently raised attention for its applications in electrochemistry [140, 141]. The growing interest in this element can also be attributed to its high oxygen affinity [142], which induces the coordination of the CO_2 to the electrode surface through a bidentate *OCHO intermediate, required for HCOOH evolution as discussed in Section 1.2.2 of Chapter 1. Indeed, experimental studies conducted by Hori et al. [66] demonstrated that a bulk metallic Sn electrode produces HCOOH with FE of about 88.4% at -1.1 V vs. RHE at relatively large overpotential and low current density.

The surface of Sn is easily susceptible to oxidation when it is exposed to air. Consequently, a common practice for CO_2RR application consists of employing tin dioxide (SnO_2) covered electrode, also so-called *precatalyst*, instead of directly using Sn metal. This strategy has several advantages. First of all, literature provides a considerably large library of widely-accepted synthetic methods for various SnO_2 nanostructures. This allows to tune both size and morphology of the electrocatalyst [140]. The resulting SnO_2 samples typically present a higher specific area and roughness which are known to positively affect both the activity and selectivity during

CO_2RR [143, 144]. As an example, Zhang and co-workers [145] synthesized 3D hierarchical mesoporous SnO_2 nanosheets, observing an improved electrocatalytic performance. They suggested that the 3D hierarchical structure makes easier the charge transfer at the surface thanks to the increase of the accessible surface area, which favours the mass transport of reactant and product. Moreover, the oxide electrode is supposed to get reduced to metal phase at working electrocatalytic potentials, creating structural defects with unusual high activities, like grain boundaries. These effectively promote the CO_2 reduction reaction by the stabilization of specific reaction intermediates [146, 147]. As an example, Spurgeon and colleagues [148] prepared porous SnO_2 nanowires electrochemically reduced to metallic Sn nanowires with a high density of grain boundaries which exhibited high activity and selectivity for the production of formate, reaching a Faradaic efficiency of 80 % at -1.0 V versus RHE.

Notwithstanding the acknowledged efficiency of SnO_2 electrocatalysts, a current matter of debate in the literature regards the nature of the electrocatalytic active surface, resulting in conflicting interpretations which will be discussed in the following.

3.2 The SnO_2 active surface structure: a matter of debate

Based on the standard redox potential, the Sn-O Pourbaix diagram shows that an SnO_2 electrode would get reduced to its metallic phase before CO_2RR takes place [149]. The CO_2 reduction to HCOOH or $HCOO^-$ is pH-dependent, because HCOOH exists at pH < 3.75, whereas it is deprotonated at pH > 3.75 [150]. The former is the least favored thermodynamically in acids, but the increase of solution pH turns the product into $HCOO^-$ and the reaction is easier to take place. In this perspective, under electrocatalytic CO_2 reduction conditions toward $HCOO^-$ production, namely at low applied potential (U < -0.4 V) and pH > 4, the metallic tin is the most thermodynamically stable phase. Therefore, under working electrode conditions, it is expected that the SnO_2 particles deposited on the electrode should be completely reduced. However, literature reports several experimental studies in which it is stated

that during the CO_2RR tin oxide phases are still present. In the following, some examples taken from the literature are discussed.

Lee and co-workers [151] performed CO_2 reduction on SnO_2 at different alkaline pH values. They found that at high pH values, that is 10.2 and 11.72, the X-ray diffraction (XRD) spectra of the catalysts show only tin oxide phases. At these conditions, the electrode is highly selective toward formic acid. On the other hand, the catalyst is partially reduced to metallic Sn under mild basic conditions (pH = 8.42). At this stage, a decrease of FE_{HCOOH} as well as an increase in H_2 production are reported. In contrast, Gao et al. [152] stated that it is fundamental that SnO_2 gets moderately reduced for the conversion of CO_2 to HCOOH conversion. In particular, they observed that the oxide surface loses oxygen species leading to a system rich of oxygen vacancies which are believed to be responsible for the selective production of formic acid.

Generally, investigating the surface structure evolution of electrode materials under operating conditions, such as by means of in situ or operando spectroscopy characterization techniques, is a powerful tool for better understanding CO_2RR electrocatalysts. For example, Raman spectroscopy can provide the structural fingerprints of surface species. Few research groups performed operando Raman characterization to gain an insight into the structure and reactivity of the SnO_2 catalytic active surface. Both Dutta et al. [153] and Kuzume et al. [154] observed that the highest selectivity toward $HCOO^-$ occurred approximately between -0.5 and -1.1 vs Ag|AgCl (at different pH values). In this potential range, SnO_2 samples should be completely reduced according to Pourbaix analysis, but their measurements revealed that the materials appear to be only partially reduced. Therefore, they suggest that SnO_2 reduction is kinetically hindered. Based on this evidence, according to the authors, both metallic (Sn^0) and oxide (Sn^{II}) phases are present during the CO_2RR, but it is not possible to clearly define which species plays the major catalytic role. Moreover, the authors found that at very negative potentials, all SnO_2 is reduced to metallic Sn favouring hydrogen production with respect to HCOOH.

In the last few years, theoretical investigations also contributed to investigate the CO_2RR reaction pathways on SnO_2 electrocatalysts. Gong and colleagues [155] studied the effect of surface oxygen vacancies on the activity and selectivity of SnO_2. The authors concluded that moderate amount of oxygen vacancies is able to

selectively promote the CO_2 reduction to HCOOH since their presence affects the bond strength between *OCHO intermediate and the electrode surface, hindering both the HER and Sn^{II} reduction to Sn^0 at the same time. Contrary to the work of Gong's group, DFT results of Ge et al. [156] showed that the key intermediate for formate production is a bicarbonate intermediate formed from the CO_2 reaction with hydroxyl groups present at the catalyst surface. The authors stated that the oxide phase of the catalyst is required to promote CO_2RR.

The works here presented show that a uniform computational model on the structure and stoichiometry of the SnO_2 surface involved in CO_2RR at experimental conditions does not exist yet. Therefore in the remaining part of this Chapter we present our view and results on the SnO_2 surface structure responsible for HCOOH selectivity at experimental operating conditions.

3.3 Surface free energy analysis of low-index SnO_2 surfaces

With the aim of representing a realistic surface model for an SnO_2 electrode during electrochemical CO_2RR, the structures and thermodynamic stability of the low-index (100), (101) and (110) crystallographic facets of tin oxide are first discussed.

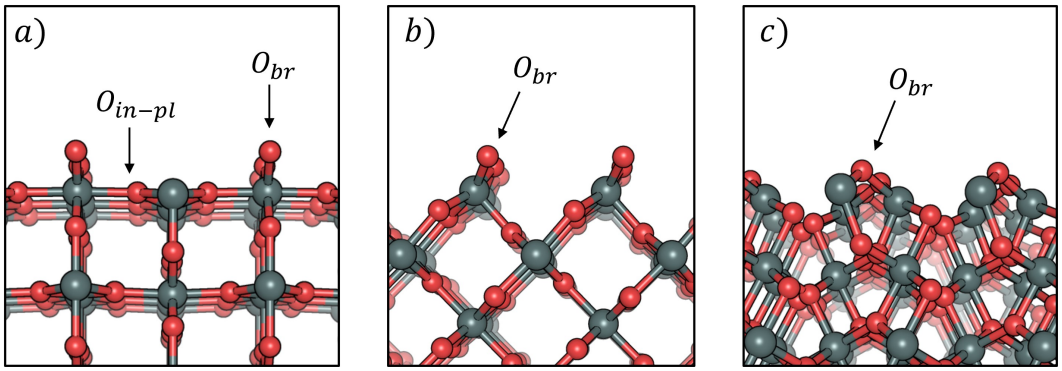


Figure 3.1 Structures of stoichiometric low-index surfaces of SnO_2. Panel a) corresponds to (110) facet, while panels b) and c) are (100) and (101) facets, respectively. Atom color code: O red and Sn grey.

Figure 3.1 shows the stoichiometric structures of the investigated SnO_2 low-index surfaces. On the stoichiometric (110) surface (Figure 3.1*a*), both five- and six-fold coordinated Sn atoms (Sn_{5f} and Sn_{6f}, respectively) are exposed. The Sn_{6f} polyhedron gives rise to rows of two-folded oxygen atoms. These oxygens are above the plane occupied by the tin cations and are called 'bridging oxygens' (O_{br}), whereas the oxygens located in the same plane of the outermost tin cations are labelled 'in-plane oxygens' (O_{in-pl}). The (100) (Figure 3.1*b*) and (101) surfaces (Figure 3.1*c*) show Sn_{5f} and O_{br} species only, and appear to be highly corrugated.

For these three surfaces we calculated the surface energies (γ) as functions of the oxygen chemical potential, μ_O, both for stoichiometric and reduced structures. Calculation details are reported in Section A.5 of Appendix A. Our analysis allows to determine the thermodynamically most stable surface, that is the one with the lowest γ at a given μ_O. The energy plot in Figure 3.2 shows that at high μ_O (experimental oxygen rich conditions) stoichiometric low-index surfaces are energetically favored. Hence, at this conditions, oxygen-rich surfaces are preferred and the energy stability increases in the order (110) > (100) > (101).
On the other hand, at experimental oxygen poor conditions, which means moving towards lower μ_O values, the loss of the outermost oxygen atoms leads to reduced surfaces energetically favored. More precisely, in (100) and (101) surfaces, the removal of the two-fold O_{br} rows to the respective reduced surface structures leaving three-fold coordinated Sn atoms (Sn_{3f}), converting from a SnO_2 stoichiometry to a SnO-like arrangement. Of the three surfaces, the SnO_2(110) has the most intricate behaviour, because its reduction proceeds by two steps of oxygen depletion. Firstly, the loss of O_{br} species leads to the so called *half-reduced* where only Sn_{5f} atoms are exposed. After that, the O_{in-pl} atoms are partially removed giving rise to the *reduced* phase, which shows Sn_{3f} ions in the external layer. Finally, oxygen poor conditions promote oxygen depleted SnO_2(110) surface, whose stability increases as the reduction degree increases.

In agreement with the literature [157], from a first thermodynamic analysis, the most stable facet is the SnO_2(110) surface, which has been employed as representative surface model of the SnO_2 electrocatalyst in this work. At this surface, the CO_2 reduction has been investigated along with its competing side reactions, that is the self-reduction reaction of the oxide electrode and the HER.

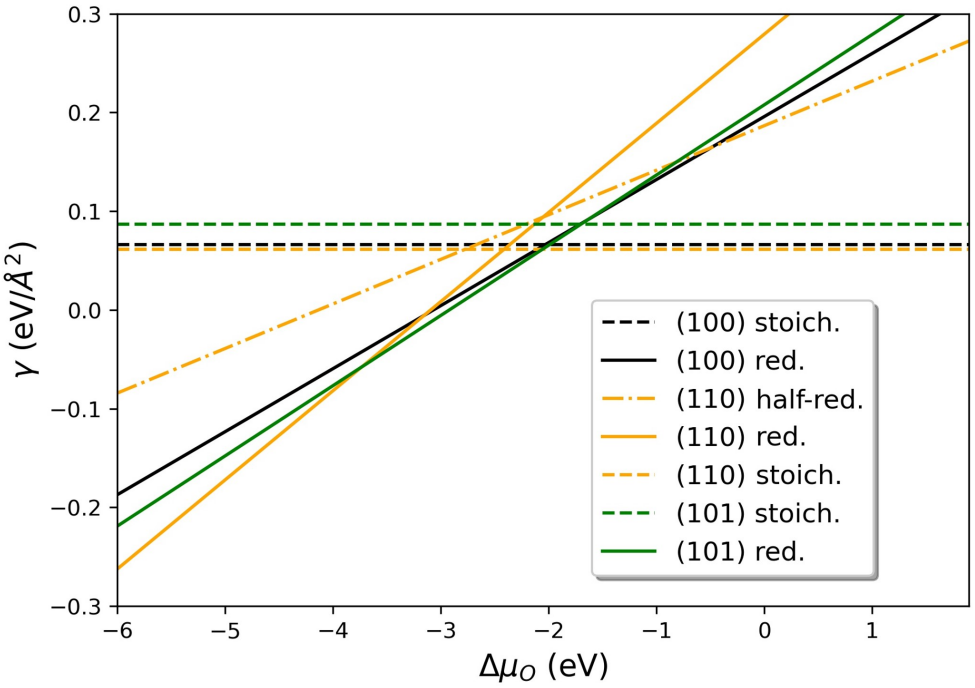


Figure 3.2 Surface energy as a function of the oxygen chemical potential for different SnO_2 surfaces. Dashed, dashed-dotted and solid lines correspond to stoichiometric, half-reduced and reduced phases, respectively. Color legend: *black* for (100) facet; *green* for (101) facet; *yellow* for (110) facet.

3.4 Possible electrocatalytic reduction reactions at the SnO_2(110) surface

Under applied baias, different competing reactions may occurs at the outermost oxide electrode surface, namely *catalytic* processes, such as the CO_2 reduction and the H_2 evolution, and *non-catalytic* mechanisms like the surface self-reduction processes.

At the oxide surface, the self-reduction commonly takes place via successive loss of surface oxygens, which leads to the formation of understoichiometric configurations. In fact, the CO_2 and H^+ in the electrolyte may react with the outermost oxygens ($^*O$) according to the two following processes

$$CO_2 + 2\,(H^+ + e^-) + {}^*O \longrightarrow H_2CO_3 + V_O \tag{3.1}$$

$$2\,(H^+ + e^-) + {}^*O \longrightarrow H_2O + V_O \tag{3.2}$$

originating carbonate and water, respectively, as final products. During these reactions, the (H^+ + e-) transfer originates surface oxygen vacancies (V_O). Reaction 3.1 unfolds into two steps, via firstly the attachment of the bicarbonate (*OCOOH) intermediate to the surface

$$CO_2 + (H^+ + e^-) + {}^*O \longrightarrow {}^*OCOOH \tag{3.1.a}$$

and its release as carbonic acid (H_2CO_3)

$${}^*OCOOH + (H^+ + e^-) \longrightarrow H_2CO_3 + V_O \tag{3.1.b}$$

in the electrolyte solution. In the same way, reaction 3.2 is also divided into two steps as follows

$$(H^+ + e^-) + {}^*O \longrightarrow {}^*OH \tag{3.2.a}$$

$${}^*OH + (H^+ + e^-) + \longrightarrow H_2O + V_O \tag{3.2.b}$$

via the surface hydroxyl (*OH) formation which is then released as H_2O.

Alternatively, if the oxide surface acts as an electrocatalyst the CO_2RR takes place. At the surface of the electrode, CO_2 can be converted to HCOOH or CO by two consecutive proton-electron transfers. In Section 1.2.2 of Chapter 1, Eq. (1.1.a) and (1.1.b) show the two (H^+ + e-) transfers for CO_2 reduction to HCOOH, while Eq. (1.2.a) and (1.2.b) for the conversion to CO. In particular, the first (H^+ + e-) exchange leads to the adsorption of CO_2 via a *OCHO or *COOH intermediate, which then turns into HCOOH or CO, respectively, upon reaction with a second (H^+ + e-) pair. Finally, in aqueous solutions, the competing HER can occur at the surface of the electrode, producing H_2 as side product. For more details about HER see Eq. (1.3) in Section 1.2.2.

In the following sections, we present the Gibbs free energy profiles of the competing reduction reactions discussed above when occurring on the SnO_2(110) surface at different stoichiometries, with the aim of understanding which are the key features that make this electrocatalyst selective towards formic acid production.

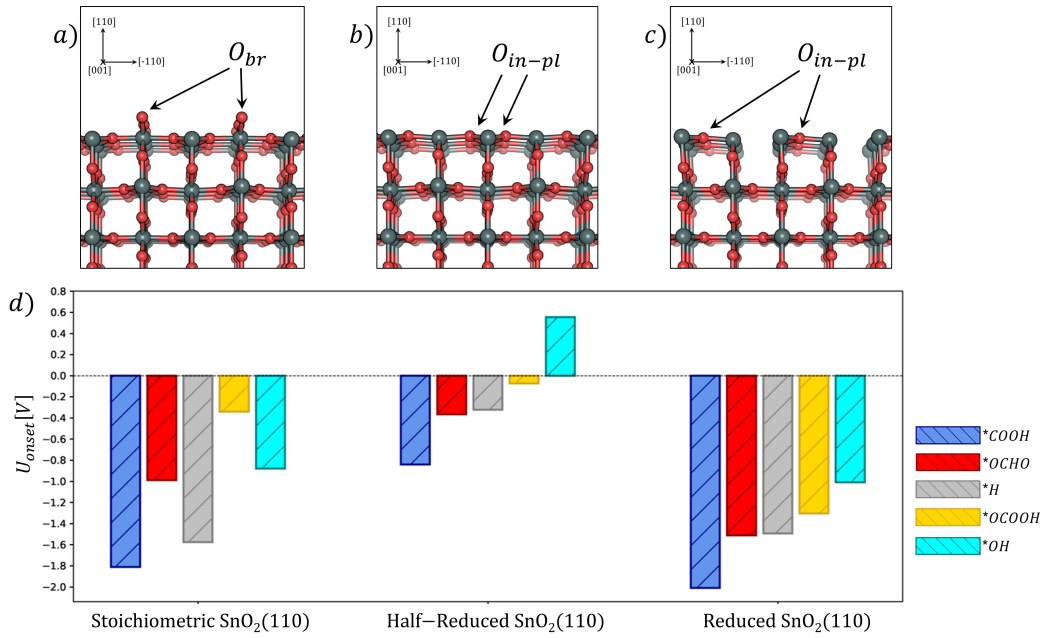


Figure 3.3 Side views of stoichiometric (a), half-reduced (b), and reduced (c) $SnO_2(110)$ surface. Atom color code: Sn gray and O red. Panel d): U_{onset} vs RHE for CO_2RR, HER and self-reduction mechanisms on $SnO_2(110)$ surfaces at increasing reduction degree. Reaction intermediate color code: *COOH blue, *OCHO red, *H gray, *OCOOH yellow, and *OH cyan. Figure taken from Ref. [158].

3.5 The self-reduction of $SnO_2(110)$ surface

The reaction energy profile of the possible competing processes occurring at the SnO_2 catalyst surface are estimated by the employment of the CHE model, as described in Section 2.5.2 of Chapter 2. From the energy landscape of each reaction, the U_{onset} is determined, i.e. the potential limiting step of the overall reaction pathway. For the stoichiometric, half-reduced and reduced $SnO_2(110)$ surfaces, the computed U_{onset} values of the reactions presented in Section 3.5 are reported in Figure 3.3.

We start our analysis from the stoichiometric $SnO_2(110)$ surface (Figure 3.3*a*). As previously stated, this surface exposes oxygen atoms in a so-called bridging configuration (O_{br}) and under-coordinated Sn ions. The potential-limiting steps for the CO_2RR and HER appear to be the adsorption of carbon dioxide and the adsorption of hydrogen respectively, while for self-reduction, it is the removal of the final product (H_2O or H_2CO_3). On the stoichiometric surface, our calculations show

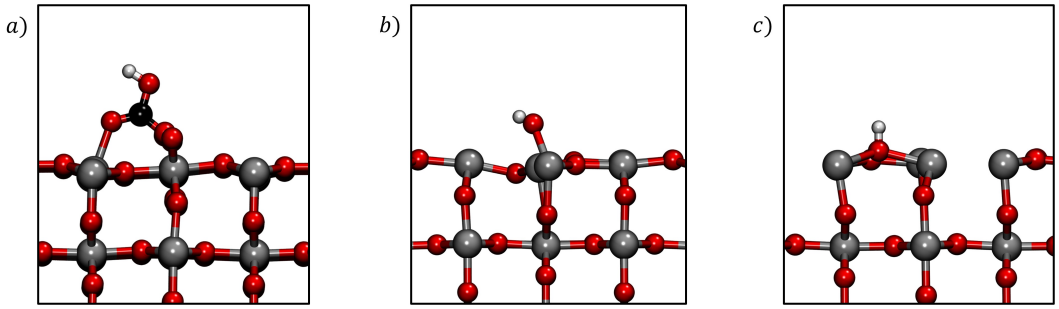


Figure 3.4 Optimized geometries for the favored adsorbates species at the $SnO_2(110)$ surfaces. Panels a) corresponds to *OCOOH intermediate at the stoichiometric $SnO_2(110)$, while panels b) and c) are the adsorbed *OH species to the half-reduced and reduced $SnO_2(110)$ surfaces, respectively. Atom color code: C black, H white, O red and Sn grey. Figure adapted from Ref. [158].

that the O_{br} atoms are the preferred species for binding CO_2 and H^+ adsorbates, in the form of *OCOOH and *OH, respectively, with negative adsorption free energies. The adsorption of *OCOOH species shows the lowest U_{onset} value (-0.34 V vs RHE), suggesting that, in the presence of dissolved CO_2, the self-reduction of the stoichiometric $SnO_2(110)$ surface occurs via the carbonate intermediate. This indicates that the evolution of $SnO_2(110)$ under applied bias initially leads to a complete loss of the oxygen bridging atoms, giving rise to a surface geometry which in the literature is indicated as half-reduced.

The analysis of the competing reaction U_{onset} on the half-reduced surface reveals that the self-reduction processes are still the favoured mechanisms at the potential required to remove O_{br} from the electrode surface. Indeed, at this step the outermost electrode exposes in-plane surface oxyigens (O_{in-pl}) which spontaneously adsorb protons. This proton adsorption moves the O_{in-pl} out of the plane and generates hydroxyl species (Figure 3.4*b*). These *OH are then released as H_2O molecules, leading to a further reduction of the SnO_2 surface to a structure that in literature is called reduced $SnO_2(110)$ (Figure 3.3*c*). From an analysis of the graph reported in Figure 3.3*d*, it is apparent that further reduction of this surface structure occurs at higher external biases, though still lower than those required to reduce CO_2 to CO or HCOOH (U_{onset} -2.00 and -1.51 V vs RHE, respectively), or for HER (-1.49 V). Indeed, the remaining O_{in-pl} atoms at -1.01 V vs RHE are further removed from the surface via proton adsorption and release of water molecules. As a result, at

relatively low potentials (about -1.01 V vs RHE) the preferred reaction occurring at the $SnO_2(110)$ surface consists of the successive removal of oxygen atoms (first O_{br} and then O_{in-pl}) which ultimately leads to a surface exposing tin atoms only. In this potential range, the surface does not work as a catalyst, but it gets modified under the effect of the external bias, evolving toward Sn rich terminations.

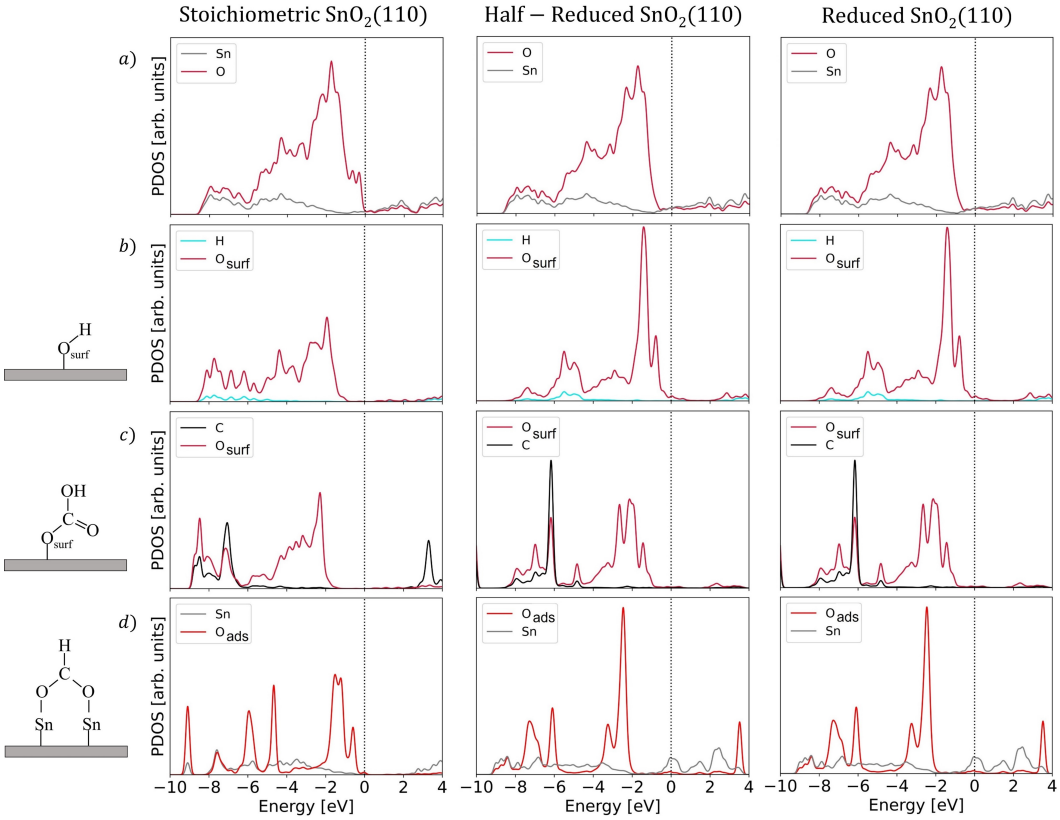


Figure 3.5 From left to right in row (a): PDOS of stoichiometric, half-reduced and reduced $SnO_2(110)$ pristine surfaces. From top to bottom: DOS projected on the atomic species involved in surface/adsorbate bonding in the case of *OH, *OCOOH and *OCHO intermediates (rows b, c and d, respectively) at the stoichiometric, half-reduced and reduced $SnO_2(110)$. On the left, schematic representation of the adsorbates *OH, *OCOOH and *OCHO (from top to bottom) on the $SnO_2(110)$ surface. The zero of energy corresponds to the maximum of the Valance Band of stoichiometric $SnO_2(110)$ surface. PDOS color code: C black, H cyan, O of the adsorbate (O_{ads}) red, Sn grey and O of the surface (O_{surf}) dark red. Figure taken from Ref. [158].

To get a better insight into the self-reduction of the $SnO_2(110)$ surface results, we performed an analysis of the electronic structure of different reaction intermediates at the SnO_2 surface. In particular, the Projected Density of States (PDOS) of the

stoichiometric, half-reduced and reduced $SnO_2(110)$ surfaces were computed and compared to the ones that involve *OH, *OCOOH and *OCHO reaction intermediates (Figure 3.5). As for the three surface structures before intermediate adsorption (Figure 3.5, row *a*), we projected the DOS on all Sn and O species. For surfaces with adsorbates, the DOS were projected on the atoms involved in the formation of the chemical bonds between intermediate anchoring atom and the surface atoms. In general, the PDOS on atomic species that are involved into bonding show peaks at the same energy, since their orbital gets hybridized. The lower in energy are those states the more stable are the chemical bonds formed (higher binding energy). Analysing the Figure 3.5, for all surface stoichiometries, it is possible to confirm bonds' formation, since states belonging to the oxygen of the surface are at the same energy of hydrogen- and carbon-states of *OH (Figure 3.5, row *b*) and *OCOOH (Figure 3.5, row *c*) intermediates, respectively. The same behaviour is observed for the states of surface Sn atoms and *OCHO adsorbate (Figure 3.5, row *d*). Importantly, formation of *OH and *OCOOH species (intermediates leading to surface self-reduction) is more favored than *OCHO one (intermediate that leads to formic acid) as proven by the deeper energy of the corresponding bonding states. These findings imply that until there are available oxygen atoms at the $SnO_2(110)$ surface, *OH and *OCOOH are preferred and the surface self-reduces. Given these results, we studied the catalytic activity of the system when an increasing number of metallic tin layers are formed at the oxide surface. In particular, we analyzed the $SnO_2(110)$ surface reactivity when one or two tin layers are exposed and compared the results to the surface of metallic tin. Results are discussed in the following paragraph.

3.6 CO_2RR and HER at under-stoichiometric SnO_2 surfaces

When a single tin layer is formed at the top of the $SnO_2(110)$ facet ($1Sn@SnO_2$, Figure 3.6*a*), the surface appears to be still inactive toward both the CO_2RR and HER (Figure 3.6*b*). Indeed, at the first proton-electron transfer, all three adsorption steps have negative free energies. Moreover, the product formation corresponds to the potential-limiting step and the production of HCOOH involves the highest thermody-

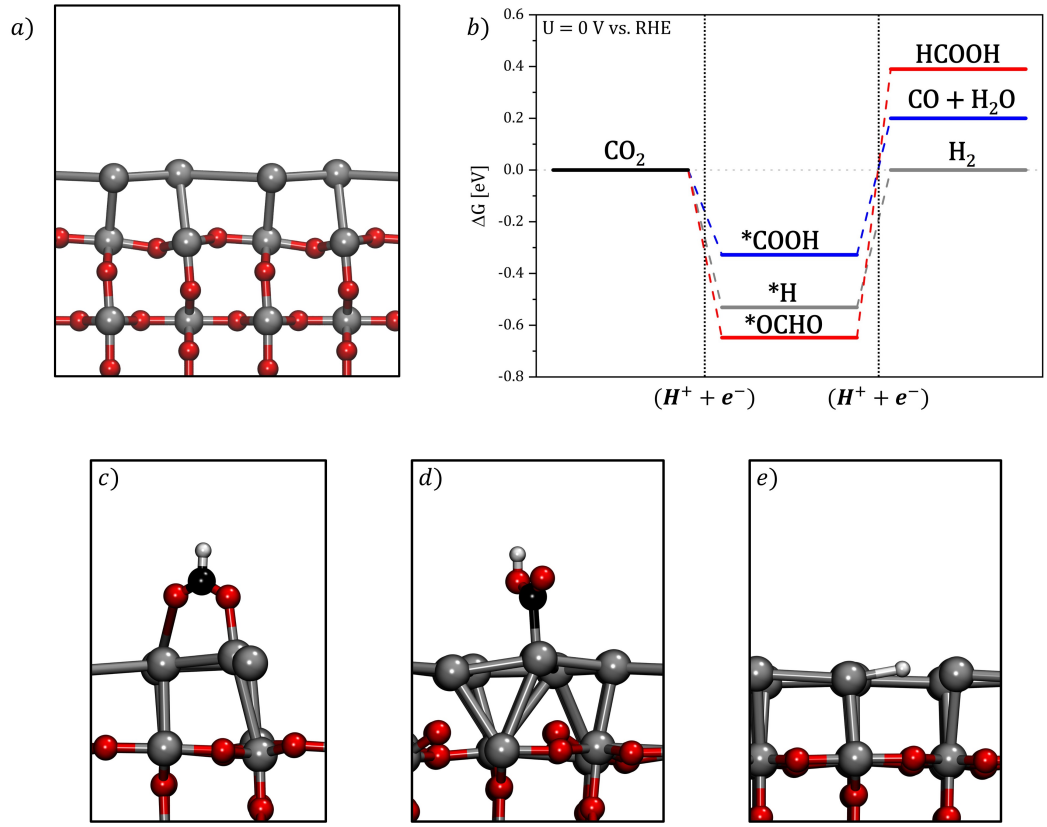


Figure 3.6 Panel a): Side view of $1Sn@SnO_2$. Atom color code: O red and Sn grey. Panel b): CO_2RR reaction paths at the $1Sn@SnO_2$ surface calculated at U = 0 V vs. RHE. The graph indicates the reaction intermediates *OCHO (red line) and *COOH (blue line) towards HCOOH and CO products, respectively. HER reaction path is also included (grey line). Optimized adsorbates structures: c) *OCHO, d) *COOH and e) *H at the $1Sn@SnO_2$ surface. Atom color code: C black, H white, O red and Sn grey. Figure adapted from Ref. [158].

namic free energies ($\Delta G^{*\mathrm{OCHO}\rightarrow\mathrm{HCOOH}}$ = 1.04 eV) compared to CO ($\Delta G^{*\mathrm{COOH}\rightarrow\mathrm{CO}}$ = 0.52 eV) and H_2 ($\Delta G^{*\mathrm{H}\rightarrow\mathrm{H_2}}$ = 0.53 eV).

When, instead, SnO_2 reduction proceeds to form a bilayer of tin on the surface ($2Sn@SnO_2$), the catalytic behavior completely changes, and the system becomes selective toward formic acid. This is evident from the analysis in Figure 3.7*a* (U_{onset} = -0.44 V vs RHE) in which, for comparison, we reported the free energy profile for the CO_2RR and HER (at U = 0 V vs RHE) both at the $2Sn@SnO_2$ (Figure 3.7*a*) and at a metal Sn(101) surface (Figure 3.7*b*). The latter represents one of the most stable tin surfaces according to previous literature studies [159]. In the case of the CO_2RR, both reduction paths to HCOOH (red path) and CO (blue path)

were considered. Analyzing the two panels of Figure 3.7, we observe that the three competing reaction pathways show similar energy profiles, suggesting that processes are not spontaneous at U = 0 V vs RHE and require the application of a negative U_{onset}. The first proton-electron transfer is uphill, and it determines the U_{onset} of the reaction on both surfaces. As for the CO_2RR, the formation of *COOH species is thermodynamically less favored with respect to *OCHO intermediates. Particularly, the energy needed to convert CO_2 to *COOH is markedly higher on the $2Sn@SnO_2$ surface ($\Delta G^{CO_2 \rightarrow {}^*COOH}$ = 1.22 eV) if compared to Sn(101) ($\Delta G^{CO_2 \rightarrow {}^*COOH}$ = 0.82 eV). On the contrary, the free energy profile corresponding to *OCHO adsorbate on the tin bi-layered oxide is consistently similar ($\Delta G^{CO_2 \rightarrow {}^*OCHO}$ = 0.44 eV) to the pristine metallic surface ($\Delta G^{CO_2 \rightarrow {}^*OCHO}$ = 0.40 eV). This result demonstrates that these reduced surfaces are selective toward the production of formic acid. With respect to the HER, Figure 3.7 highlights that the formation of *H intermediates is disfavored on the $2Sn@SnO_2$ ($\Delta G^{H^+ \rightarrow {}^*H}$ = 0.78 eV) if compared to Sn(101) ($\Delta G^{H^+ \rightarrow {}^*H}$ = 0.58 eV). This confirms that the selectivity toward HCOOH is higher in partially reduced SnO_2 surfaces exposing at least two metallic tin layers. When the surface reduction proceeds giving rise to thick tin metallic phases, the hydrogen evolution reaction becomes possible and HCOOH faradaic efficiency is expected to decrease.

3.7 Conclusions

In this Chapter, the catalytic activity of the $SnO_2(110)$ surface towards CO_2RR and HER has been analysed, providing a possible interpretation of experimental evidences. The calculations show an intrinsic catalytic inactivity of the electrode for the CO_2 conversion and H_2 evolution, but once the formation of a metallic Sn bilayer occurs, the electrocatalyst becomes selective for the HCOOH production. At working CO_2RR conditions, operando measurements [153, 154] observe both metallic Sn^0 and oxidized Sn^{II} species. Accordingly the discussed results, the experimental signal corresponding to the oxidized species comes from the subsurfaces layers, while the presence of an outermost thin zerovalent tin layer plays the key role in the catalytic reaction. However, the experimental in-situ detection of the Sn bi-layer may be difficult by means of standard techniques, while the ex-situ analysis may involve

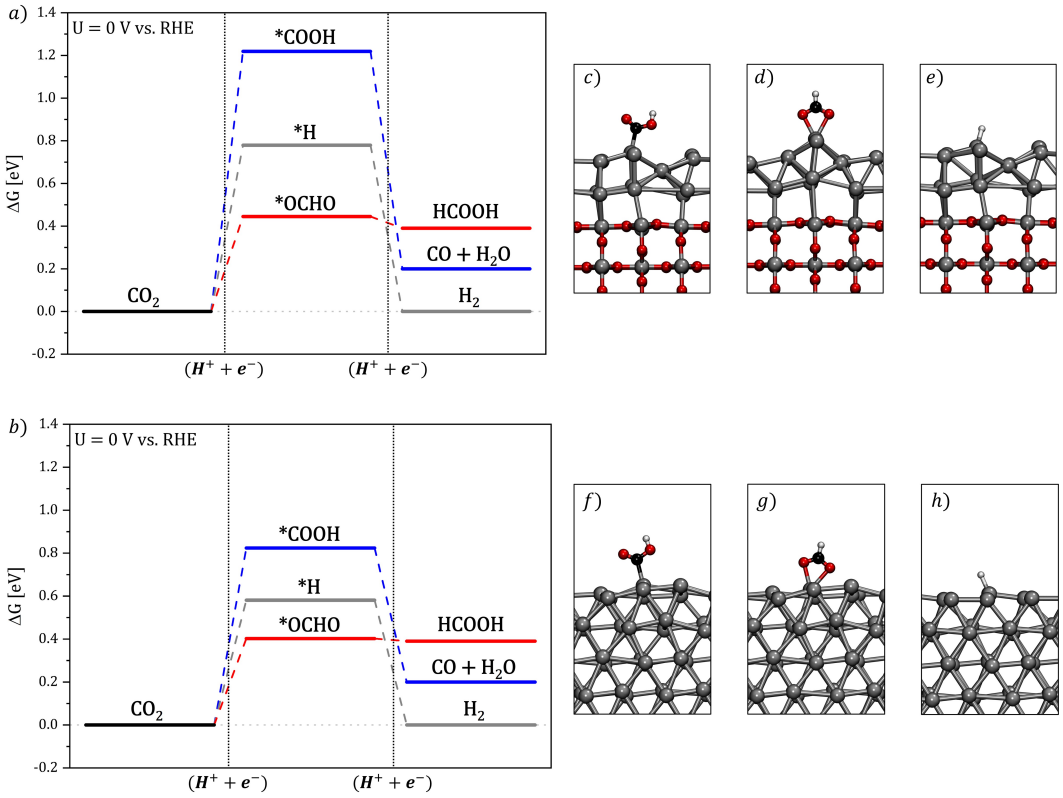


Figure 3.7 CO_2RR reaction paths to HCOOH and CO through *OCHO (red line) and *COOH (blue line) intermediates, respectively. HER reaction paths are also included (gray line). Panel a): 2Sn@SnO_2 surface at U = 0 V with respect to RHE. Optimized structures of adsorbates c) *COOH, d) *OCHO and e) *H at the 2Sn@SnO_2 surface. Panel b): Sn(101) surface at U = 0 V with respect to RHE. Optimized structures of adsorbates f) *COOH, g) *OCHO and h) *H at the Sn(101) surface. Figure adapted from Ref. [158].

the quick re-oxidation of the electrode, becoming undetectable. As soon as the application of a higher bias occurs, the SnO_2 surface is reduced to a metallic thick Sn layer. Even though the catalytic acitivity of the electrode persists, calculations show that the catalyst loses in selectivity, since the HCOOH and H_2 production become thermodynamically competitive.

CHAPTER 4

Imidazole-Imidazolate Pair in ZIF-8 for CO_2 Capture and Conversion

This Chapter provides a comprehensive study of the electrochemical properties of ZIF-8, an electro-organocatalyst that selectively captures and converts CO_2 to CO. The objective is to identify the active sites that enable this process, with a focus on the ZIF-8(110) surface as a model catalyst. To do so, we conducted thermodynamic analysis of the identified reaction mechanism, and computational details can be found in Appendix B, Section B.3.

The Chapter is organized as follows: Section 4.1 outlines the main objectives of this work. Section 4.2 discusses the structural properties of ZIF-8, including surface energy analysis and modifications such as changes in face terminations (110), while Section 4.3 presents the incorporation of carbon nanotubes (CNTs) to enhance electron transfer to the absorbed intermediate. Sections 4.4 and 4.5 propose thermodynamic reaction mechanisms for CO_2 reduction and discuss the electrochemical performance of pristine and CNT-supported compounds considering imidazole-imidazolate (ImH/Im^-) pair and undercoordinated Zn ions as active sites, respectively. Experimental results are presented in Section 4.6, which demonstrate the effectiveness of the electro-organocatalyst designed using the presented theoretical model. Finally, we summarize the main results in Section 4.7.

4.1 ZIF-8 electro-organocatalyst for CO_2 capture and conversion

This study aims to explore a novel electro-organocatalyst that has the potential to efficiently capture and reduce CO_2 by means of a theoretical approach. The catalyst is designed using a specific metal organic framework, composed of Zn ions and imidazolate ligands, which enables efficient CO_2 reduction to CO molecule.
Electro-organocatalysis is an effective strategy for the CO_2 conversion, involving the removal or addition of electrons through electrocatalysis, in combination with non-metal organic catalysts [160]. Both homogeneous and heterogeneous electro-organocatalysts for CO_2RR are reported in literature [161, 162]. The crucial aspect of this process is the electron transfer step, which can be facilitated through organic substrates to generate intermediates that subsequently undergo chemical processes such as bond dissociation and formation [163–165].
However, even though it is a widely accepted knowledge that metal sites are essential as catalytic sites for CO_2RR, the realization of an electro-organocatalytic system enables to convert the CO_2 without involving the metal centers is extremely fascinating and challenging in this research field. The pioneering work of Göttle and Koper [166] proposes a reaction mechanism for CO_2 reduction to HCOOH via the formation of a hydride donor phlorin ligand belonging to on porphyrin complexes. Here, the ligand behaves as nucleophilic species activating the CO_2 and the system does not imply the involvement of the metal center in the reaction mechanism.

One promising category of electrocatalysts is MOF [167], which features metal cations stabilized by organic ligands as reported in Section 1.3.2 of Chapter 1. The aforementioned arrangement includes highly porous surface area, versatile nature modifying the metal cation and its linkers, and tunable post-synthesis structure [168]. In this perspective, MOFs are an excellent candidate for CO_2RR, because they provide a broad opportunity in manifacturing diversified catalytic materials with several adavantages [169]: (i) guaranteeing high mass transfer and availability of active sites, (ii) managing the electronic structure by heteroatom doping techniques, (iii) preserving their pristine characteristics, such as surface area, porosity, and homogeneous active sites distribution. These features support the promising

electrocatalytic activity of MOFs for CO_2 conversion into value-added products [170].

In addition, previous research has shown that among the systems that effectively capture CO_2 are ionic liquids (IL), particularly those based on imidazolate, [171, 172]. Spectroscopic and theoretical investigations reveal that this is achieved via a CO_2-activated mechanism involving the formation of a carbonate intermediate where CO_2 interacts with the nitrogen atom of the nucleophilic imidazolate species [173, 174]. Despite these promising findings, the major limitations of such capturing systems are their high viscosity and significant energy consumption required for CO_2 desorption [175]. To enhance efficiency and reduce energy consumption, it is crucial to explore electrochemical imidazole-based system capable of simultaneous CO_2 capture and convertion.

Zeolitic Imidazole Frameworks (ZIFs) - a unique subclass of MOFs with a zeolite-like structure - have emerged as promising candidates for CO_2 conversion. Among the extensively studied ZIFs is ZIF-8, which contains zinc cations as metal centres coordinated with 2-methylimidazolate (Im^-) ligands, that exhibit exceptional CO_2 adsorption properties, a crucial step for the electrochemical CO_2RR [176]. Despite their widespread use in gas capture and separation [177, 178], here are only a limited number of publications on their use as electrocatalysts, especially in the selective reduction of CO_2 to CO [105, 179]. Furthermore, the characterization of the outermost catalytic sites is lacking. Chizallet et al. conducted experimental and DFT calculations to investigate the surface termination of the ZIF-8 system [180, 181]. They discovered that Lewis and Brønsted basic, as well as acid sites, such as N^- (Im^-) and NH (ImH) extremities of imidazolate ligands, respectively, are exposed at the surface along with the potential presence of hydroxyl (OH^-) and water (H_2O) species coordinated to Zn centers.
Therefore, the exposition of imidazole-imidazolate (ImH/Im^-) species suggests these terminations as potential catalytic sites acting similarly to the aforementioned imidazole-based ILs for CO_2 capture and following reduction. Previous investigations [106, 182] proposed a reaction mechanism for CO_2 reduction that occurs via the sp^2 carbon sites (C_{sp^2}) within the aromatic ring of Im^- ligand, neglecting the potential contribution of the nitrogen atom of the imidazole ring previously discussed. The involvement of C_{sp^2} species leads to the aromaticity loss, which is an extremely

energetic step (about 2 eV), as Jiang et al. calculated in their computational work [106]. High energy barriers were also obtained by Dou and coworkers [182], who investigated the effect of ligand doping on CO_2 reduction employing a streamlined cluster as model structure of the actual complex system.
These findings show that the role of nitrogen atoms belonging to the imidazole ring for CO_2 reduction have been underestimated in earlier studies.

Therefore, taking in consideration the peculiar surface organization, in the following sections the theoretical investigation of CO_2 capture and conversion on ZIF-8 electro-organocatalyst is discussed.

4.2 Investigation of ZIF-8(110) surface terminations

The ZIF-8 compound is an ordered and robust material composed of imidazole-based units in which Zn^{2+} cations are tetra-coordinated with imidazolate anions Im^-, forming a periodic and crystalline structure as shown in Figure 4.1*a*. To study the properties of the ZIF-8 material as an electro-organocatalyst, a suitable facet was constructed based on its crystal bulk structure. In particular, among all the possible facets, the low-index ZIF-8 (110), reported in Figure 4.1*b*, was investigated. The focus on this surface is due to its prevalence in rhombic dodecahedron crystals observed in characterization data [183–186]. To generate the ZIF$-$8(110) surface, the weak Zn-Im coordination bonds were cleaved, while the ImH/Im^- pair of the bottom layer of the slab were kept fixed at their bulk positions.

ZIFs are typically synthesized in aqueous solvents at room temperature, which may impact the surface structure and termination of the resulting material. To identify the catalytic site for CO_2RR, it was necessary to determine the precise termination of the ZIF-8(110) surface. The most thermodynamically stable surface termination is one that minimizes the surface free energy, ($\gamma(T,p)$), which can be calculated as follows:

$$\gamma(T,p) = \frac{1}{2A}(G_{slab}(T,p,N_i) - \sum N_i \mu_i(T,p)) \tag{4.1}$$

where G_{slab} is the Gibbs surface free energy of a slab with surface area A, N_i is the number of the outermost species with chemical potential μ_i at temperature T and pressure p.

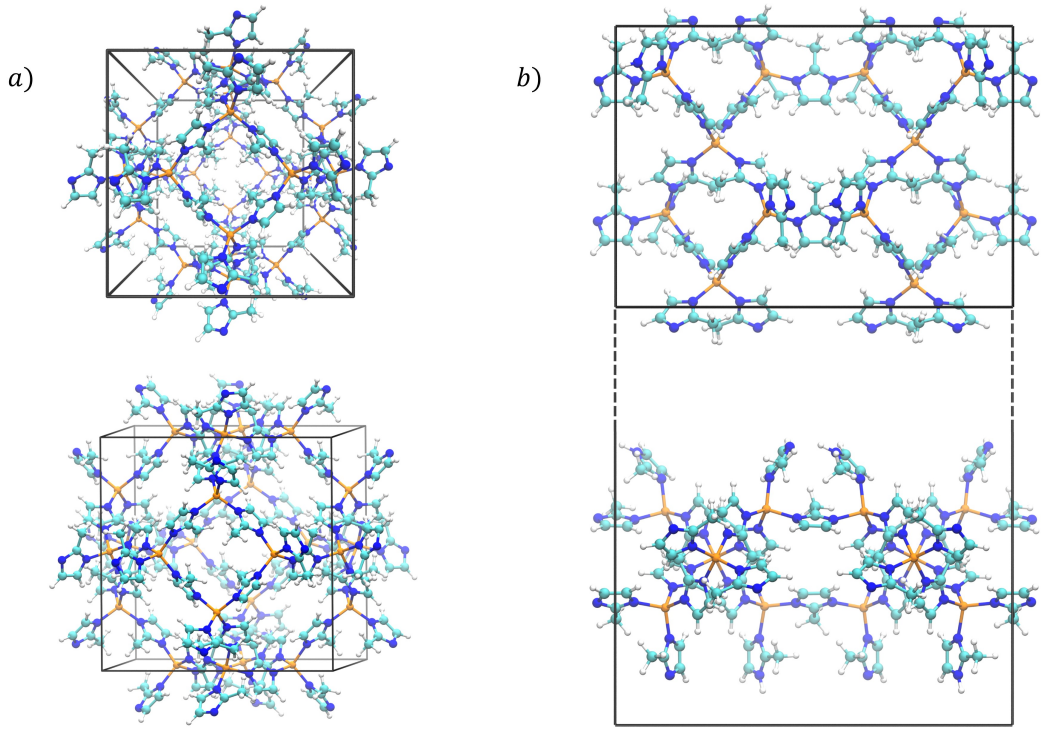


Figure 4.1 Ball-and-stick representations of simulated ZIF-8 bulk (a) and (110) surface (b). Atom color code: orange for zinc, blue for nitrogen, white for hydrogen, and cyan for carbon atoms in the ZIF structures.

We analyzed the relative thermodynamic stability of various terminations of ZIF-8 in aqueous solution at room temperature, starting from Eq. 4.1. We constructed surface models of ZIF-8 exposing different possible charge-neutral terminations with full coverage to compensate for the Zn cations. The outermost terminations are labeled as $surf_{n/m}$ based on the number of organic linkers (n), including ImH and Im^-, and adsorbed solvent molecules (m), such as H_2O and OH^-. Using this labeling system, we differentiated the ZIF-8(110) surfaces into three categories: (i) Enrich organic ligands slabs - $surf_{4/0}$ and $surf_{3/1}$ - which exposed two ImH/Im^- pairs and one ImH/Im^- and one ImH/OH^- pair, respectively. (ii) Stoichiometric organic/aqueous terminations - $surf_{2/2}$ - which presented ImH/Im^- and H_2O/OH^- couples. (iii) Enriched solvent surfaces - $surf_{0/4}$ and $surf_{1/3}$ - which displayed H_2O/OH^- species and one H_2O/OH^- and one ImH/OH^- pair, respectively. The analysis of the relative thermodynamic stability of these terminations based on their respective surface free energies was performed.

Figure 4.2 shows the phase diagram reporting γ as a function of the ImH chemical potential ($\Delta\mu_{ImH}$). A detailed discussion of phase diagram construction is reported in Section A.4 of Appendix B.

The appropriate concentration of ImH is crucial under synthesis conditions. At high $\Delta\mu_{ImH}$, the $surf_{4/0}$ termination (Figure 4.2*g*) becomes the most stable surface, completely covered by imidazole/imidazolate. This configuration is stabilized by the formation of a hydrogen bond between the hydrogen atom in ImH and a nitrogen atom in the neighboring Im^- . Conversely, at low $\Delta\mu_{ImH}$, the $surf_{0/4}$ surface (Figure 4.2*h*) becomes the predominant termination, exposing H_2O/OH^- groups. Given that CO_2RR experiments are typically conducted under neutral or slightly acidic conditions, investigating imidazole/imidazolate-terminated ZIF-8(110) surfaces is plausible, as their thermodynamic stability has been demonstrated under these working conditions[187].

4.3 Designing carbon nanotube supported ZIF-8 electrocatalyst

ZIF-8's limited electrical conductivity has hindered its practical application as electrocatalyst. However, the high microporosity of ZIFs enables the inclusion of

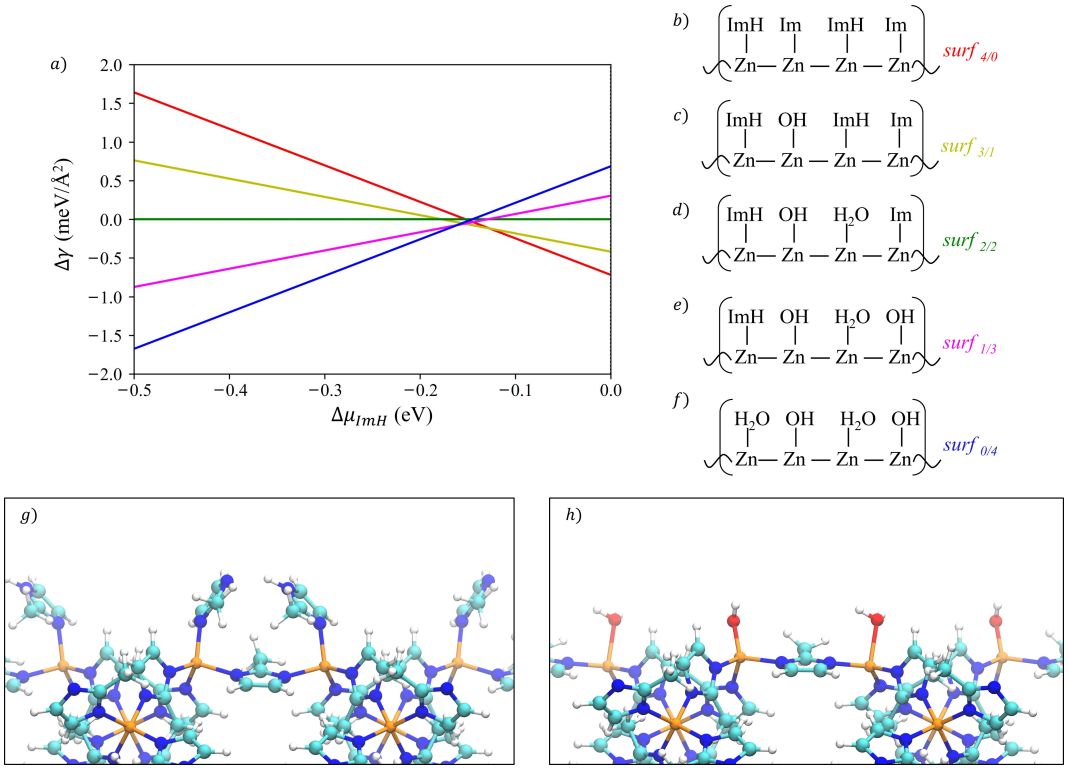


Figure 4.2 ZIF-8 (110) surface phase diagram (a). Surface structures schematically depicted: b) $\text{surf}_{4/0}$ (red line), c) $\text{surf}_{3/1}$ (ocher line), d) $\text{surf}_{2/2}$ (green line), e) $\text{surf}_{1/3}$ (fuchsia line), and f) $\text{surf}_{0/4}$ (blue line). Panels g) and h) are the surface terminations of $\text{surf}_{4/0}$ and $\text{surf}_{0/4}$, respectively. Atom color code: orange for zinc, blue for nitrogen, white for hydrogen, red for oxygen and cyan for carbon.

guest composites, which has led to the development of more conductive ZIF-8 materials[188, 189]. Indeed, recent research has explored ways to enhance the conductivity of ZIF-8-based materials by incorporating various conductive supports [190, 191].

To investigate the potential for CO_2 reduction, we simulated the deposition of ZIF-8 on a conductive nanostructure, specifically a CNT. Not only does this material exhibit metallic properties when grown with a specific chirality [192], but it also demonstrates good chemical and electrochemical catalytic abilities [193]. Thus, incorporating it could significantly enhance the reactivity of ZIF-8. In addition, the use of a carbon-based material like CNTs offers several advantages, such as reducing the need for expensive inorganic materials and introducing a more hydrophobic environment [168]. This is expected to achieve both improved CO_2 reduction and stronger adherence of the catalyst to the electrode during electrolysis. To further

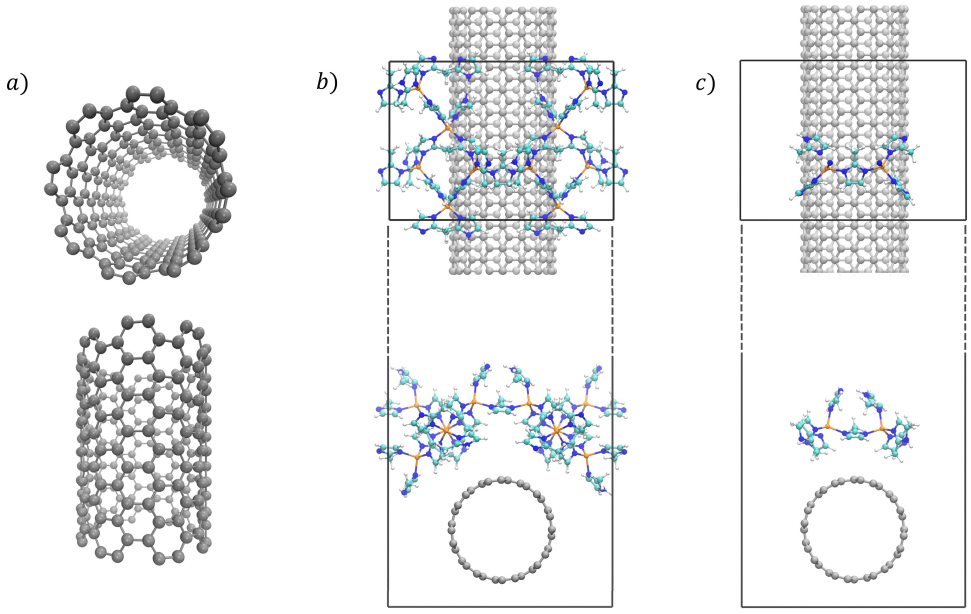


Figure 4.3 Ball-and-stick representations of simulated CNT incorporated ZIF-8 structures: a) CNT 8x8, b) ZC1@CNT and, c) ZC2@CNT. Atom color code: orange for zinc, blue for nitrogen, white for hydrogen, cyan and dark gray for carbon atoms in the ZIF structures, and CNT, respectively.

investigate the effects of size on the electrocatalytic performance of ZIF-8, a metallic (8x8) CNT was used as a model and interfaced with the catalyst (Figure 4.3*a*). This

resulted in two clusters of different sizes, named ZC1@CNT and ZC2@CNT. The ZC2@CNT cluster was the smaller of the two and exposed only one ImH/Im$^-$ pair (Figure 4.3*c*) while the ZC1@CNT cluster still showed the two outermost native ImH/Im$^-$ couples (Figure 4.3*b*). To simulate the composite ZIF-CNT system, both clusters underwent structural optimization, resulting in a configuration where the ImH/Im$^-$ species at the bottom reorganized themselves to wrap around the carbon nanotube in a cohesive manner. Moreover, the downsizing of ZIF-8 clusters led to a more intimate contact between the active site and the CNT surface.

In Section 4.3, we will investigate and compare the electrocatalytic performance of these composites for CO_2 reduction against that of the unmodified ZIF-8(110) surface, providing valuable insights into the effects of introducing CNT support and varying material sizes on their electrocatalytic properties

4.4 Elctrochemical CO_2RR on ImH/Im$^-$ sites

The analysis presented in Section 4.2 indicates that, during reduction conditions, the ZIF-8(110) surface with a $surf_{4/0}$ termination is the most stable. This surface exposes two ImH/Im$^-$ pairs, which are stabilized by hydrogen bonds, as shown in Figure 4.2*g*.
We have proposed a CO_2 reduction mechanism leading to the formation of CO and H_2O molecules, building upon previous research conducted by Lee et al. [194]. Their investigations into a CO_2RR reaction pathway mechanism involving a carbamate bonded to monoethanolamine provided a foundation for this work. Additionally, recent research suggests that imidazolate species can form covalent bonds with CO_2 [173, 174], allowing for CO_2 adsorption on these surfaces. With this knowledge in mind, the proposed CO_2 reduction mechanism can be described as follows:

$$CO_2 + 2\,(H^+ + e^-) \longrightarrow CO + H_2O \tag{4.2}$$

which unfolds into three steps according to the mechanism here proposed:

$$^*Im\cdots H{-}Im^* + CO_2 \longrightarrow {}^*Im{-}COO\cdots H{-}Im^* \tag{4.2.a}$$

$$^*Im{-}COO\cdots H{-}Im^* + (H^+ + e^-) \longrightarrow {}^*Im{-}COOH\cdots H{-}Im^* \tag{4.2.b}$$

$$^{*}\mathrm{Im}-\mathrm{COOH}\cdots\mathrm{H}-\mathrm{Im}^{*}+(\mathrm{H}^{+}+\mathrm{e}^{-})\longrightarrow{}^{*}\mathrm{Im}\cdots\mathrm{H}-\mathrm{Im}^{*}+\mathrm{CO}+\mathrm{H_2O} \quad (4.2.c)$$

where the active site is the $^{*}\mathrm{Im}\cdots\mathrm{H}-\mathrm{Im}^{*}$ system and $*$ represents the ZIF-8 surface. Initially, the reaction proceeds through chemical adsorption of CO_2 (Eq. 4.2.a) forming a Lewis adduct ($^{*}\mathrm{Im}-\mathrm{COO}$) where the nitrogen atom from the imidazolate ring serves as the Lewis base and CO_2 as the Lewis acid. The electrochemical reduction reaction then proceeds through two proton-electron transfer steps (Eq. 4.2.b and 4.2.c). In the final stage, the reaction yields the final products (CO and H_2O), which are released into the electrolyte, thereby reactivating the catalytic surface ($^{*}\mathrm{Im}\cdots\mathrm{H}-\mathrm{Im}^{*}$).

The thermodynamic Gibbs free energy profiles for electrochemical CO_2 conversion to CO and H_2O were calculated using the approach described in Section 2.5.2 of Chapter 2. The calculations were based on the aforementioned mechanism that considers imidazole/imidazolate as catalytic sites. The Gibbs free energy calculations were performed at zero potential (U = 0 V) with respect to RHE.

Figure 4.4 illustrates the free energy profiles of the following systems: the CO_2RR on the pristine ZIF-8(110) surface, denoted as ZIF-8, while the CO_2 reduction steps on the ZIF-8 clusters, namely ZC1@CNT and ZC2@CNT, are denoted by red and green, respectively. The first chemical reaction step, which involves the formation of $^{*}\mathrm{Im}-\mathrm{COO}$ adduct via nucleophilic addition of imidazolate nitrogen to CO_2 (Eq. 4.2.a), is spontaneous in all three pathways of the free energy diagram since $\Delta G_{\mathrm{CO_2}\rightarrow{}^{*}\mathrm{COO}} < 0$ eV. CO_2 activation or subsequent reduction takes place after the formation of the $^{*}\mathrm{Im}-\mathrm{COO}$ adduct, where a C–N bond that is 1.57 Å long is formed, resulting in the bending of the CO_2 molecule with an $\widehat{OCO}$ of 134.4° degrees. Finally, the final Lewis adduct is stabilized by a hydrogen bond between the $^{*}\mathrm{Im}-\mathrm{COO}$ group and the nearby $\mathrm{H}-\mathrm{Im}^{*}$ ligand.
While the activation of CO_2 offers significant energy advantages due to its spontaneous reaction, electrochemical reduction requires high-energy electrochemical steps. At a voltage of U = 0 V vs RHE, all three reaction pathways exhibit a similar energy trend where the overall reaction is non-spontaneous and necessitates a negative U_{onset} to proceed. Specifically, the first proton-electron transfer leading to the half-reduced CO_2 intermediate (*COOH) involves an uphill electrochemical reduction step ($\Delta G_{{}^{*}\mathrm{COO}\rightarrow{}^{*}\mathrm{COOH}}$), which ultimately determines the U_{onset} for all investigated ZIF-8 models.

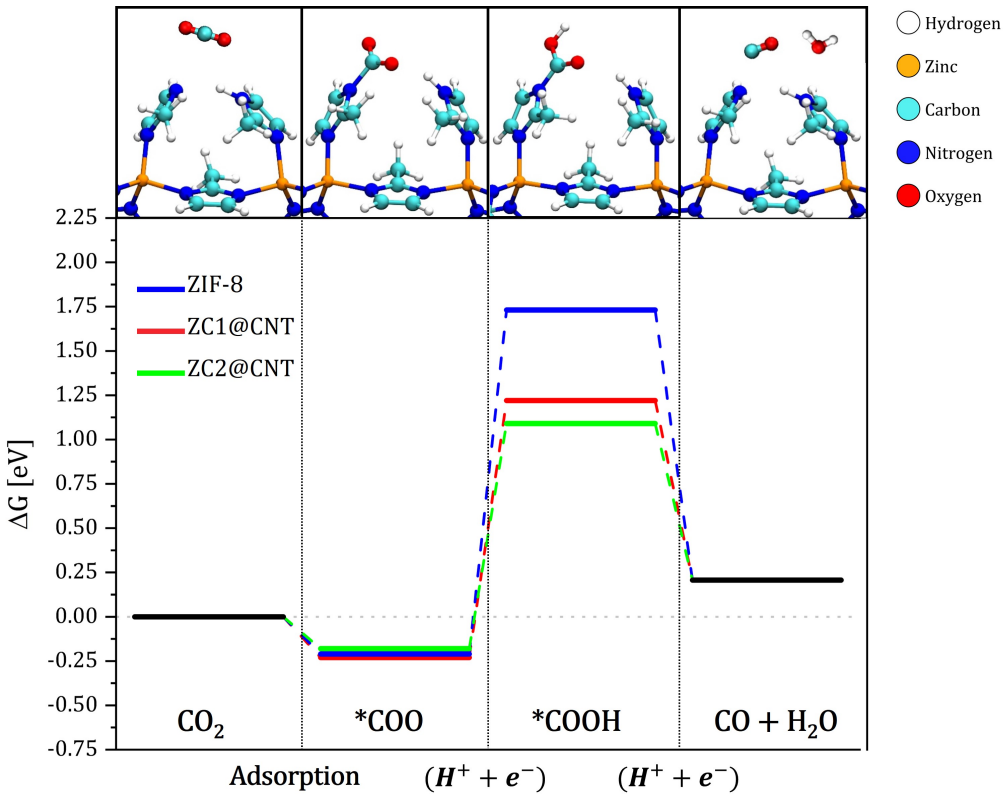


Figure 4.4 Lower panel: CO_2RR pathway forming CO and H_2O on ZIF-8 (blue line), ZC1@CNT (red line) and ZC2@CNT (green line) at U = 0 V vs RHE. Upper panel: Ball-and-stick representation of reaction states. Atom color code: orange for zinc, blue for nitrogen, white for hydrogen, red for oxygen and cyan for carbon. Figure taken from Ref [195].

The conversion of *COO to *COOH on the ZIF-8 surface requires significantly more energy ($\Delta G^{ZIF-8}_{^*\mathrm{COO}\rightarrow{}^*\mathrm{COOH}}$ = 1.95 eV) than on the CNT-supported ZIF-8 compound ZC1@CNT ($\Delta G^{ZC1@CNT}_{^*\mathrm{COO}\rightarrow{}^*\mathrm{COOH}}$ = 1.45 eV). This finding underscores how a conductive support function, such as a carbon nanotube, can promote the first reduction step, facilitating the formation of the *COOH intermediate and decreasing the energy barrier by roughly 0.5 eV. Furthermore, as the size of the cluster in contact with the CNT decreases, the $\Delta G_{^*\mathrm{COO}\rightarrow{}^*\mathrm{COOH}}$ is further reduced. As a result, the first proton-electron transfer on the ZC2@CNT system requires even less energy ($\Delta G^{ZC2@CNT}_{^*\mathrm{COO}\rightarrow{}^*\mathrm{COOH}}$ = 1.27 eV). These findings suggest that a smaller ZIF-8 structure in closer proximity to the CNT surface can enhance the overall catalytic performance of the ZIF-8/CNT system.

4.5 CO_2RR and HER on undercoordinated Zn metal center

Despite the more stable surface exposing ImH/Im^- ligands, under experimental conditions it is possible for ZIF-8 surfaces to contain undercoordinated defective Zn sites in aqueous media [180, 181], as previously discussed in Section 4.2. These sites may react with water, resulting in H_2O/OH^- terminations. Specifically, the charge-neutral surface ZIF-8 (110) surface terminated by hydroxyls and water ligands coordinated to Zn atoms was considered as reported in Figure 4.2*h*.

At these particular sites, multiple reactions can compete with one another, such as the conversion of CO_2 to HCOOH via the *OCHO intermediate, or alternatively, the conversion to CO through the *COOH intermediate. In addition, HER can occur, which proceeds via *H intermediate. For more details about the reaction mechanisms, see Eq. (1.1.a) and (1.2.a) for the formation of *OCHO and *COOH intermediates, respectively, presented in Section 1.2.2 of Chapter 1. The Gibbs free energy profiles of all three reaction pathways have been investigated, and they require two successive proton-electron transfers to occur. The outermost Zn atoms may have coordinative vacancies, which can be formed where a ligand is missing and may directly participate in reduction processes. From a coordination chemistry perspective, water molecules behave as weak ligands, and the reaction that occurs is

generally as follows:

$$^{*}H_2O + (M) \longrightarrow {}^{*}M + H_2O \tag{4.3}$$

Therefore, $^{*}H_2O$ can be easily replaced by incoming species (M) due to the weak bonding interaction between water molecules and metal centers. However, the bonding interaction between metal centers and hydroxyl anions is strong, and in order to activate the active site, protonation is necessary to convert them to $^{*}H_2O$ adsorbates, as follows:

$$^{*}OH + (H^{+} + e^{-}) \longrightarrow {}^{*}H_2O \tag{4.4}$$

whose calculated Gibbs free energy ($\Delta G_{^{*}OH \rightarrow {}^{*}H_2O}$) is 1.50 eV. The catalytic pathway involving water decoordination (Eq. 4.4) have been considered to convert CO_2 in C1- products (HCOOH and CO), as well as to evolve H_2 on undercoordinated Zn atom. Figure 4.5 shows the free energy profiles of the three reactions at U = 0 V vs RHE. From a thermodynamic perspective, the first PET that produces the half-reduced adsorbed intermediate is uphill and determines the U_{onset} of the reaction for all three reduction pathways. The formate production pathway that passes through the $^{*}OCHO$ intermediate requires the lowest bias, which is about -1.0 V relative to $^{*}COOH$ and $^{*}H$ (-1.80 V and -1.96 V, respectively), predicting that ZIF-8 (110) surface terminated by H_2O/OH^{-} molecules is selective towards HCOOH.

To validate the accuracy of these theoretical predictions, our colleagues from the Istituto Italiano di Tecnologia synthesized the ZIF-8 electro-organocatalyst and conducted a series of electrochemical investigations. These investigations aimed to analyze the electrochemical performance of ZIF-8 both in its pristine state and when grown on metallic multi-walled carbon nanotubes (MWCNTs). The findings of these experiments are presented in Ref. [195] and are summarized in the next section.

4.6 Synthesis and electrochemical performace of ZIF-8 electro-organcatalyst guided by DFT predictions

The theoretical results presented have been employed as guidelines for the synthesis of ZIF-8 based electro-organocatalysts for CO_2RR [195]. New synthesis

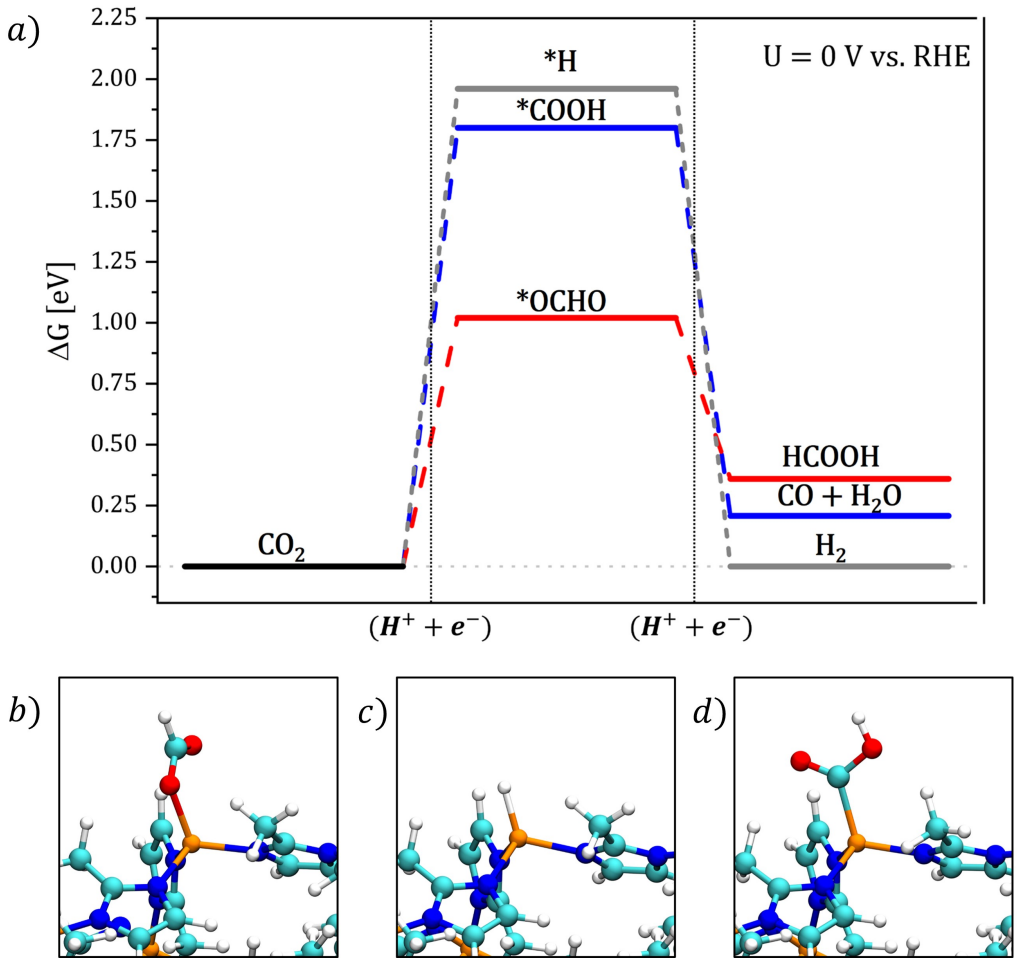


Figure 4.5 CO_2RR and HER on ZIF-8 (110) surface terminated by hydroxyls and water species. Panel a) displays the free-energy profiles for HCOOH (red line), H_2 (grey line) and CO (blue line) at U = 0 V vs RHE. Panels b), c) and d) represent *OCHO, *H and *COOH intermediates, respectively. Atom color code: orange for zinc, blue for nitrogen, white for hydrogen, red for oxygen and cyan for carbon. Figure taken from Ref [195].

method used to create ZIF-8 framework (sZIF-8) and ZIF-8 grown on MWCNTs (sZIF-8-MWCNT) in water solution. Procedure included mixing solutions of 2-methylimidazole and sodium hydroxide, adding [$Zn(NO_3)_2 \cdot 6H_2O$] solution dropwise under sonication, and separating and washing the powder. MWCNTs were added for sZIF-8-MWCNT synthesis. Bare MWCNTs were also sonicated in basic media for comparison. Zn salt was excluded to avoid contamination.

Morphological and spectroscopic analyses were performed on sZIF-8 and sZIF-8-MWCNT samples, revealing significant differences. The incorporation of MWCNTs leads to drastic changes in particle size and morphology, causing material amorphization. ATR spectra show similar patterns for both materials, demonstrating the formation of ZIF in presence of MWCNT. XRD patterns reveal that sZIF-8 is highly crystalline, while sZIF-8-MWCNT shows a mixture of crystalline and amorphous regions due to the presence of nanotubes. Loss of crystallinity is an improvement for electrocatalysis, exposing more defective sites bearing undercoordinated Im-site (See FE-SEM analysis reported in Figure 4.6).

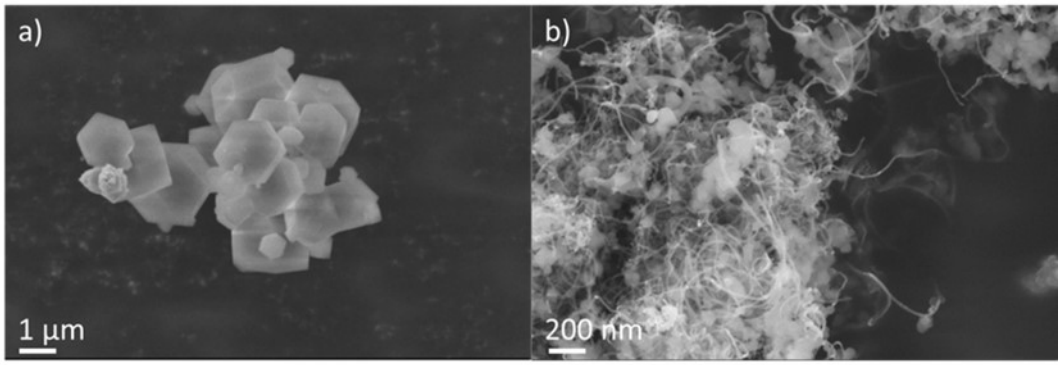


Figure 4.6 Electron microscopic images: a) FE-SEM images of sZIF-8 and b) sZIF-8-MWCNT. Figure taken from Ref [195].

The addition of MWCNT to ZIF-8 affects its morphology, crystallinity, and porosity, but not its thermal stability. The XPS analysis in Figure 4.7 shows the hybrid material preserves the coordination geometry of ZIF-8. The nitrogen signal in sZIF-8-WCNT indicates the presence of defects in crystals as undercoordinated imidazoles, supporting the mechanism involving the imidazole-imidazolate pair. The Zn signals cannot discriminate between ZnO and $Zn(OH)_2$ species, but the O signal helps to discriminate the absence of ZnO nanoparticles in the catalyst.

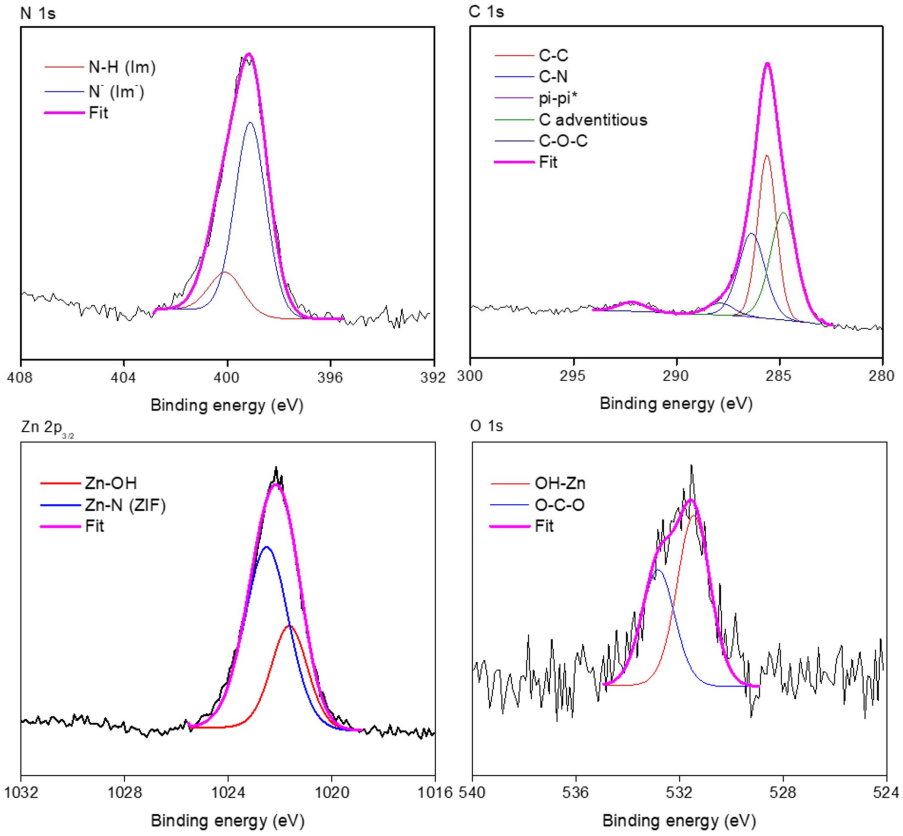


Figure 4.7 XPS measurements for sZIF-8-WCNT-8 sample. Top-left, N 1s, top-right, C 1s, bottom-left, Zn $2p_{3/2}$ and bottom-right, O 1s regions. Figure adapted from Ref [195].

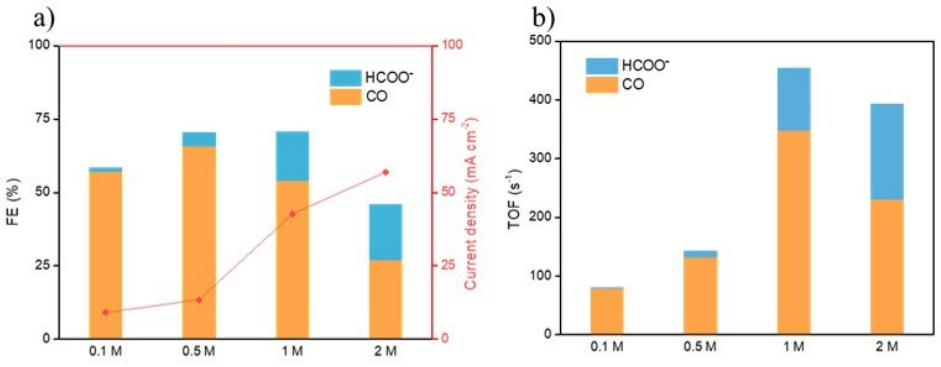


Figure 4.8 Semi-flow cell CO_2RR investigation on sZIF-8-MWCNT electrodes: a) FEs and current densities at -1.2 V in different electrolyte compositions and b) the relative TOFs. Stability test in 0.1 M $KHCO_3$ at -1.2 V vs RHE. Figure adapted from Ref [195].

Initially, chronoamperometric tests were conducted to evaluate the electrocatalytic performance of sZIF-8 and sZIF-8-MWCNT electrodes in a 0.1 M $KHCO_3$ solution at -1.2 V vs RHE using a batch cell configuration. The best selectivity for the CO_2RR was achieved with sZIF-8-MWCNT catalyst, reaching a FE_{CO_2RR} of 65.7% compared to 48.7% for sZIF-8. The lower current density of sZIF-8 is attributed to its low electrical conductivity and stability.

To further investigate the sZIF-8-MWCNT catalyst, different concentrations of $KHCO_3$ water solution (0.1, 0.5, 1.0, and 2.0 M) were combined with it and the resulting performance was tested at -1.2 V vs RHE in a flow cell configuration. The results, as shown in Figure 4.8*a*, reveal that 0.5 M is the optimal concentration for CO production, achieving a FE_{CO} of 65.8% and an overall FE_{CO_2RR} of 70.4%.

Interestingly, the turnover frequency (TOF_{CO_2RR}) Figure 4.8*b* is higher with more concentrated electrolytes, due to the higher currents obtained. In addition, the production of $HCOO^-$ was observed to be directly proportional to the concentration of $KHCO_3$ in the electrolyte. This can be explained by the DFT calculations that predicted the $HCOO^-$ production in the presence of surface Zn sites coordinating the H_2O/OH^- species. The higher dielectric constant of the electrolyte with more dissolved salt can make the dissociation of the coordinated water molecules easier, resulting in better shielding of zinc charge.

The experimental data gathered demonstrate that ZIF-8 is selective towards CO production. Additionally, the catalytic performance of ZIF-8-MWCNT shows a significant improvement in CO_2RR compared to the pristine ZIF-8 sample, as evidenced by higher activity and selectivity. These findings are consistent with the onset potential that was theoretically predicted and demonstrate the potential for ZIF-8-based materials to be used as efficient catalysts for CO_2 reduction.

4.7 Conclusions

This Chapter employed DFT calculations to propose feasible reaction mechanisms that may occur on the two distinct types of active sites presented in the ZIF-8 electro-organocatalyst. These active sites were investigated through thermodynamic analysis, leading to important insights into the catalytic properties of ZIF-8.

It was discovered that the ZIF-8(110) surface with imidazole-based termination is highly selective for the conversion of CO_2 to CO. On the other hand, the compound favors formate production when undercoordinated zinc centers are exposed.

Moreover, incorporating a conductive support such as CNTs is predicted to enhance electron transport in the catalyst. Representative models (ZC1@CNT and ZC2@CNT clusters) of ZIF-8/CNT systems with varying sizes were simulated, and it was found that the efficiency towards CO production increases as the catalyst size decreases, which enhances catalyst/support contact. This theory-guided catalyst design was then validated through experimental data, providing an interesting method for guiding the synthesis of heterogeneous catalysts.

The findings of this study had important implications for the development of novel catalysts for CO_2 reduction. By gaining a deeper understanding of the active sites and reaction mechanisms involved, it was possible to design more efficient and selective catalysts.
The generalization of this approach to design new electrocatalysts could ultimately lead to the development of more sustainable and environmentally friendly processes for CO_2 reduction, with significant benefits for the environment and society as a whole.

CHAPTER 5

Voltage-Dependent Activation Energy of CO_2RR on Ag and Zn Surfaces

The goal of this study is to gain a better understanding of CO_2RR on silver and zinc metal electrodes by means of a kinetic investigation. The employed approach involves the identification of reaction transition states upon the application of a constant potential and the estimation of the activation energiy.
The kinetic barriers of CO_2RR via the Tafel- and the Heyrovsky-like reduction mechanisms were computed and compared to the competing HER. The computational details are provided in Appendix B, Section B.4.

The Chapter is organized as follows: a short overview of the experimental and theoretical studies using Ag and Zn electrodes is presented in Sections 5.1 and 5.2, followed by a thermodynamic analysis in Section 5.3. Sections 5.4 and 5.5 discuss the reaction mechanisms of CO_2RR and HER and the results of calculation of the voltage-dependent activation energy. Finally, concluding remarks are in Section 5.6.

5.1 CO_2RR and the binding energy of CO on Ag and Zn surfaces

Transition metal electrocatalysts have been widely investigated for electrochemical CO_2 reduction [196]. This class is one of the most explored due to the ease and versa-

tility in design and development of electrocatalysts, as well as the high selectivity of transition metals towards specific products, as reported in Section 1.3.1. Pioneering research of Hori [66, 197] categorized pure elemental metals into three major groups based on their products: CO, formate or hydrocarbons. In particular, CO production has been broadly investigated due to its commercial interest in chemical industry and Fischer-Tropsch synthesis. Although Au exhibits the highest activity towards CO production at low overpotential, it is an expensive metal. Ag and Zn have emerged as potentially efficient and relatively cheaper electrocatalysts with high selectivity in CO_2-saturated electrolytes for CO production [35].

Based on the Sabatier principle that an ideal catalyst should moderately bind the reaction intermediates, several reports found that a key descriptor of the product distribution is the binding strength of CO on the metal surfaces. In the work by Kuhl et al. [198], a volcano plot of the CO adsorption strength related to the electrochemical CO_2 conversion current density was derived for different transition metals. Au appears close to the top of the volcano, as the ideal metal to bind CO, while Ag and Zn give weaker binding energies and are located on the low-binding-energy side of the volcano. These insights allowed to interpret the current efficiency trend for CO_2RR on Ag and Zn foils. Indeed, because of the slow CO_2 activation on these metals, HER dominates at low overpotential, but it is suppressed as overpotential increases, leading to the CO_2 conversion to CO weakly bound to the surface, which favors its desorption. Operando Raman and infrared spectroscopies show that CO species adsorbed on the electrode surface during CO_2 reduction prevent hydrogen adsorption, leading to HER suppression [199–202]. Finally, at high overpotential a mass transfer control occurs and CO_2 barely reaches the electrode surface and selectivity shifts back to hydrogen. The maximum selectivity of CO_2RR to CO on Ag and Zn foils is experimentally detected in the range from -1.0 to -1.2 V vs. RHE, limiting practical applications [203, 204]. Consequently, the synthesis and characterization of Ag and Zn catalysts have been extensively explored, both from the theoretical and the experimental points of view, in terms of morphology, size and porosity to improve CO_2RR efficiency.

5.2 Previous work on CO_2RR on Ag and Zn electrocatalysts

Much effort has been devoted to the design of selective and active Ag and Zn metal electrodes for CO_2 conversion to CO. The morphology of the exposed metal surfaces has been proven to play a key role in CO_2 reactivity.

Early research by Hori et al. [205] on single-crystal silver, showed that the Ag(110) facet has a higher catalytic activity for the electrochemical CO_2 conversion to CO than Ag(111) and Ag(100). Later computational studies related the high density of step and edge sites on Ag surface to the increased stabilisation of CO_2 intermediates and, consequently, to improved CO_2 reduction [206]. In particular, DFT simulations showed that Ag(110) and Ag(211) facets have a lower free energy barrier for transferring the first proton-electron pair to CO_2 than flat surfaces such as Ag(111) and Ag(100) [206]. Recent experimental work aimed at investigating the facet-dependence of the CO evolution activity on large area Ag thin film electrodes [207]. Consistent with the aforementioned single-crystal studies, at -1.0 V vs RHE, Ag(110) thin films were found to have a superior intrinsic activity with respect to Ag(111) or Ag(100) facets because of a higher density of undercoordinated active sites.

The morphology of Zn-based catalysts for CO_2RR to CO has also been investigated. Won et al. [208] compared a hierarchical hexagonal Zn (h-Zn) electrode to conventional Zn foil. The h-Zn catalyst exhibited the highest CO production at -1.1 V vs RHE, suggesting a correlation with the (101) surface, which is preferentially exposed by h-Zn. DFT calculations confirmed that Zn(101) favors CO production while the (002) facet promotes H_2 evolution. This finding was further supported by varying the crystal facet ratios in different Zn catalysts [209], confirming that the Zn(101) surface promotes CO_2 reduction to CO. In another study, the role of crystal planes on metallic hexagonal Zn nanoplates (H-Zn-NPs) was investigated both experimentally and theoretically by Luo et al. [210]. The authors synthesized H-Zn-NPs enclosed by (002) and (100) facets and found that the CO_2RR catalytic activity for CO production on Zn catalysts can be enhanced by maximizing the percentages of Zn(100) facets and edge sites.

A purely thermodynamic approach may not always be sufficient to predict the selectivity of an electrocatalyst towards a reaction product. In recent work [211], using the CHE model, the authors performed a computational investigation on different metal surfaces to calculate the theoretical onset potentials for the CO_2 electroreduction to HCOOH, CO and H_2. In the case of Ag and Zn, the obtained U_{onset} led to a misclassification of these metals, since they were predicted to produce formate and H_2, at odds with the experimental results that show a high selectivity toward CO. The authors suggested that the CO_2 conversion to HCOOH may be kinetically hindered compared to the CO production. Similarly, from thermodynamic DFT calculations, copper is expected to mainly produce HCOOH [212], even though its onset potential is experimentally found to be similar to that of CO formation (about -0.5 V vs RHE) [66]. This discrepancy between the thermodynamic calculation and experimental observations was resolved by DFT calculations of voltage dependent activation energy which showed that similar values were found for the two competing reaction mechanisms for the formation of CO and $HCOO^-$ [213].

These findings underline that only a full kinetic analysis can correctly explain the observed selectivities of Ag and Zn electrocatalysts and reveal the actual reaction mechanisms taking place on the metal surface.

5.3 Thermodynamic investigation of CO_2RR on Ag and Zn low-index surfaces

To investigate the inconsistencies between the experimental selectivity towards CO of Ag and Zn and the theoretical calculations based on the CHE that predict the production of HCOOH and H_2 on these metals, we performed first a thermodynamic study of CO_2RR to HCOOH and CO, and of the competing HER on low-index surfaces of silver and zinc.

In the case of silver, the three crystal surfaces (111), (100) and (110) were considered to model polycrystalline silver foils. Ag(111) is the most densely packed, flat surface, whereas the surface coordination decreases as Ag(111)>Ag(100)> Ag(110). Regarding zinc, we studied the close-packed Zn(0001) surface and the undercoordinated Zn($10\bar{1}0$) facets, where the outermost Zn atoms form chains. Figure 5.1 show

the investigated low-index surfaces of silver and zinc. To perform the thermodynamic investigation, we considered two possible first reaction steps of CO_2RR

$$CO_2 + (H^+ + e^-) \xrightarrow{\Delta G_{CO_2 \rightarrow {}^*OCHO}} {}^*OCHO, \tag{5.1}$$

or

$$CO_2 + (H^+ + e^-) \xrightarrow{\Delta G_{CO_2 \rightarrow {}^*COOH}} {}^*COOH, \tag{5.2}$$

where CO_2 is converted to HCOOH or CO through the *OCHO and *COOH intermediates, respectively. HER occurs as follows

$${}^*(H^+ + e^-) \xrightarrow{\Delta G_{H^+ \rightarrow {}^*H}} {}^*H. \tag{5.3}$$

in which an H^+ coming from the electrolyte is reduced by an electron from the electrode and adsorbed on the surface as *H.

By taking a pure thermodynamic approach, it is possible to identify the most stable intermediates and make assumptions about the selectivity and activity of the electrocatalysts. The CHE model has been employed to calculate the adsorption Gibbs free energy (ΔG) at zero applied potential ($U = 0$ V) referred to the RHE of the first proton-electron transfer (PET) step (Chapter 2, section 2.5.2). In Figure 5.1, the plot shows the ΔGs calculated for the low-index metal surfaces. From Figure 5.1, we can notice that the formation of *COOH intermediates is, generally, thermodynamically less favored than *OCHO species for all silver and zinc surfaces. Specifically, the Gibbs free energy needed to transfer a ($H^+ + e^-$) pair to CO_2 and form *COOH is slightly higher on the low-index Ag surfaces than on Zn facets ($\Delta G^{Ag}_{CO_2 \rightarrow {}^*COOH} > \Delta G^{Zn}_{CO_2 \rightarrow {}^*COOH}$). The same trend occurs for the *OCHO intermediate, where Zn surfaces show the lowest Gibbs free energy values ($\Delta G^{Ag}_{CO_2 \rightarrow {}^*OCHO} > \Delta G^{Zn}_{CO_2 \rightarrow {}^*OCHO}$). Interestingly, $\Delta G_{CO_2 \rightarrow {}^*OCHO}$ decreases in the order Ag(111) > Ag(100) > Ag(110) and Zn(0001) > Zn($10\bar{1}0$).

This result shows that the *OCHO stability increases as the degree of surface packing decreases and the atoms at the surface are more undercoordinated. The *OCHO formation is a spontaneous process on the Zn($10\bar{1}0$) facet ($\Delta G^{Zn(10\bar{1}0)}_{CO_2 \rightarrow {}^*OCHO} < 0$). Finally, considering HER, Figure 5.1 highlights that the formation of *H intermediates is disfavored compared to the*OCHO species for all surfaces, except for Ag(111), as

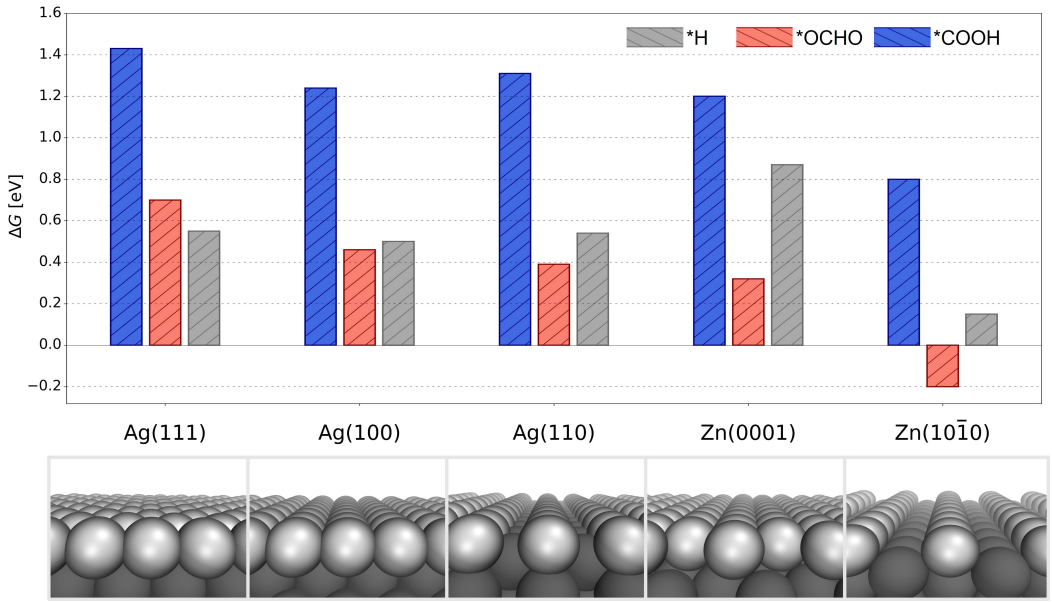


Figure 5.1 Top panel: ΔG values of *OCHO (red bar), *COOH (blue bar) and *H (grey bar) on the investigated low-index silver and zinc surfaces. The ΔG values for the formation of the intermediates *OCHO and *COOH correspond to the Eq.(5.1) and Eq.(5.2), respectively. The ΔG values for *H intermediate correspond to the Eq.(5.3). Bottom panel, from left to right: Ag(111), Ag(100), Ag(110), Zn(0001) and Zn(10$\bar{1}$0) surfaces.

$\Delta G^{\mathrm{Ag(111)}}_{\mathrm{CO_2}\rightarrow{}^*\mathrm{OCHO}} > \Delta G^{\mathrm{Ag(111)}}_{\mathrm{H^+}\rightarrow{}^*\mathrm{H}}$, where the hydrogen is adsorbed on the *fcc* site with higher stability.

Therefore, from a thermodynamic point of view, our calculations confirm what previous works already observed: silver and zinc electrodes are predicted to produce HCOOH and H_2, in contrast to what is observed experimentally. Therefore, a kinetic investigation must be performed to deepen our understanding of the reaction mechanisms and the energy barriers involved in CO_2RR on silver and zinc electrodes.

5.4 Reaction mechanisms

The CO_2 conversion towards CO and HCOOH can be achieved by two proton-electron transfers.Here, the two pathways that we kinetically investigate are the Tafel and the Heyrovsky mechanisms.

In the Tafel mechanism, the CO_2RR intermediate is obtained from the reaction between a CO_2 molecule and a hydrogen atom *H already adsorbed on the surface,

as

$$CO_2 + {}^{*}H \longrightarrow {}^{*}COOH \tag{5.4}$$

for *COOH and a related mechanism, a Tafel-like mechanism, involves concerted H atom and electron transfer [212] to CO_2 for $HCOO^-$ production, as

$$CO_2 + e^- + {}^{*}H \longrightarrow HCOO^- \tag{5.5}$$

The Heyrovsky mechanism firstly proceeds through the formation of either *COOH or *OCHO, in which the proton comes from the electrolyte. We consider hydronium ions (H_3O^+) as the proton source, so that we have

$$CO_2 + H_3O^+ + e^- + {}^{*} \longrightarrow {}^{*}COOH + H_2O \tag{5.6}$$

$$CO_2 + H_3O^+ + e^- + {}^{*} \longrightarrow {}^{*}OCHO + H_2O \tag{5.7}$$

The second PET occuring after Eq. (5.7) only releases formate, as

$${}^{*}OCHO + H_3O^+ + e^- \longrightarrow HCOOH + 2H_2O + {}^{*} \tag{5.8}$$

*COOH, instead, can react to form both HCOOH and CO, as evidenced by both experimental and theoretical studies [23, 203, 142]. Therefore, a second Heyrovsky-like PET may occur either as

$${}^{*}COOH + H_3O^+ + e^- \longrightarrow CO + 2H_2O + {}^{*}, \tag{5.9}$$

or

$${}^{*}COOH + H_3O^+ + e^- \longrightarrow HCOOH + H_2O + {}^{*}. \tag{5.10}$$

In addition, since the Tafel-like mechanism requires a hydrogen atom adsorbed on the metal surface, the Volmer-Heyrovsky mechanism for the HER was also considered [214]. This pathway of HER unfolds as

$$H_3O^+ + e^- + {}^{*} \longrightarrow {}^{*}H + H_2O, \tag{5.11}$$

$${}^{*}H + H_3O^+ + e^- \longrightarrow H_2 + H_2O + {}^{*}, \tag{5.12}$$

where the H^+ is transferred from an H_3O^+ in solution to the surface.

As discussed in Chapter 2, depending on the mechanism involved, the reaction pathway passes through a specific transition state (TS). This TS corresponds to a first-order saddle point of the the energy surface, and determines the magnitude of the kinetic barrier ($\Delta\Omega_{\text{act}}$).

For HER, we introduce the TSs in the reactions steps Eqs. (5.11) and (5.12) as

$$\underset{\text{initial}^{\text{Vol}}_{\text{HER}}}{\mathrm{H_3O^+ + e^- + {}^*}} \longrightarrow \underset{\text{TS}^{\text{Vol}}_{\text{HER}}}{[{}^*\cdot\cdot\mathrm{H}\cdot\cdot\mathrm{OH_2}]} \longrightarrow \underset{\text{final}^{\text{Vol}}_{\text{HER}}}{{}^*\mathrm{H} + \mathrm{H_2O}}, \tag{5.13}$$

for the first Volmer step, and

$$\underset{\text{initial}^{\text{Hey}}_{\text{HER}}}{{}^*\mathrm{H} + \mathrm{H_3O^+} + \mathrm{e^-}} \longrightarrow \underset{\text{TS}^{\text{Hey}}_{\text{HER}}}{[{}^*\mathrm{H}\cdot\cdot\mathrm{H}\cdot\cdot\mathrm{OH_2}]} \longrightarrow \underset{\text{final}^{\text{Hey}}_{\text{HER}}}{\mathrm{H_2} + \mathrm{H_2O} + {}^*}, \tag{5.14}$$

for the second, Heyrovsky, step.

Turning to CO_2RR, in the first step, reduced CO_2 can be adsorbed on the electrode surface either as *COOH

$$\underset{\text{initial}^{\text{Hey}}_{\text{CO}_2}}{\mathrm{CO_2} + \mathrm{H_3O^+} + \mathrm{e^-} + {}^*} \longrightarrow \underset{\text{TS}^{\text{Hey}}_{\text{CO}_2\rightarrow{}^*\text{COOH}}}{[{}^*\mathrm{CO_2}\cdot\cdot\mathrm{H}\cdot\cdot\mathrm{OH_2}]} \longrightarrow \underset{\text{final}^{\text{Hey}}_{{}^*\text{COOH}}}{{}^*\mathrm{COOH} + \mathrm{H_2O}}, \tag{5.15}$$

or *OCHO

$$\underset{\text{initial}^{\text{Hey}}_{\text{CO}_2}}{\mathrm{CO_2} + \mathrm{H_3O^+} + \mathrm{e^-} + {}^*} \longrightarrow \underset{\text{TS}^{\text{Hey}}_{\text{CO}_2\rightarrow{}^*\text{OCHO}}}{[{}^*\mathrm{CO_2}\cdot\cdot\mathrm{H}\cdot\cdot\mathrm{OH_2}]} \longrightarrow \underset{\text{final}^{\text{Hey}}_{{}^*\text{OCHO}}}{{}^*\mathrm{OCHO} + \mathrm{H_2O}}. \tag{5.16}$$

The reduction step of the *COOH intermediate to CO can be written as

$$\underset{\text{initial}^{\text{Hey}}_{{}^*\text{COOH}}}{{}^*\mathrm{COOH} + \mathrm{H_3O^+} + \mathrm{e^-}} \longrightarrow \underset{\text{TS}^{\text{Hey}}_{{}^*\text{COOH}\rightarrow\text{CO}}}{[{}^*\mathrm{CO_2H}\cdot\cdot\mathrm{H}\cdot\cdot\mathrm{OH_2}]} \longrightarrow \underset{\text{final}^{\text{Hey}}_{\text{CO}}}{\mathrm{CO} + 2\,\mathrm{H_2O} + {}^*} \tag{5.17}$$

and to HCOOH as

$$\underset{\text{initial}^{\text{Hey}}_{{}^*\text{COOH}}}{{}^*\mathrm{COOH} + \mathrm{H_3O^+} + \mathrm{e^-}} \longrightarrow \underset{\text{TS}^{\text{Hey}}_{{}^*\text{COOH}\rightarrow\text{HCOOH}}}{[{}^*\mathrm{COOH}\cdot\cdot\mathrm{H}\cdot\cdot\mathrm{OH_2}]} \longrightarrow \underset{\text{final}^{\text{Hey}}_{\text{HCOOH}}}{\mathrm{HCOOH} + \mathrm{H_2O} + {}^*}.. \tag{5.18}$$

The reduction step of *OCHO leads to HCOOH as

$$\underset{\text{initial}^{\text{Hey}}_{^*\text{OCHO}}}{^*\text{OCHO} + \text{H}_3\text{O}^+ + \text{e}^-} \longrightarrow \underset{\text{TS}^{\text{Hey}}_{^*\text{OCHO}\rightarrow\text{HCOOH}}}{[^*\text{OCHO}\cdot\cdot\text{H}\cdot\cdot\text{OH}_2]} \longrightarrow \underset{\text{final}^{\text{Hey}}_{\text{HCOOH}}}{\text{HCOOH} + \text{H}_2\text{O} + ^*} .. \tag{5.19}$$

Finally, assuming that a hydrogen atom is already adsorbed on the metal surface, the first step of CO_2RR may be Tafel-like and proceed as either

$$\underset{\text{initial}^{\text{Taf}}_{\text{CO}_2}}{^*\text{H} + \text{CO}_2 + ^*} \longrightarrow \underset{\text{TS}^{\text{Taf}}_{\text{CO}_2\rightarrow{}^*\text{COOH}}}{[^*\text{H}\cdot\cdot\text{CO}_2]} \longrightarrow \underset{\text{final}^{\text{Taf}}_{^*\text{COOH}}}{^*\text{COOH} + ^*}, \tag{5.20}$$

or

$$\underset{\text{initial}^{\text{Taf}}_{\text{CO}_2}}{^*\text{H} + \text{CO}_2 + \text{e}^- + ^*} \longrightarrow \underset{\text{TS}^{\text{Taf}}_{\text{CO}_2\rightarrow\text{HCOO}^-}}{[^*\text{H}\cdot\cdot\text{CO}_2]} \longrightarrow \underset{\text{final}^{\text{Taf}}_{\text{HCOO}^-}}{\text{HCOO}^- + ^*}. \tag{5.21}$$

In the following section, the computed activation energy barriers ($\Delta\Omega_{\text{act}}$) and the corresponding transition states of the presented reaction mechanisms are discussed.

5.5 Voltage-dependent activation energy calculations

The activation energy barriers ($\Delta\Omega_{\text{act}}$) involved in the various elementary steps for CO_2RR and HER were computed on the pristine Ag(111), Ag(100), Ag(110), Zn(0001) and Zn($10\bar{1}0$) surfaces under an applied external potential. Since experimental studies are performed at low/intermediate potential, kinetics controls the selectivity on silver and zinc electrodes. The $\Delta\Omega_{\text{act}}$ have been investigated at -0.4, -0.8, and -1.1 V vs RHE.

The DFT calculations for both CO_2RR and HER explicitly involve a hydronium species surrounded by three H_2O molecules to describe the solvated proton. The water cluster model corresponds to the "Eigen" cation in its protonated form, where the first solvation shell around the H_3O^+ core is filled by two H_2O hydrogen bond donors and one H_2O hydrogen bond acceptor [215, 216]. The rest of the electrolyte solution is represented by an implicit solvent model. The obtained saddle point configurations are similar among the surfaces investigated, and, for the sake of simplicity, only those found on the Ag(100) facet are shown as representative models for both CO_2RR and HER. For Tafel steps, the explicit water molecules and proton

are not included since the reaction involves a hydrogen adatom and thereby is not affected significantly by the presence of the solvent. Finally, a zero $\Delta\Omega_{act}$ value was set to reaction steps which do not involve a kinetic barrier.

5.5.1 Comparison between the Tafel and Heyorvsky mechanisms for CO_2RR

The TSs of the Tafel steps, Eqs. (5.20)-(5.21), the first Heyrovsky steps, Eqs. (5.15)-(5.16), and the second Heyrovsky steps, Eqs. (5.17)-(5.18) are shown in Figure 5.2.

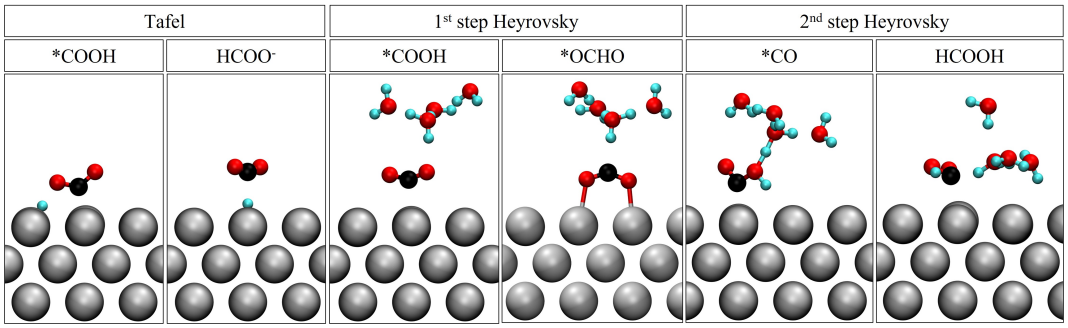


Figure 5.2 Optimized transition states configurations of Tafel and Heyrovsky reaction for CO_2RR. From left to right, the saddle points structures of: *COOH and $HCOO^-$ by Tafel mechanism; *COOH and *OCHO by the first step of Heyrovsky mechanism; *CO and HCOOH by the second step of Heyrovsky mechanism. Atom color code: grey for silver, red for oxygen, black for carbon and cyan for hydrogen atoms.

As in Ref. [213], we obtain that the chemisorbed *COOH species preferably binds to silver and zinc surfaces pointing its hydrogen atom toward the metal electrode and its stability increases with the magnitude of the applied voltage. Differently from the hydrogen atom attracted towards the electrode surface, oxygen atoms belonging to the CO_2 molecule are pushed away and the formate anion, $HCOO^-$, is repelled by the negatively charged surface.

Figure 5.2 shows that the transition state configurations of CO_2RR in the Tafel reaction $TS^{Taf}_{CO_2\rightarrow{}^*COOH}$ and $TS^{Taf}_{CO_2\rightarrow{}^*HCOO^-}$ involve the CO_2 activation by the electron transfer which leads to a bent CO_2 conformation, while the molecule is interacting with the *H species, slightly displaced from its equilibrium position. In the first step of the CO_2RR Heyrovsky reaction, the structures of both the $TS^{Hey}_{CO_2\rightarrow{}^*COOH}$ and $TS^{Hey}_{CO_2\rightarrow{}^*OCHO}$ arrangements show a bent CO_2 configuration chemisorbed on the

surface through a C-bond or an O-bond, respectively, with one hydrogen belonging to the H_3O^+ barely stretched towards CO_2.

The energy plots in Figure 5.3 present the $\Delta\Omega_{act}$ in eV of the Tafel steps, while in Figure 5.4 we report the $\Delta\Omega_{act}$ of the first Heyrovsky steps. Generally, it is possible

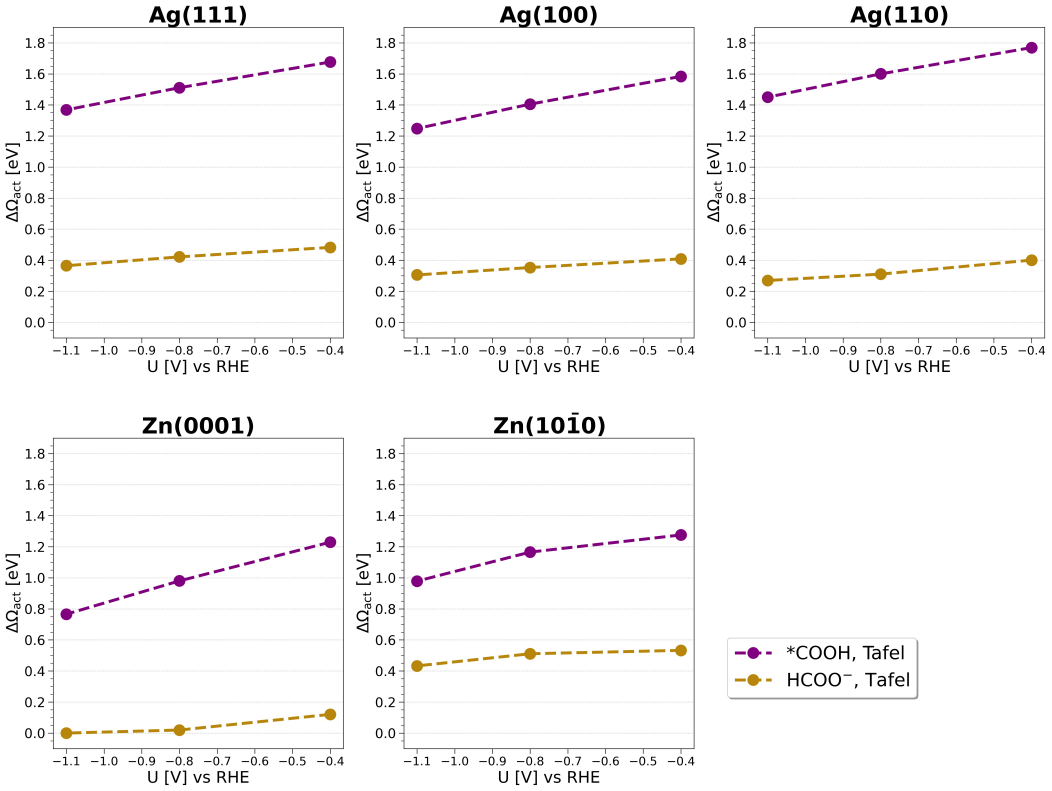


Figure 5.3 Calculated activation energies, $\Delta\Omega_{act}$ in eV, for the Tafel mechanism of CO_2RR on Ag(111), Ag(100), Ag(110), Zn(0001) and Zn(10$\bar{1}$0) at -0.4, -0.8, and -1.1 V vs. RHE. The purple and golden lines refer to Eqs. (5.20) and (5.21), respectively.

to observe a common trend, since in both mechanisms the energy barrier decreases as the magnitude of the applied negative bias increases. Moreover, the $\Delta\Omega_{act}$ decreases as the surface becomes more open. Indeed, densely close-packed surfaces, such as Ag(111) and Zn(0001), require overcoming higher energy barriers compared to their more open surfaces and make the reaction kinetically unfavored.

The panels in Figure 5.3 show that the Tafel step leading to *COOH presents a very high energy barrier (between 1.2 and 1.8 eV) on all three Ag surfaces, whereas the $\Delta\Omega_{act}$ of $HCOO^-$ formation is significantly lower. On the Zn facets, a similar

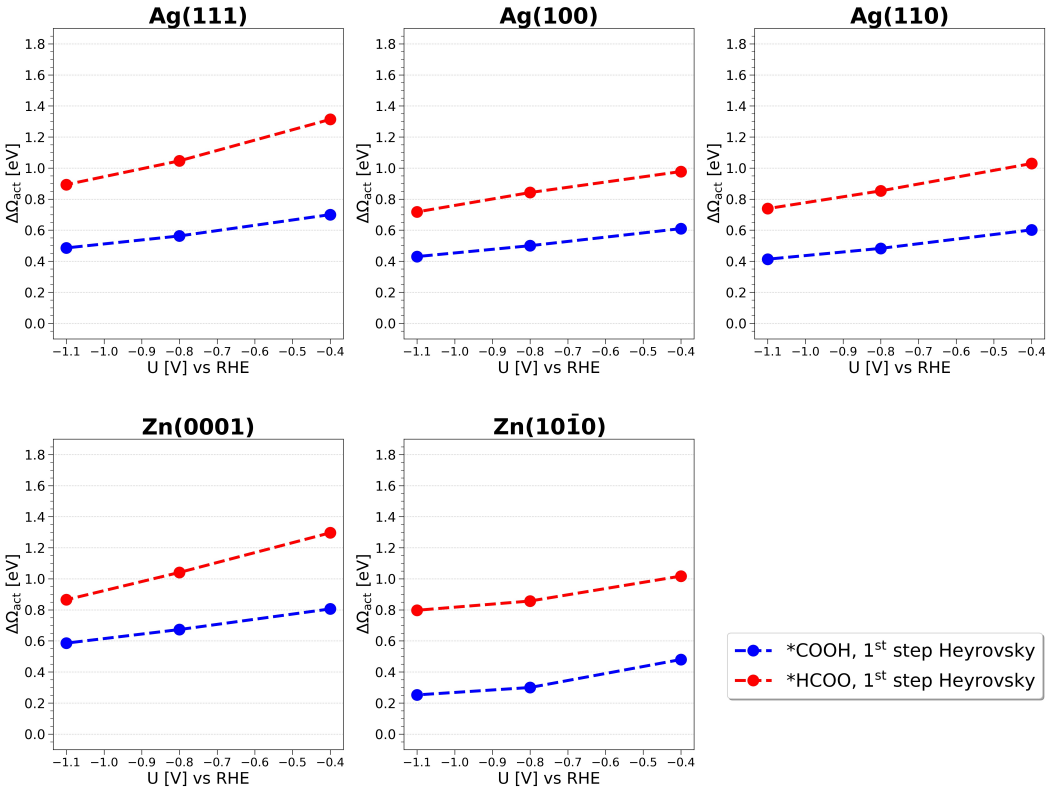


Figure 5.4 Calculated activation energy, $\Delta\Omega_{act}$ in eV, for the first step of the Heyrovsky mechanism of CO_2RR on Ag(111), Ag(100), Ag(110), Zn(0001) and Zn(10$\bar{1}$0) at -0.4, -0.8, and -1.1 V vs. RHE. The blue and red lines refer to Eqs. (5.15) and (5.16), respectively.

trend is observed, with the overall activation energy of *COOH formation being lower with respect to Ag surfaces and ranging from 1.0 to 1.4 eV. Nevertheless, the $HCOO^-$ species is still the preferred product. Notably, on the Zn(0001) facet, the formation of $HCOO^-$ becomes barrierless at -0.8 V vs RHE. Therefore, the Tafel mechanism favors the formation of $HCOO^-$ on all the investigated metal surfaces.

In contrast to the Tafel reaction, the energy plots relative to the first Heyrovsky steps of CO_2RR reveal that the *COOH formation is the kinetically favored process on both metals. The kinetic barriers for the *OCHO formation are higher than 0.8 eV over the entire potential range, while the highest $\Delta\Omega_{act}$ for the production of *COOH are 0.7 eV and 0.8 eV at -0.4 V vs RHE on Ag(111) and Zn(0001), respectively. As the magnitude of the applied bias U increases, $\Delta\Omega_{act}$ decreases for all surfaces and reaches just 0.25 eV on Zn(10$\bar{1}$0) at 1.1 V vs. RHE. On the contrary, the *OCHO formation is kinetically more demanding, resulting in a disfavored mechanism on Ag and Zn low-index surfaces. Therefore, we can conclude that the Heyrovsky mechanism prefers to proceed via the *COOH intermediate. Consequently, the second step of Heryrovsky reaction was investigated starting from *COOH, discarding the reaction step in Eq. (5.19).

Finally, *COOH can be converted to either CO or HCOOH, Eqs. (5.17)-(5.18), whose $\Delta\Omega_{act}$ are shown in Figure 5.5. The energy barriers for the formation of HCOOH are in the range of 0.8 eV to 0.4 eV as the potential becomes more negative. In the transition state $TS^{Hey}_{^*COOH\rightarrow HCOOH}$ the *COOH is arranged parallel to the metal surface and points its carbon towards the H_3O^+, c.f. Figure 5.2. On the other hand, the *COOH reduction to *CO requires lower activation energy ($\Delta\Omega_{act} < 0.4$ eV) for the entire potential range, involving a transition state $TS^{Hey}_{^*COOH\rightarrow CO}$ where the hydroxyl group is stretched while H_3O^+ is giving its proton. Hence, due to the the lower energy barriers, the reduction of *COOH leads to *CO formation, Eq. (5.17), in agreement with the experimental results on polycrystalline silver and zinc electrocatalysts.

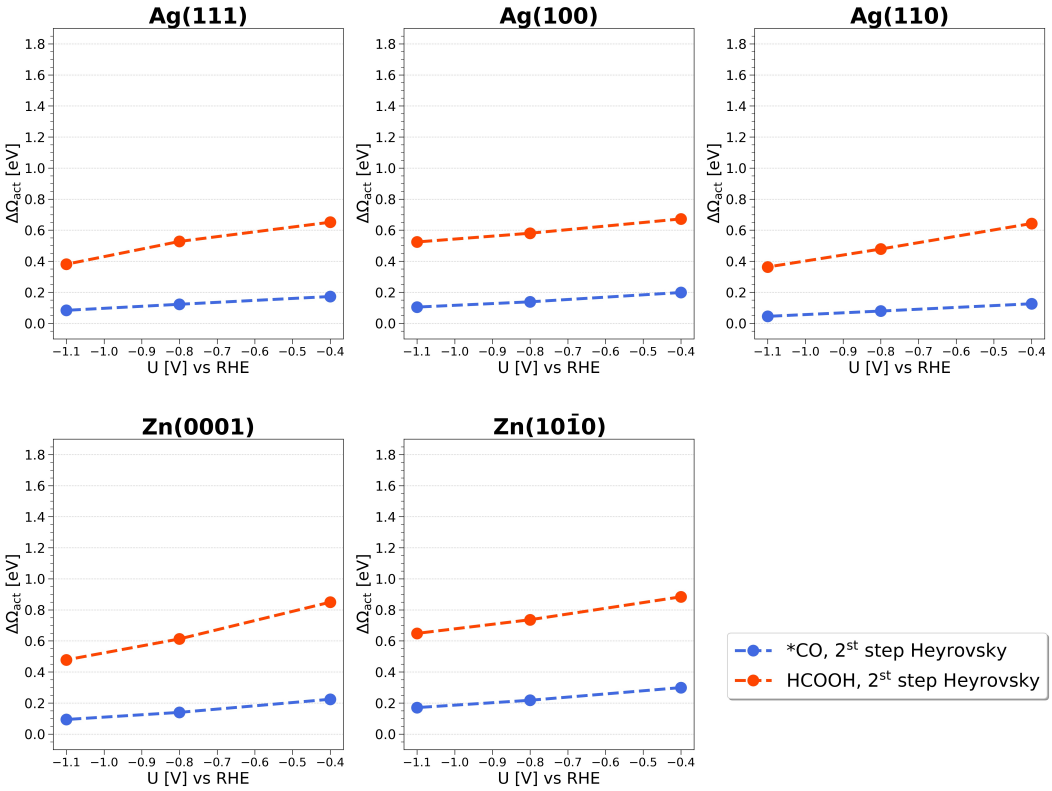


Figure 5.5 Calculated activation energies, $\Delta\Omega_{act}$ in eV, for the second step of the Heyrovsky mechanism of CO_2RR on Ag(111), Ag(100), Ag(110), Zn(0001) and Zn(10$\bar{1}$0) at -0.4, -0.8, and -1.1 V vs. RHE. The light blue and red lines refer to Eqs. (5.17) and (5.18), respectively.

5.5.2 Kinetic barriers of the Volmer-Heyrovsky mechanism for HER

The adsorbed hydrogen atom on the metal surface is a fundamental prerequisite for the CO_2RR Tafel mechanism to take place. Therefore, from a kinetic perspective, the

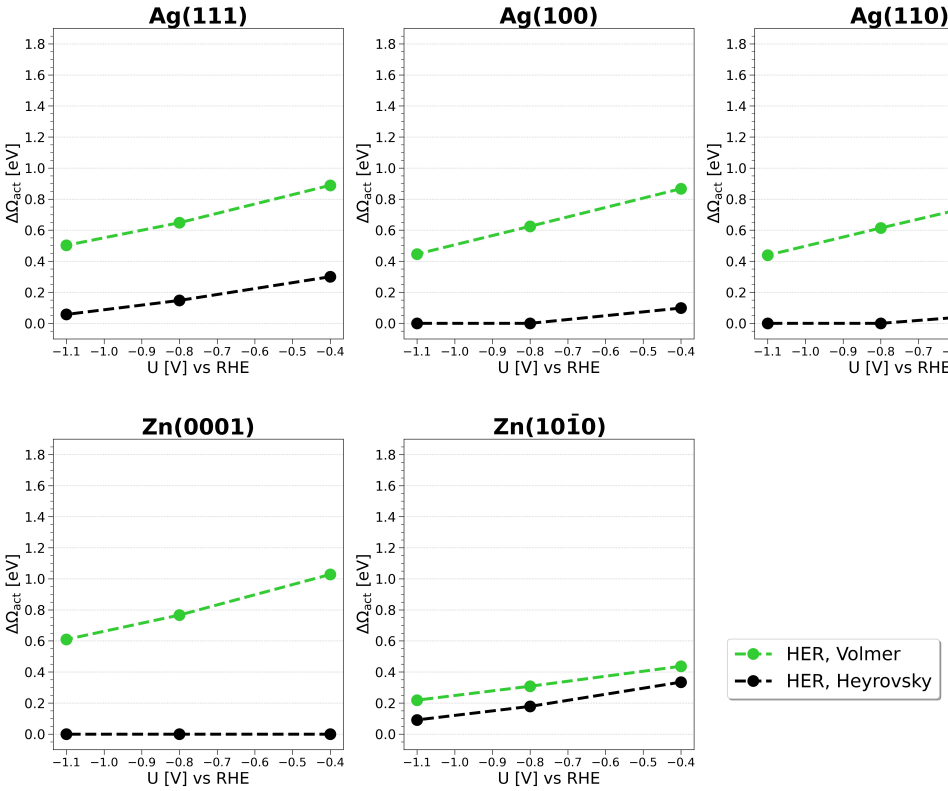


Figure 5.6 Calculated activation energies, $\Delta\Omega_{act}$ in eV, for the Volmer-Heyrovsky mechanism of HER on Ag(111), Ag(100), Ag(110), Zn(0001) and Zn(10$\bar{1}$0) at -0.4, -0.8, and -1.1 VRHE. The green and black lines represents Eqs. (5.13) and (5.14), respectively.

hydrogen adsorption via Volmer reaction and the consequent H_2 evolution through the Heyrovsky mechanism were also kinetically investigated to verify the feasibility of the Tafel-like CO_2 reduction and to compare the competitive HER to CO_2RR.

The optimized saddle point structures found along the Volmer (TS^{Vol}_{HER}) and the Heyrovsky (TS^{Hey}_{HER}) reaction paths are shown in Figure 5.7. In TS^{Vol}_{HER}, the proton belonging to the H_3O^+ is halfway transferred to the electrode surface. Once adsorbed,

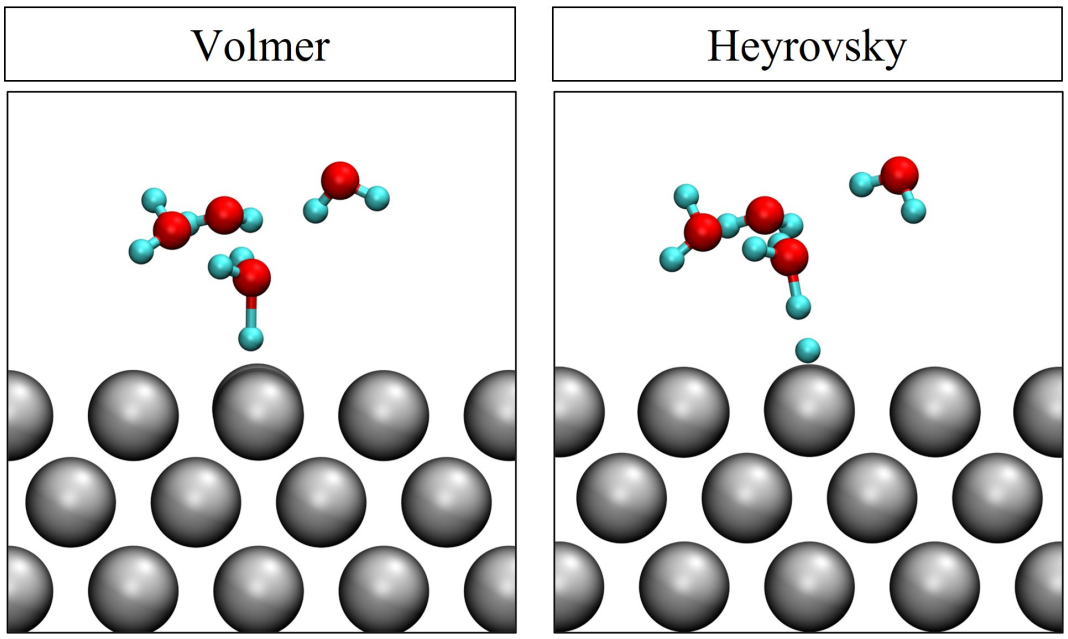


Figure 5.7 Optimized transition states configurations of Volmer (left) and Heyrovsky (right) TS of HER. Atom color code: grey for silver, red for oxygen and cyan for hydrogen atoms.

another H_3O^+ provides a second hydrogen via TS_{HER}^{Hey} where the $^*H$ is slightly moved away from the surface and points towards the H_3O^+ which extends its O-H bond.

The calculated activation energies of both mechanisms are displayed in Figure 5.6. Generally, for the Volmer reaction on silver, $\Delta\Omega_{act}$ reaches almost 1.0 eV at low potentials (-0.4 V vs RHE), and decreases to about 0.4 eV when a potential of -1.1 V vs RHE is applied. Once hydrogen is adsorbed, the Heyrovsky reaction occurs involving very low activation energy values ($\Delta\Omega_{act} < 0.4$ eV) over the entire U range. This step becomes barrierless ($\Delta\Omega_{act} < 0$ eV) on Ag(100) and Ag(111) at potential lower than about -0.8 V vs. RHE.

An energy trend similar to the one observed for the silver surfaces is found on the Zn(0001) facet, while the Zn(10$\bar{1}$0) surface involves lower activation energies for the HER Volmer for the whole U range (about $\Delta\Omega_{act} < 0.4$ eV) as well as the following Heyrovsky step. Generally, on all the low-index Ag and Zn surfaces, once the hydrogen is adsorbed via HER Volmer reaction, the H_2 evolution through the Heyrovsky mechanism, Eq. (5.14) is kinetically favored with respect to the CO_2 reduction to $HCOO^-$ via Tafel reaction, Eq. (5.21), hindering the latter mechanism.

However, comparing the kinetic barriers of the HER Volmer reaction, Eq. (5.13), with the first step of the CO_2RR Heyrovsky mechanism, Eq. (5.15), the formation of the *COOH intermediate requires lower activation energies rather than the *H species, representing the rate-determining step on the Ag and Zn surfaces for all the investigated U values. Therefore, our theoretical results suggest that the favored CO_2RR pathway on all studied surfaces is the Heyrovsky mechanism via Eqs. (5.15)-(5.17), leading to CO production.

5.6 Conclusions

In conclusion, our theoretical analysis shows that, on all the Ag and Zn surfaces, the primary pathway for the formation of $HCOO^-$ is the Tafel reaction. However, the Volmer reaction for the hydrogen adsorption on the surface is involves a high energy barrier, thus hindering the formate production via this mechanism. This suggests that CO_2RR proceeds via the Heyrovsky mechanism on all investigated surfaces. The rate determining step is the first proton-electron transfer for CO_2 conversion to *COOH at all applied voltages. Finally, the calculated activation energies relative to the second proton-electron transfer of the CO_2RR Heyrovsky mechanism show that *COOH does not form HCOOH, but is converted to CO. This investigation allows to understand that, while HCOOH is thermodynamically preferred, the experimentally observed Ag and Zn selectivity towards CO is determined by kinetic aspects.

With the exception of the Zn($10\bar{1}0$) facet, the computed kinetic barriers seem to suggest that CO production is always promoted, even at less negative voltages, while experiments prove that at these low overpotentials HER dominates. One possible explanation for this discrepancy is that our investigation focused solely on pristine flat surfaces, without taking into account the presence of morphological defects, such as atom vacancies, steps or edges, which may have a greater selectivity and activity towards HER. Recent studies demonstrated that H_2 production increases as the amount of edge sites increases [217, 218]. Masel and coworkers [217] studied the catalytic performance of CO_2RR to CO on Ag nanoparticles as a function of their size, showing a strong correlation between the selectivity towards either reaction and the particle size. Indeed, they observed that the rate of CO_2 conversion to CO significantly drops when the nanoparticle diameter is reduced below 5 nm,

favoring HER. The authors assigned this variation to the change in binding energy of the key intermediates as the particle size decreases. A computational study of the experimental observations of Masel and coworkers was provided by Back et al. [219], who calculated the binding energies of CO_2RR and HER intermediates on different active sites of Ag and Au nanoparticles. In this work, the authors state that under-coordinated sites, like corners and edges, are the main active sites for the reaction intermediates. Starting from these studies, Deng et al. [218] performed a combination of DFT, microkinetic, and experimental investigations to understand the size-dependent selectivity in the critical sub-5 nm range for Ag nanoparticles. The results of the study indicate that Ag(100) and Ag edge sites have a significant impact on CO_2RR and HER, respectively. As the particle diameter decreases, the HER activity improves due to an increase in the density of Ag edge sites, while the activity towards CO_2RR decreases. Future research should then explore defective surfaces that presents edges, steps, and corner sites to gain a deeper understanding of how kinetics controls the transition from CO_2RR to HER on silver and zinc electrocatalysts.

Conclusions

This thesis work employed DFT calculations to gain a deeper understanding of selective electrocatalysts for the conversion of CO_2 into valuable products. The approach to this challenging task has been two-fold, focusing on both thermodynamic and kinetic investigations.

The thermodynamic approach has been particularly useful in interpreting unresolved experimental measurements concerning the relation between structure and catalytic performance of materials, as well as predicting the chemical and physical properties of electrocatalysts. The findings of this study provided valuable guidelines for the experimental development of electrocatalysts in the laboratory.
To investigate the role of the surface structure of SnO_2 electrocatalysts towards the selective reduction of CO_2 to HCOOH, the most thermodynamically stable low-index surface of SnO_2, $SnO_2(110)$, was used to model the pristine surface of the oxide electrode. The results demonstrate that the $SnO_2(110)$ surface is intrinsically inactive for CO_2RR and HER, but, in the presence of an applied potential, the surface self-reduces and an outermost layer of metallic tin atoms is formed. At this stage, the material becomes selective for HCOOH. As the reduction degree of the surface increases and the thickness of the metallic phase grows at higher bias, the catalyst loses its selectivity. Therefore, these findings elucidate the experimental observations of both the metallic and oxide phases: signals of oxidized species, Sn^{II}, originate from the sub-surfaces SnO_2 layers, while the outermost metal thin phase, Sn^0, plays the catalytic key role.

Next, a theory-guided catalyst design was performed for the successive experimental synthesis of ZIF-8 as a performing electrocatalyst for the CO_2 capture and conversion to CO. Through DFT calculations, the thermodynamic analysis shows that the surface termination of ZIF-8 exposes imidazole-imidazolate pairs. Morever

our results show that the imidazolate moieties present at the ZIF-8 surface are able to coordinate the CO_2 molecule through its nitrogen atom. Once captured, the CO_2 is selectively reduced to CO if an external bias is applied to a ZIF-8 covered electrode. We also focused on increasing ZIF-8 catalytic performance by using CNTs as support and tuning the size of the catalytic ZIF-8 samples. The calculations highlight an enhancement in terms of selectivity once ZIF-8 is supported on CNTs, as well as when the catalyst/CNTs contact increases, reducing the size of catalyst particle size. These computational guidelines were validated by following experimental investigation.

The final part of the thesis aimed to understand the selective conversion of CO_2 to CO on silver and zinc metal electrodes through a kinetic study. Two main CO_2RR mechanisms, the Tafel and Heyrovsky reactions for CO and HCOOH production, were investigated and compared to the Volmer-Heyrovsky mechanism of HER on pristine low-index Ag and Zn surfaces. The estimated activation energy barriers for CO_2RR on all surfaces indicated that the Tafel mechanism leads to formate and cannot occur because the kinetic barrier of the Heyrovsky step is much lower and leads to the release of CO. However, these results show that CO_2RR is generally favored over HER for the entire explored range of potentials ($-1.1 \div -0.4$ V vs. RHE), which contradicts experimental results. We propose that this discrepancy can be attributed to the absence of morphological defects in the theoretical simulations, as only flat pristine surfaces were investigated. Further theoretical studies are required to gain better insights into how kinetics controls silver and zinc selectivity, taking into account more realistic surface geometries.

Bibliography

[1] Steven Chu and Arun Majumdar. Opportunities and challenges for a sustainable energy future. *Nature*, 488(7411):294–303, 2012.

[2] Joeri Rogelj, Michel Den Elzen, Niklas Höhne, Taryn Fransen, Hanna Fekete, Harald Winkler, Roberto Schaeffer, Fu Sha, Keywan Riahi, and Malte Meinshausen. Paris Agreement climate proposals need a boost to keep warming well below 2 °c. *Nature*, 534(7609):631–639, 2016.

[3] Jeremy D. Shakun, Peter U. Clark, Feng He, Shaun A. Marcott, Alan C. Mix, Zhengyu Liu, Bette Otto-Bliesner, Andreas Schmittner, and Edouard Bard. Global warming preceded by increasing carbon dioxide concentrations during the last deglaciation. *Nature*, 484(7392):49–54, 2012.

[4] https://ourworldindata.org/grapher/annual-co-emissions-by-region.

[5] Sichao Ma, Paul JA Kenis, et al. Electrochemical conversion of CO_2 to useful chemicals: current status, remaining challenges, and future opportunities. *Current Opinion in Chemical Engineering*, 2(2):191–199, 2013.

[6] Sean Overa, Byung Hee Ko, Yaran Zhao, and Feng Jiao. Electrochemical Approaches for CO_2 Conversion to Chemicals: A Journey toward Practical Applications. *Accounts of Chemical Research*, 55(5):638–648, 2022.

[7] Hossein Salehizadeh, Ning Yan, and Ramin Farnood. Recent advances in microbial CO_2 fixation and conversion to value-added products. *Chemical engineering journal*, 390:124584, 2020.

[8] Shaikh Abdur Razzak, Saad Aldin M Ali, Mohammad Mozahar Hossain, and Hugo deLasa. Biological CO_2 fixation with production of microalgae in wastewater–a review. *Renewable and Sustainable Energy Reviews*, 76:379–390, 2017.

[9] Vyacheslav Romanov, Yee Soong, Casey Carney, Gilbert E Rush, Benjamin Nielsen, and William O'Connor. Mineralization of carbon dioxide: a literature review. *ChemBioEng Reviews*, 2(4):231–256, 2015.

[10] Sandra Ó Snæbjörnsdóttir, Bergur Sigfússon, Chiara Marieni, David Goldberg, Sigurður R Gislason, and Eric H Oelkers. Carbon dioxide storage through

mineral carbonation. *Nature Reviews Earth & Environment*, 1(2):90–102, 2020.

[11] Zhiqiang Ma and Marc D Porosoff. Development of tandem catalysts for CO_2 hydrogenation to olefins. *ACS Catalysis*, 9(3):2639–2656, 2019.

[12] Michael North, Pedro Villuendas, and Carl Young. A gas-phase flow reactor for ethylene carbonate synthesis from waste carbon dioxide. *Chemistry–A European Journal*, 15(43):11454–11457, 2009.

[13] Ana S. Reis Machado and Manuel Nunes da Ponte. CO_2 capture and electrochemical conversion. *Current Opinion in Green and Sustainable Chemistry*, 11:86–90, 2018.

[14] Federica Proietto, Urvi Patel, Alessandro Galia, and Onofrio Scialdone. Electrochemical conversion of CO_2 to formic acid using a Sn based electrode: A critical review on the state-of-the-art technologies and their potential. *Electrochimica Acta*, 389:138753, 2021.

[15] Oriol Gutiérrez Sánchez, Yuvraj Y Birdja, Metin Bulut, Jan Vaes, Tom Breugelmans, and Deepak Pant. Recent advances in industrial CO_2 electroreduction. *Current Opinion in Green and Sustainable Chemistry*, 16:47–56, 2019.

[16] Qi Lu and Feng Jiao. Electrochemical CO_2 reduction: Electrocatalyst, reaction mechanism, and process engineering. *Nano Energy*, 29:439–456, 2016.

[17] Shuyu Liang, Naveed Altaf, Liang Huang, Yanshan Gao, and Qiang Wang. Electrolytic cell design for electrochemical CO_2 reduction. *Journal of CO2 Utilization*, 35(September 2019):90–105, 2020.

[18] David M. Weekes, Danielle A. Salvatore, Angelica Reyes, Aoxue Huang, and Curtis P. Berlinguette. Electrolytic CO_2 Reduction in a Flow Cell. *Accounts of Chemical Research*, 51(4):910–918, 2018.

[19] Fengjiao Yu, Penghui Wei, Yang Yang, Yuhui Chen, Limin Guo, and Zhangquan Peng. Material design at nano and atomic scale for electrocatalytic CO_2 reduction. *Nano Materials Science*, 1(1):60–69, 2019.

[20] Progress and Perspective of Electrocatalytic CO_2 Reduction for Renewable Carbonaceous Fuels and Chemicals. *Advanced Science*, 5(1), 2018.

[21] Matthew Jouny, Wesley Luc, and Feng Jiao. General Techno-Economic Analysis of CO_2 Electrolysis Systems. *Industrial and Engineering Chemistry Research*, 57(6):2165–2177, 2018.

[22] Wanfeng Yang, Kamran Dastafkan, Chen Jia, and Chuan Zhao. Design of electrocatalysts and electrochemical cells for carbon dioxide reduction reactions. *Advanced Materials Technologies*, 3(9):1700377, 2018.

[23] Ruud Kortlever, Jing Shen, Klaas Jan P Schouten, Federico Calle-Vallejo, and Marc TM Koper. Catalysts and reaction pathways for the electrochemical reduction of carbon dioxide. *The journal of physical chemistry letters*, 6(20):4073–4082, 2015.

[24] Nicolas Dubouis and Alexis Grimaud. The hydrogen evolution reaction: from material to interfacial descriptors. *Chemical Science*, 10(40):9165–9181, 2019.

[25] Eric E. Benson, Clifford P. Kubiak, Aaron J. Sathrum, and Jonathan M. Smieja. Electrocatalytic and homogeneous approaches to conversion of CO_2 to liquid fuels. *Chemical Society Reviews*, 38(1):89–99, 2009.

[26] Cyrille Costentin, Marc Robert, and Jean Michel Savéant. Catalysis of the electrochemical reduction of carbon dioxide. *Chemical Society Reviews*, 42(6):2423–2436, 2013.

[27] Eric E Benson, Clifford P Kubiak, Aaron J Sathrum, and Jonathan M Smieja. Electrocatalytic and homogeneous approaches to conversion of CO_2 to liquid fuels. *Chemical Society Reviews*, 38(1):89–99, 2009.

[28] Sheng Zhang, Qun Fan, Rong Xia, and Thomas J. Meyer. CO_2 Reduction: From Homogeneous to Heterogeneous Electrocatalysis. *Accounts of Chemical Research*, 53(1):255–264, 2020.

[29] Dong Dong Zhu, Jin Long Liu, and Shi Zhang Qiao. Recent Advances in Inorganic Heterogeneous Electrocatalysts for Reduction of Carbon Dioxide. *Advanced Materials*, 28(18):3423–3452, 2016.

[30] Guanyu Liu, Thanh Tran-Phu, Hongjun Chen, and Antonio Tricoli. A Review of Metal- and Metal-Oxide-Based Heterogeneous Catalysts for Electroreduction of Carbon Dioxide. *Advanced Sustainable Systems*, 2(8-9):1–13, 2018.

[31] Yuhou Pei, Heng Zhong, and Fangming Jin. A brief review of electrocatalytic reduction of CO_2—Materials, reaction conditions, and devices. *Energy Science and Engineering*, 9(7):1012–1032, 2021.

[32] Bijandra Kumar, Joseph P. Brian, Veerendra Atla, Sudesh Kumari, Kari A. Bertram, Robert T. White, and Joshua M. Spurgeon. New trends in the development of heterogeneous catalysts for electrochemical CO_2 reduction. *Catalysis Today*, 270:19–30, 2016.

[33] Chang Long, Xiang Li, Jun Guo, Yanan Shi, Shaoqin Liu, and Zhiyong Tang. Electrochemical reduction of co_2 over heterogeneous catalysts in aqueous solution: recent progress and perspectives. *Small Methods*, 3(3):1800369, 2019.

[34] P. R. Yaashikaa, P. Senthil Kumar, Sunita J. Varjani, and A. Saravanan. A review on photochemical, biochemical and electrochemical transformation of CO_2 into value-added products. *Journal of CO2 Utilization*, 33(March):131–147, 2019.

[35] Y i Hori. Electrochemical CO_2 reduction on metal electrodes. *Modern aspects of electrochemistry*, pages 89–189, 2008.

[36] P. Prabhu, Vishal Jose, and Jong Min Lee. Heterostructured Catalysts for Electrocatalytic and Photocatalytic Carbon Dioxide Reduction. *Advanced Functional Materials*, 30(24), 2020.

[37] Mariana CO Monteiro, Matthew F Philips, Klaas Jan P Schouten, and Marc TM Koper. Efficiency and selectivity of CO_2 reduction to CO on gold gas diffusion electrodes in acidic media. *Nature Communications*, 12(1):1–7, 2021.

[38] Qi Lu, Jonathan Rosen, Yang Zhou, Gregory S. Hutchings, Yannick C. Kimmel, Jingguang G. Chen, and Feng Jiao. A selective and efficient electrocatalyst for carbon dioxide reduction. *Nature Communications*, 5:1–6, 2014.

[39] Aicheng Chen and Cassandra Ostrom. Palladium-Based Nanomaterials: Synthesis and Electrochemical Applications. *Chemical Reviews*, 115(21):11999–12044, 2015.

[40] Zhenni Yang, Freddy E. Oropeza, and Kelvin H.L. Zhang. P-block metal-based (Sn, In, Bi, Pb) electrocatalysts for selective reduction of CO_2 to formate. *APL Materials*, 8(6), 2020.

[41] Jinli Yu, Juan Wang, Yangbo Ma, Jingwen Zhou, Yunhao Wang, Pengyi Lu, Jinwen Yin, Ruquan Ye, Zonglong Zhu, and Zhanxi Fan. Recent Progresses in Electrochemical Carbon Dioxide Reduction on Copper-Based Catalysts toward Multicarbon Products. *Advanced Functional Materials*, 31(37):1–28, 2021.

[42] Syed Shoaib Ahmad Shah, Tayyaba Najam, Ming Wen, Shuang-Quan Zang, Amir Waseem, and Hai-Long Jiang. Metal–organic framework-based electrocatalysts for co_2 reduction. *Small Structures*, 3(5):2100090, 2022.

[43] Zengqiang Gao, Junjun Li, Zhicheng Zhang, and Wenping Hu. Recent advances in carbon-based materials for electrochemical CO_2 reduction reaction. *Chinese Chemical Letters*, 33(5):2270–2280, 2022.

[44] Chuangang Hu, Ying Xiao, Yuqin Zou, and Liming Dai. Carbon-based metal-free electrocatalysis for energy conversion, energy storage, and environmental protection. *Electrochemical Energy Reviews*, 1:84–112, 2018.

[45] Qiang Wu, Lijun Yang, Xizhang Wang, and Zheng Hu. Carbon-based nanocages: a new platform for advanced energy storage and conversion. *Advanced Materials*, 32(27):1904177, 2020.

[46] Dunfeng Gao, Tianfu Liu, Guoxiong Wang, and Xinhe Bao. Structure Sensitivity in Single-Atom Catalysis toward CO_2 Electroreduction. *ACS Energy Letters*, 6(2):713–727, 2021.

[47] Huilong Fei, Juncai Dong, Dongliang Chen, Tiandou Hu, Xidong Duan, Imran Shakir, Yu Huang, and Xiangfeng Duan. Single atom electrocatalysts supported on graphene or graphene-like carbons. *Chemical Society Reviews*, 48(20):5207–5241, 2019.

[48] Minhan Li, Haifeng Wang, Wei Luo, Peter C. Sherrell, Jun Chen, and Jianping Yang. Heterogeneous Single-Atom Catalysts for Electrochemical CO_2 Reduction Reaction. *Advanced Materials*, 32(34), 2020.

[49] Leilei Zhang, Yujing Ren, Wengang Liu, Aiqin Wang, and Tao Zhang. Single-atom catalyst: A rising star for green synthesis of fine chemicals. *National Science Review*, 5(5):653–672, 2018.

[50] Huijuan Wu, Weiqiong Zheng, Ran Zhu, Mi Zhou, Xiancheng Ren, Yinghan Wang, Chong Cheng, Hongju Zhou, and Sujiao Cao. Modulating coordination structures and metal environments of MOFs-Engineered electrocatalysts for water electrolysis. *Chemical Engineering Journal*, page 139475, 2022.

[51] Anastasiya Bavykina, Nikita Kolobov, Il Son Khan, Jeremy A Bau, Adrian Ramirez, and Jorge Gascon. Metal–organic frameworks in heterogeneous catalysis: recent progress, new trends, and future perspectives. *Chemical reviews*, 120(16):8468–8535, 2020.

[52] Kayode Adesina Adegoke and Nobanathi Wendy Maxakato. Porous metal-organic framework (MOF)-based and MOF-derived electrocatalytic materials for energy conversion. *Materials Today Energy*, 21:100816, 2021.

[53] Hanguang Zhang, Jiazhan Li, Qiang Tan, Leilei Lu, Zhenbo Wang, and Gang Wu. Metal–Organic Frameworks and Their Derived Materials as Electrocatalysts and Photocatalysts for CO_2 Reduction: Progress, Challenges, and Perspectives. *Chemistry - A European Journal*, 24(69):18137–18157, 2018.

[54] Hassan Ait Ahsaine and Amal BaQais. Metal and metal oxide electrocatalysts for the electrochemical reduction of CO_2-to-C1 chemicals: are we there yet? *Green Chemistry Letters and Reviews*, 16(1):2160215, 2023.

[55] Kayode Adesina Adegoke, Rhoda Oyeladun Adegoke, Asiata Omotayo Ibrahim, Samson Ademola Adegoke, and Olugbenga Solomon Bello. Electrocatalytic conversion of CO_2 to hydrocarbon and alcohol products: Realities and prospects of cu-based materials. *Sustainable Materials and Technologies*, 25:e00200, 2020.

[56] M. Gattrell, N. Gupta, and A. Co. A review of the aqueous electrochemical reduction of CO_2 to hydrocarbons at copper. *Journal of Electroanalytical Chemistry*, 594(1):1–19, 2006.

[57] Karthish Manthiram, Brandon J. Beberwyck, and A. Paul Alivisatos. Enhanced electrochemical methanation of carbon dioxide with a dispersible nanoscale copper catalyst. *Journal of the American Chemical Society*, 136(38):13319–13325, 2014.

[58] David Raciti, Kenneth J. Livi, and Chao Wang. Highly Dense Cu Nanowires for Low-Overpotential CO_2 Reduction. *Nano Letters*, 15(10):6829–6835, 2015.

[59] Recep Kas, Khalid Khazzal Hummadi, Ruud Kortlever, Patrick De Wit, Alexander Milbrat, Mieke W.J. Luiten-Olieman, Nieck E. Benes, Marc T.M. Koper, and Guido Mul. Three-dimensional porous hollow fibre copper electrodes for efficient and high-rate electrochemical carbon dioxide reduction. *Nature Communications*, 7, 2016.

[60] Anthony Vasileff, Chaochen Xu, Yan Jiao, Yao Zheng, and Shi Zhang Qiao. Surface and Interface Engineering in Copper-Based Bimetallic Materials for Selective CO_2 Electroreduction. *Chem*, 4(8):1809–1831, 2018.

[61] Dongwei Du, Rong Lan, John Humphreys, Sivaprakash Sengodan, Kui Xie, Huanting Wang, and Shanwen Tao. Achieving Both High Selectivity and Current Density for CO_2 Reduction to Formate on Nanoporous Tin Foam Electrocatalysts. *ChemistrySelect*, 1(8):1711–1715, 2016.

[62] Fengcai Lei, Wei Liu, Yongfu Sun, Jiaqi Xu, Katong Liu, Liang Liang, Tao Yao, Bicai Pan, Shiqiang Wei, and Yi Xie. Metallic tin quantum sheets confined in graphene toward high-efficiency carbon dioxide electroreduction. *Nature Communications*, 7:1–8, 2016.

[63] Wesley Luc, Charles Collins, Siwen Wang, Hongliang Xin, Kai He, Yijin Kang, and Feng Jiao. Ag-Sn bimetallic catalyst with a core-shell structure for CO_2 reduction. *Journal of the American Chemical Society*, 139(5):1885–1893, 2017.

[64] Song Yi Choi, Soon Kwan Jeong, Hak Joo Kim, Il Hyun Baek, and Ki Tae Park. Electrochemical Reduction of Carbon Dioxide to Formate on Tin-Lead Alloys. *ACS Sustainable Chemistry and Engineering*, 4(3):1311–1318, 2016.

[65] Qiang Lai, Na Yang, and Gaoqing Yuan. Highly efficient In–Sn alloy catalysts for electrochemical reduction of CO_2 to formate. *Electrochemistry Communications*, 83(August):24–27, 2017.

[66] Yoshio Hori, Hidetoshi H I Wakebe, Toshio Tsukamoto, and Osamu Koga. Electrocatalytic Process of CO Selectivity in Electrochemical Reduction of CO_2 at Metal Electrodes in Aqueous Media. *Electrochimica Acta*, 39(11-12):1833–1839, 1994.

[67] Hessam Jahangiri, James Bennett, Parvin Mahjoubi, Karen Wilson, and Sai Gu. A review of advanced catalyst development for Fischer-Tropsch synthesis of hydrocarbons from biomass derived syn-gas. *Catalysis Science and Technology*, 4(8):2210–2229, 2014.

[68] Selwyn Hanselman, Marc T.M. Koper, and Federico Calle-Vallejo. Computational Comparison of Late Transition Metal (100) Surfaces for the Electrocatalytic Reduction of CO to C_2 Species. *ACS Energy Letters*, 3(5):1062–1067, 2018.

[69] Yoshio Hori, Akira Murata, Katsuhei Kikuchi, and Shin Suzuki. Electrochemical reduction of carbon dioxides to carbon monoxide at a gold electrode in aqueous potassium hydrogen carbonate. *Journal of the chemical society, chemical communications*, (10):728–729, 1987.

[70] Nagahiro Hoshi, Makiko Kato, and Yoshio Hori. Electrochemical reduction of CO_2 on single crystal electrodes of silver Ag(111), Ag(100) and Ag(110). *Journal of Electroanalytical Chemistry*, 440(1-2):283–286, 1997.

[71] Jonathan Rosen, Gregory S. Hutchings, Qi Lu, Robert V. Forest, Alex Moore, and Feng Jiao. Electrodeposited Zn Dendrites with Enhanced CO Selectivity for Electrocatalytic CO_2 Reduction. *ACS Catalysis*, 5(8):4586–4591, 2015.

[72] A. Bandi. Electrochemical Reduction of Carbon Dioxide on Conductive Metallic Oxides. *Journal of The Electrochemical Society*, 137(7):2157–2160, 1990.

[73] Shan Gao, Zhongti Sun, Wei Liu, Xingchen Jiao, Xiaolong Zu, Qitao Hu, Yongfu Sun, Tao Yao, Wenhua Zhang, Shiqiang Wei, and Yi Xie. Atomic layer confined vacancies for atomic-level insights into carbon dioxide electroreduction. *Nature Communications*, 8, 2017.

[74] Jia Jia, Chenxi Qian, Yuchan Dong, Young Feng Li, Hong Wang, Mireille Ghoussoub, Keith T. Butler, Aron Walsh, and Geoffrey A. Ozin. Heterogeneous catalytic hydrogenation of CO_2 by metal oxides: Defect engineering-perfecting imperfection. *Chemical Society Reviews*, 46(15):4631–4644, 2017.

[75] Wei Zhang, Baohua Jia, Xue Liu, and Tianyi Ma. Surface and interface chemistry in metal-free electrocatalysts for electrochemical CO_2 reduction. *SmartMat*, 3(1):5–34, 2022.

[76] Yihong Chen and Matthew W. Kanan. Tin oxide dependence of the CO_2 reduction efficiency on tin electrodes and enhanced activity for tin/tin oxide thin-film catalysts. *Journal of the American Chemical Society*, 134(4):1986–1989, 2012.

[77] Chan Woo Lee, Jung Sug Hong, Ki Dong Yang, Kyoungsuk Jin, Jun Ho Lee, Hyo Yong Ahn, Hongmin Seo, Nark Eon Sung, and Ki Tae Nam. Selective Electrochemical Production of Formate from Carbon Dioxide with Bismuth-Based Catalysts in an Aqueous Electrolyte. *ACS Catalysis*, 8(2):931–937, 2018.

[78] Hemma Mistry, Ana Sofia Varela, Cecile S. Bonifacio, Ioannis Zegkinoglou, Ilya Sinev, Yong Wook Choi, Kim Kisslinger, Eric A. Stach, Judith C. Yang, Peter Strasser, and Beatriz Roldan Cuenya. Highly selective plasma-activated

copper catalysts for carbon dioxide reduction to ethylene. *Nature Communications*, 7, 2016.

[79] Abebe Reda Woldu, Zanling Huang, Pengxiang Zhao, Liangsheng Hu, and Didier Astruc. Electrochemical CO_2 reduction (CO_2RR) to multi-carbon products over copper-based catalysts. *Coordination Chemistry Reviews*, 454:214340, 2022.

[80] A. V. Chadwick and J. N. Sherwood. Point Defects in Molecular Solids. *Point Defects in Solids*, 85(8):441–475, 1975.

[81] Sayed Ali Akbar Razavi and Ali Morsali. Linker functionalized metal-organic frameworks. *Coordination Chemistry Reviews*, 399:213023, 2019.

[82] Ping Shao, Luocai Yi, Shumei Chen, Tianhua Zhou, and Jian Zhang. Metal-organic frameworks for electrochemical reduction of carbon dioxide: The role of metal centers. *Journal of Energy Chemistry*, 40:156–170, 2020.

[83] Yun-Nan Gong, Long Jiao, Yunyang Qian, Chun-Yang Pan, Lirong Zheng, Xuechao Cai, Bo Liu, Shu-Hong Yu, and Hai-Long Jiang. Regulating the coordination environment of mof-templated single-atom nickel electrocatalysts for boosting co2 reduction. *Angewandte Chemie*, 132(7):2727–2731, 2020.

[84] Long Jiao, Yang Wang, Hai-Long Jiang, and Qiang Xu. Metal–organic frameworks as platforms for catalytic applications. *Advanced Materials*, 30(37):1703663, 2018.

[85] Guorui Cai, Peng Yan, Liangliang Zhang, Hong-Cai Zhou, and Hai-Long Jiang. Metal–organic framework-based hierarchically porous materials: synthesis and applications. *Chemical Reviews*, 121(20):12278–12326, 2021.

[86] Chanderpratap Singh, Subhabrata Mukhopadhyay, and Idan Hod. Metal–organic framework derived nanomaterials for electrocatalysis: recent developments for CO2 and N2 reduction. *Nano Convergence*, 8(1):1–10, 2021.

[87] Pei Qin Liao, Jian Qiang Shen, and Jie Peng Zhang. Metal–organic frameworks for electrocatalysis. *Coordination Chemistry Reviews*, 373:22–48, 2018.

[88] Nikolay Kornienko, Yingbo Zhao, Christopher S. Kley, Chenhui Zhu, Dohyung Kim, Song Lin, Christopher J. Chang, Omar M. Yaghi, and Peidong Yang. Metal-Organic Frameworks for Electrocatalytic Reduction of Carbon Dioxide. *Journal of the American Chemical Society*, 137(44):14129–14135, 2015.

[89] Idan Hod, Matthew D. Sampson, Pravas Deria, Clifford P. Kubiak, Omar K. Farha, and Joseph T. Hupp. Fe-Porphyrin-Based Metal-Organic Framework Films as High-Surface Concentration, Heterogeneous Catalysts for Electrochemical Reduction of CO_2. *ACS Catalysis*, 5(11):6302–6309, 2015.

[90] R. Senthil Kumar, S. Senthil Kumar, and M. Anbu Kulandainathan. Highly selective electrochemical reduction of carbon dioxide using Cu based metal organic framework as an electrocatalyst. *Electrochemistry Communications*, 25(1):70–73, 2012.

[91] Liang Feng, Gregory S. Day, Kun Yu Wang, Shuai Yuan, and Hong Cai Zhou. Strategies for Pore Engineering in Zirconium Metal-Organic Frameworks. *Chem*, 6(11):2902–2923, 2020.

[92] Yong Peng, Soheila Sanati, Ali Morsali, and Hermenegildo García. Metal–organic frameworks as electrocatalysts. *Angewandte Chemie*, 135(9):e202214707, 2023.

[93] Nikolay Kornienko, Yingbo Zhao, Christopher S Kley, Chenhui Zhu, Dohyung Kim, Song Lin, Christopher J Chang, Omar M Yaghi, and Peidong Yang. Metal–organic frameworks for electrocatalytic reduction of carbon dioxide. *Journal of the American Chemical Society*, 137(44):14129–14135, 2015.

[94] Xing Zhang, Zishan Wu, Xiao Zhang, Liewu Li, Yanyan Li, Haomin Xu, Xiaoxiao Li, Xiaolu Yu, Zisheng Zhang, Yongye Liang, et al. Highly selective and active co2 reduction electrocatalysts based on cobalt phthalocyanine/carbon nanotube hybrid structures. *Nature communications*, 8(1):14675, 2017.

[95] Xinchen Kang, Qinggong Zhu, Xiaofu Sun, Jiayin Hu, Jianling Zhang, Zhimin Liu, and Buxing Han. Highly efficient electrochemical reduction of co 2 to ch 4 in an ionic liquid using a metal–organic framework cathode. *Chemical science*, 7(1):266–273, 2016.

[96] Bo You, Nan Jiang, Meili Sheng, Walter S Drisdell, Junko Yano, and Yujie Sun. Bimetal–organic framework self-adjusted synthesis of support-free nonprecious electrocatalysts for efficient oxygen reduction. *Acs Catalysis*, 5(12):7068–7076, 2015.

[97] Fuping Pan, Hanguang Zhang, Kexi Liu, David Cullen, Karren More, Maoyu Wang, Zhenxing Feng, Guofeng Wang, Gang Wu, and Ying Li. Unveiling active sites of co_2 reduction on nitrogen-coordinated and atomically dispersed iron and cobalt catalysts. *Acs Catalysis*, 8(4):3116–3122, 2018.

[98] Yuan Pan, Rui Lin, Yinjuan Chen, Shoujie Liu, Wei Zhu, Xing Cao, Wenxing Chen, Konglin Wu, Weng-Chon Cheong, Yu Wang, et al. Design of single-atom Co-N_5 catalytic site: a robust electrocatalyst for co_2 reduction with nearly 100% co selectivity and remarkable stability. *Journal of the American chemical society*, 140(12):4218–4221, 2018.

[99] Kyo Sung Park, Zheng Ni, Adrien P Côté, Jae Yong Choi, Rudan Huang, Fernando J Uribe-Romo, Hee K Chae, Michael O'Keeffe, and Omar M Yaghi. Exceptional chemical and thermal stability of zeolitic imidazolate frameworks. *Proceedings of the National Academy of Sciences*, 103(27):10186–10191, 2006.

[100] Liling Zhang, Gang Wu, and Jianwen Jiang. Adsorption and diffusion of CO_2 and CH_4 in zeolitic imidazolate framework-8: effect of structural flexibility. *The Journal of Physical Chemistry C*, 118(17):8788–8794, 2014.

[101] Surendar R. Venna and Moises A. Carreon. Highly permeable zeolite imidazolate framework-8 membranes for CO_2/CH_4 separation. *Journal of the American Chemical Society*, 132(1):76–78, 2010.

[102] Kangjie Zhang, Hailin Shang, Bin Li, Zhe Wang, Yuexiang Lu, and Xiangke Wang. Structural design of metal catalysts based on ZIFs: From nanoscale to atomic level. *Nano Select*, 2(10):1902–1925, 2021.

[103] Haoze Wang, Xiaokun Pei, Markus J Kalmutzki, Jingjing Yang, and Omar M Yaghi. Large cages of zeolitic imidazolate frameworks. *Accounts of Chemical Research*, 55(5):707–721, 2022.

[104] Yusuf Valentino Kaneti, Saikat Dutta, Md SA Hossain, Muhammad JA Shiddiky, Kuo-Lun Tung, Fa-Kuen Shieh, Chia-Kuang Tsung, Kevin C-W Wu, and Yusuke Yamauchi. Strategies for improving the functionality of zeolitic imidazolate frameworks: tailoring nanoarchitectures for functional applications. *Advanced Materials*, 29(38):1700213, 2017.

[105] Yulin Wang, Pengfei Hou, Zhuo Wang, and Peng Kang. Zinc imidazolate metal–organic frameworks (ZIF-8) for electrochemical reduction of CO_2 to CO. *ChemPhysChem*, 18(22):3142–3147, 2017.

[106] Xiaole Jiang, Haobo Li, Jianping Xiao, Dunfeng Gao, Rui Si, Fan Yang, Yanshuo Li, Guoxiong Wang, and Xinhe Bao. Carbon dioxide electroreduction over imidazolate ligands coordinated with Zn(II) center in ZIFs. *Nano Energy*, 52:345–350, 2018.

[107] Jens Kehlet Nørskov, Jan Rossmeisl, Ashildur Logadottir, LRKJ Lindqvist, John R Kitchin, Thomas Bligaard, and Hannes Jonsson. Origin of the overpotential for oxygen reduction at a fuel-cell cathode. *The Journal of Physical Chemistry B*, 108(46):17886–17892, 2004.

[108] Graeme Henkelman and Hannes Jónsson. A dimer method for finding saddle points on high dimensional potential surfaces using only first derivatives. *The Journal of chemical physics*, 111(15):7010–7022, 1999.

[109] Graeme Henkelman and Hannes Jónsson. Improved tangent estimate in the nudged elastic band method for finding minimum energy paths and saddle points. *The Journal of chemical physics*, 113(22):9978–9985, 2000.

[110] Graeme Henkelman, Blas P Uberuaga, and Hannes Jónsson. A climbing image nudged elastic band method for finding saddle points and minimum energy paths. *The Journal of chemical physics*, 113(22):9901–9904, 2000.

[111] M. Born and R. Oppenheimer. Zur quantentheorie der molekeln. *Annalen der Physik*, 389(20):457–484, 1927.

[112] E. Fermi. Un metodo statistico per la determinazione di alcune priorietá dell'atomo. *Rend. Accad. Naz. Lincei*, 6:602, 1927.

[113] L. H. Thomas. The calculation of atomic fields. *Proc. Cambridge Phil. Roy. Soc.*, 23:542, 1927.

[114] P. A. M. Dirac. Note on exchange phenomena in the Thomas-Fermi atom. *Proc. Cambridge Phil. Roy. Soc.*, 26:376, 1930.

[115] P. Hohenberg and W. Kohn. Inhomogeneous electron gas. *Phys. Rev.*, 136:B864–B871, Nov 1964.

[116] W. Kohn and L. J. Sham. Self-consistent equations including exchange and correlation effects. *Phys. Rev.*, 140:A1133–A1138, Nov 1965.

[117] John P. Perdew and Karla Schmidt. Jacob's ladder of density functional approximations for the exchange-correlation energy. *AIP Conference Proceedings*, 577(1):1–20, 2001.

[118] D. M. Ceperley and B. J. Alder. Ground state of the electron gas by a stochastic method. *Phys. Rev. Lett.*, 45:566–569, Aug 1980.

[119] J. P. Perdew and Alex Zunger. Self-interaction correction to density-functional approximations for many-electron systems. *Phys. Rev. B*, 23:5048–5079, May 1981.

[120] John P. Perdew and Wang Yue. Accurate and simple density functional for the electronic exchange energy: Generalized gradient approximation. *Phys. Rev. B*, 33:8800–8802, Jun 1986.

[121] John P. Perdew, Kieron Burke, and Matthias Ernzerhof. Generalized gradient approximation made simple. *Phys. Rev. Lett.*, 77:3865–3868, Oct 1996.

[122] Xiaowa Nie, Wenjia Luo, Michael J Janik, and Aravind Asthagiri. Reaction mechanisms of co2 electrochemical reduction on cu (1 1 1) determined with density functional theory. *Journal of catalysis*, 312:108–122, 2014.

[123] Jochen Heyd, Gustavo E Scuseria, and Matthias Ernzerhof. Hybrid functionals based on a screened coulomb potential. *The Journal of chemical physics*, 118(18):8207–8215, 2003.

[124] Jochen Heyd, Gustavo E. Scuseria, and Matthias Ernzerhof. Erratum: "Hybrid functionals based on a screened Coulomb potential" [J. Chem. Phys. 118, 8207 (2003)]. *The Journal of Chemical Physics*, 124(21), 06 2006. 219906.

[125] James C. Phillips and Leonard Kleinman. New method for calculating wave functions in crystals and molecules. *Phys. Rev.*, 116:287–294, Oct 1959.

[126] D. R.Hamann, M. Schlüter, and C. Chiang. Norm-conserving pseudopotentials. *Phys. Rev. Lett.*, 43:1494–1497, 1979.

[127] D. Vanderbilt. Soft self-consistent pseudopotentials in a generalized eigenvalue formalism. *Phys. Rev. B.*, 41:7892–7895, 1990.

[128] https://chem.libretexts.org/Bookshelves/Physical_and_Theoretical_Chemistry_Textbook_Maps/Physical_Chemistry_%28LibreTexts%29/30%3A_Gas-Phase_Reaction_Dynamics/30.10%3A_The_Potential-Energy_Surface_Can_Be_Calculated_Using_Quantum_Mechanics.

[129] Josiah Willard Gibbs. On the equilibrium of heterogeneous substances. *American Journal of Science*, 3(96):441–458, 1878.

[130] Long-Qing Chen. Chemical potential and gibbs free energy. *Mrs Bulletin*, 44(7):520–523, 2019.

[131] Daniel Richard Stull. *JANAF Thermochemical Tables*, volume 1. Clearinghouse, 1965.

[132] Peter J Linstrom and William G Mallard. The nist chemistry webbook: A chemical data resource on the internet. *Journal of Chemical & Engineering Data*, 46(5):1059–1063, 2001.

[133] Maxime Van den Bossche, Egill Skúlason, Christoph Rose-Petruck, and Hannes Jónsson. Assessment of constant-potential implicit solvation calculations of electrochemical energy barriers for h2 evolution on pt. *The Journal of Physical Chemistry C*, 123(7):4116–4124, 2019.

[134] Kiran Mathew, Ravishankar Sundararaman, Kendra Letchworth-Weaver, TA Arias, and Richard G Hennig. Implicit solvation model for density-functional study of nanocrystal surfaces and reaction pathways. *The Journal of chemical physics*, 140(8):084106, 2014.

[135] Kiran Mathew, Richard G Hennig, et al. Implicit self-consistent description of electrolyte in plane-wave density-functional theory. *arXiv preprint arXiv:1601.03346*, 1601:03346, 2016.

[136] Liang An and R Chen. Direct formate fuel cells: A review. *Journal of power sources*, 320:127–139, 2016.

[137] Hyun Ju Lee, Dong-Chang Kang, Seung Hee Pyen, Mi Shin, Young-Woong Suh, Haksoo Han, and Chae-Ho Shin. Production of H_2-free co by decomposition of formic acid over ZrO_2 catalysts. *Applied Catalysis A: General*, 531:13–20, 2017.

[138] Junli Wang, Xiumin Li, Junlan Zheng, Ji Cao, Xiaogang Hao, Zhongde Wang, Abuliti Abudula, and Guoqing Guan. Non-precious molybdenum-based catalyst derived from biomass: CO-free hydrogen production from formic acid at low temperature. *Energy Conversion and Management*, 164:122–131, 2018.

[139] Louis Schlapbach and Andreas Züttel. Hydrogen-storage materials for mobile applications. *Nature*, 414(6861):353–358, 2001.

[140] Qingqing Li, Xufeng Rao, Jiawei Sheng, Jie Xu, Jin Yi, Yuyu Liu, and Jiujun Zhang. Energy storage through CO_2 electroreduction: A brief review of advanced sn-based electrocatalysts and electrodes. *Journal of CO2 Utilization*, 27:48–59, 2018.

[141] Shulin Zhao, Sheng Li, Tao Guo, Shuaishuai Zhang, Jing Wang, Yuping Wu, and Yuhui Chen. Advances in Sn-based catalysts for electrochemical CO_2 reduction. *Nano-Micro Letters*, 11:1–19, 2019.

[142] Jeremy T Feaster, Chuan Shi, Etosha R Cave, Toru Hatsukade, David N Abram, Kendra P Kuhl, Christopher Hahn, Jens K Nørskov, and Thomas F Jaramillo. Understanding selectivity for the electrochemical reduction of carbon dioxide to formic acid and carbon monoxide on metal electrodes. *Acs Catalysis*, 7(7):4822–4827, 2017.

[143] Christina W Li and Matthew W Kanan. CO_2 reduction at low overpotential on cu electrodes resulting from the reduction of thick Cu_2O films. *Journal of the American Chemical Society*, 134(17):7231–7234, 2012.

[144] Recep Kas, Ruud Kortlever, Alexander Milbrat, Marc TM Koper, Guido Mul, and Jonas Baltrusaitis. Electrochemical CO_2 reduction on Cu_2O-derived copper nanoparticles: controlling the catalytic selectivity of hydrocarbons. *Physical Chemistry Chemical Physics*, 16(24):12194–12201, 2014.

[145] Fengwang Li, Lu Chen, Gregory P Knowles, Douglas R MacFarlane, and Jie Zhang. Hierarchical mesoporous SnO_2 nanosheets on carbon cloth: a robust and flexible electrocatalyst for CO_2 reduction with high efficiency and selectivity. *Angewandte chemie international edition*, 56(2):505–509, 2017.

[146] Kang-Sahn Kim, Won June Kim, Hyung-Kyu Lim, Eok Kyun Lee, and Hyungjun Kim. Tuned chemical bonding ability of Au at grain boundaries for enhanced electrochemical CO_2 reduction. *ACS Catalysis*, 6(7):4443–4448, 2016.

[147] Cunku Dong, Jianyu Fu, Hui Liu, Tao Ling, Jing Yang, Shi Zhang Qiao, and Xi-Wen Du. Tuning the selectivity and activity of Au catalysts for carbon dioxide electroreduction via grain boundary engineering: a DFT study. *Journal of Materials Chemistry A*, 5(15):7184–7190, 2017.

[148] Bijandra Kumar, Veerendra Atla, J Patrick Brian, Sudesh Kumari, Tu Quang Nguyen, Mahendra Sunkara, and Joshua M Spurgeon. Reduced SnO2 porous nanowires with a high density of grain boundaries as catalysts for efficient electrochemical CO_2-into-HCOOH conversion. *Angewandte Chemie International Edition*, 56(13):3645–3649, 2017.

[149] M Pourbaix. Atlas of electrochemical equilibria in aqueous solutions. Houston: NACE International. In *Mater. Sci. Forum*, pages 43–54, 1974.

[150] Na Han, Pan Ding, Le He, Youyong Li, and Yanguang Li. Promises of main group metal–based nanostructured materials for electrochemical CO_2 reduction to formate. *Advanced Energy Materials*, 10(11):1902338, 2020.

[151] Seunghwa Lee, Joey D. Ocon, Young Il Son, and Jaeyoung Lee. Alkaline CO_2 electrolysis toward selective and continuous $HCOO^-$ production over SnO_2 nanocatalysts. *Journal of Physical Chemistry C*, 119(9):4884–4890, 2015.

[152] Tengfei Gao, Anuj Kumar, Zhicheng Shang, Xinxuan Duan, Hangchao Wang, Shiyuan Wang, Shengfu Ji, Dongpeng Yan, Liang Luo, Wen Liu, and Xiaoming Sun. Promoting electrochemical conversion of CO_2 to formate with rich oxygen vacancies in nanoporous tin oxides. *Chinese Chemical Letters*, 30(12):2274–2278, 2019.

[153] Abhijit Dutta, Akiyoshi Kuzume, Motiar Rahaman, Soma Vesztergom, and Peter Broekmann. Monitoring the chemical state of catalysts for CO_2 electroreduction: an in operando study. *ACS Catalysis*, 5(12):7498–7502, 2015.

[154] A. Kuzume, A. Dutta, S. Vesztergom, and P. Broekmann. *Operando raman spectroscopy: Studies on the Reactivity and Stability of SnO_2 Nanoparticles During Electrochemical CO_2 Reduction Reaction*. Elsevier, 2018.

[155] Lulu Li, Zhi-Jian Zhao, Congling Hu, Piaoping Yang, Xintong Yuan, Yanan Wang, Lei Zhang, Lyudmila Moskaleva, and Jinlong Gong. Tuning oxygen vacancies of oxides to promote electrocatalytic reduction of carbon dioxide. *ACS Energy Letters*, 5(2):552–558, 2020.

[156] Chaonan Cui, Jinyu Han, Xinli Zhu, Xiao Liu, Hua Wang, Donghai Mei, and Qingfeng Ge. Promotional effect of surface hydroxyls on electrochemical reduction of CO_2 over SnO_x/Sn electrode. *Journal of Catalysis*, 343:257–265, 2016.

[157] Matthias Batzill and Ulrike Diebold. The surface and materials science of tin oxide. *Progress in surface science*, 79(2-4):47–154, 2005.

[158] Clara Salvini, Michele Re Fiorentin, Francesca Risplendi, Federico Raffone, and Giancarlo Cicero. Active surface structure of SnO_2 catalysts for CO_2 reduction revealed by ab initio simulations. *The Journal of Physical Chemistry C*, 126(34):14441–14447, 2022.

[159] Nicolas G Hörmann, Axel Gross, and Payam Kaghazchi. Semiconductor–metal transition induced by nanoscale stabilization. *Physical Chemistry Chemical Physics*, 17(8):5569–5573, 2015.

[160] Karolina Zalewska, Miguel M Santos, Hugo Cruz, and Luis C Branco. Photo-organocatalysis, photo-redox, and electro-organocatalysis processes. In *Recent Advances in Organocatalysis*. IntechOpen Rijeka, Croatia, 2016.

[161] Yuhang Wang, Junlang Liu, Yifei Wang, Abdullah M Al-Enizi, and Gengfeng Zheng. Tuning of co_2 reduction selectivity on metal electrocatalysts. *Small*, 13(43):1701809, 2017.

[162] Uttam R Pokharel, Frank R Fronczek, and Andrew W Maverick. Retracted article: Reduction of carbon dioxide to oxalate by a binuclear copper complex. *Nature communications*, 5(1):1–5, 2014.

[163] Kristian Torbensen, Dorian Joulié, Shaoxuan Ren, Min Wang, Danielle Salvatore, Curtis P Berlinguette, and Marc Robert. Molecular catalysts boost the rate of electrolytic CO_2 reduction. *ACS Energy Letters*, 5(5):1512–1518, 2020.

[164] Moran Feller, Urs Gellrich, Aviel Anaby, Yael Diskin-Posner, and David Milstein. Reductive cleavage of CO_2 by metal–ligand-cooperation mediated by an iridium pincer complex. *Journal of the American Chemical Society*, 138(20):6445–6454, 2016.

[165] Kallol Talukdar, Asala Issa, and Jonah W Jurss. Synthesis of a Redox-Active NNP-Type Pincer Ligand and Its Application Reduction With to Electrocatalytic First-Row Transition CO_2 Metal Complexes. *Molecular Catalysts for CO2 Fixation/Reduction*, 2020.

[166] Adrien J Göttle and Marc TM Koper. Determinant role of electrogenerated reactive nucleophilic species on selectivity during reduction of CO_2 catalyzed by metalloporphyrins. *Journal of the American Chemical Society*, 140(14):4826–4834, 2018.

[167] Susumu Kitagawa et al. Metal–organic frameworks (MOFs). *Chemical Society Reviews*, 43(16):5415–5418, 2014.

[168] Meili Ding, Xuechao Cai, and Hai-Long Jiang. Improving MOF stability: approaches and applications. *Chemical Science*, 10(44):10209–10230, 2019.

[169] Meili Ding, Robinson W Flaig, Hai-Long Jiang, and Omar M Yaghi. Carbon capture and conversion using metal–organic frameworks and MOF-based materials. *Chemical Society Reviews*, 48(10):2783–2828, 2019.

[170] Fayez Nasir Al-Rowaili, Umer Zahid, Sagheer Onaizi, Mazen Khaled, Aqil Jamal, and Eid M AL-Mutairi. A review for Metal-Organic Frameworks (MOFs) utilization in capture and conversion of carbon dioxide into valuable products. *Journal of CO2 Utilization*, 53:101715, 2021.

[171] Mengshuai Liu, Lin Liang, Xin Li, Xiangxiang Gao, and Jianmin Sun. Novel urea derivative-based ionic liquids with dual-functions: CO_2 capture and conversion under metal-and solvent-free conditions. *Green Chemistry*, 18(9):2851–2863, 2016.

[172] Mohammad Izadyar, Mojtaba Rezaeian, and Alexey Victorov. Theoretical study on the absorption of carbon dioxide by DBU-based ionic liquids. *Physical Chemistry Chemical Physics*, 22(35):20050–20060, 2020.

[173] Jikuan Qiu, Yuling Zhao, Zhiyong Li, Huiyong Wang, Maohong Fan, and Jianji Wang. Efficient ionic-liquid-promoted chemical fixation of CO_2 into α-alkylidene cyclic carbonates. *ChemSusChem*, 10(6):1120–1127, 2017.

[174] Xiao Zhu, Mengling Song, and Yingjie Xu. DBU-based protic ionic liquids for CO_2 capture. *ACS Sustainable Chemistry & Engineering*, 5(9):8192–8198, 2017.

[175] Wufeng Jiang, Xiaoshan Li, Ge Gao, Fan Wu, Cong Luo, and Liqi Zhang. Advances in applications of ionic liquids for phase change CO_2 capture. *Chemical Engineering Journal*, page 136767, 2022.

[176] Peng-Fei Liu, Kai Tao, Guo-Chang Li, Meng-Ke Wu, Shuai-Ru Zhu, Fei-Yan Yi, Wen-Na Zhao, and Lei Han. In situ growth of ZIF-8 nanocrystals on layered double hydroxide nanosheets for enhanced CO_2 capture. *Dalton Transactions*, 45(32):12632–12635, 2016.

[177] Liang Mu, Bei Liu, Huang Liu, Yuntao Yang, Changyu Sun, and Guangjin Chen. A novel method to improve the gas storage capacity of ZIF-8. *Journal of Materials Chemistry*, 22(24):12246–12252, 2012.

[178] Weixin Guan, Yan Dai, Chenyuan Dong, Xiaochen Yang, and Yuan Xi. Zeolite imidazolate framework (ZIF)-based mixed matrix membranes for CO_2 separation: A review. *Journal of Applied Polymer Science*, 137(33):48968, 2020.

[179] Renjie Zhang, Jie Yang, Xinbo Zhao, Han Yang, Hongping Li, Bairun Ji, Guangying Zhou, Xiaoxue Ma, and Dexin Yang. Electrochemical deposited zeolitic imidazolate frameworks as an efficient electrocatalyst for CO_2 electrocatalytic reduction. *ChemCatChem*, 14(4):e202101653, 2022.

[180] Céline Chizallet, Sandrine Lazare, Delphine Bazer-Bachi, Fabien Bonnier, Vincent Lecocq, Emmanuel Soyer, Anne-Agathe Quoineaud, and Nicolas Bats. Catalysis of transesterification by a nonfunctionalized metal-organic framework: acido-basicity at the external surface of ZIF-8 probed by FTIR and ab initio calculations. *Journal of the American Chemical Society*, 132(35):12365–12377, 2010.

[181] Céline Chizallet and Nicolas Bats. External surface of zeolite imidazolate frameworks viewed ab initio: multifunctionality at the organic- inorganic interface. *The Journal of Physical Chemistry Letters*, 1(1):349–353, 2010.

[182] Shuo Dou, Jiajia Song, Shibo Xi, Yonghua Du, Jiong Wang, Zhen-Feng Huang, Zhichuan J Xu, and Xin Wang. Boosting electrochemical CO_2 reduction on metal–organic frameworks via ligand doping. *Angewandte Chemie*, 131(12):4081–4085, 2019.

[183] Yichang Pan, Yunyang Liu, Gaofeng Zeng, Lan Zhao, and Zhiping Lai. Rapid synthesis of zeolitic imidazolate framework-8 (ZIF-8) nanocrystals in an aqueous system. *Chemical Communications*, 47(7):2071–2073, 2011.

[184] Simon H Pang, Chu Han, David S Sholl, Christopher W Jones, and Ryan P Lively. Facet-specific stability of ZIF-8 in the presence of acid gases dissolved in aqueous solutions. *Chemistry of Materials*, 28(19):6960–6967, 2016.

[185] Pak Y Moh, Pablo Cubillas, Michael W Anderson, and Martin P Attfield. Revelation of the molecular assembly of the nanoporous metal organic framework ZIF-8. *Journal of the American Chemical Society*, 133(34):13304–13307, 2011.

[186] Yihan Zhu, Jim Ciston, Bin Zheng, Xiaohe Miao, Cory Czarnik, Yichang Pan, Rachid Sougrat, Zhiping Lai, Chia-En Hsiung, Kexin Yao, et al. Unravelling surface and interfacial structures of a metal–organic framework by transmission electron microscopy. *Nature materials*, 16(5):532–536, 2017.

[187] Tingting Weng and JR Schmidt. Structure and thermodynamic stability of zeolitic imidazolate framework surfaces. *The Journal of Physical Chemistry C*, 124(2):1458–1468, 2019.

[188] Lei Cheng, Puxuan Yan, Xiulin Yang, Huahong Zou, Hu Yang, and Hong Liang. High conductivity, percolation behavior and dielectric relaxation of hybrid ZIF-8/CNT composites. *Journal of Alloys and Compounds*, 825:154132, 2020.

[189] Zhonghua Xiang, Zan Hu, Dapeng Cao, Wantai Yang, Jianmin Lu, Bingyong Han, and Wenchuan Wang. Metal–organic frameworks with incorporated carbon nanotubes: improving carbon dioxide and methane storage capacities by lithium doping. *Angewandte Chemie International Edition*, 50(2):491–494, 2011.

[190] James E Ellis, Zidao Zeng, Sean I Hwang, Shaobo Li, Tian-Yi Luo, Seth C Burkert, David L White, Nathaniel L Rosi, Jeremiah J Gassensmith, and Alexander Star. Growth of ZIF-8 on molecularly ordered 2-methylimidazole/single-walled carbon nanotubes to form highly porous, electrically conductive composites. *Chemical science*, 10(3):737–742, 2019.

[191] Daeok Kim, Dae Woo Kim, Won G Hong, and Ali Coskun. Graphene/ZIF-8 composites with tunable hierarchical porosity and electrical conductivity. *Journal of Materials Chemistry A*, 4(20):7710–7717, 2016.

[192] S Rathinavel, K Priyadharshini, and Dhananjaya Panda. A review on carbon nanotube: An overview of synthesis, properties, functionalization, characterization, and the application. *Materials Science and Engineering: B*, 268:115095, 2021.

[193] Israr Masood ul Hasan, Luwei Peng, Jianfeng Mao, Ruinan He, Yongxia Wang, Jing Fu, Nengneng Xu, and Jinli Qiao. Carbon-based metal-free catalysts for electrochemical CO_2 reduction: activity, selectivity, and stability. *Carbon Energy*, 3(1):24–49, 2021.

[194] Geonhui Lee, Yuguang C Li, Ji-Yong Kim, Tao Peng, Dae-Hyun Nam, Armin Sedighian Rasouli, Fengwang Li, Mingchuan Luo, Alexander H Ip, Young-Chang Joo, et al. Electrochemical upgrade of CO_2 from amine capture solution. *Nature Energy*, 6(1):46–53, 2021.

[195] Daniele Sassone, Sergio Bocchini, Marco Fontana, Clara Salvini, Giancarlo Cicero, Michele Re Fiorentin, Francesca Risplendi, Giulio Latini, M Amin Farkhondehfal, Fabrizio Pirri, et al. Imidazole-imidazolate pair as organo-electrocatalyst for CO_2 reduction on ZIF-8 material. *Applied Energy*, 324:119743, 2022.

[196] Denis Johnson, Eugenie Pranada, Ray Yoo, Ekenedilichukwu Uwadiunor, Bright Ngozichukwu, and Abdoulaye Djire. Review and perspective on transition metal electrocatalysts toward carbon-neutral energy. *Energy & Fuels*, 2023.

[197] Y Hori, K Kikuchi, and S Suzuki. Production of carbon monoxide and methane in electrochemical reduction of carbon dioxide at metal electrodes in aqueous hydrogen carbonate solution. *Chem. Lett*, 14:1695–1698, 1985.

[198] Kendra P Kuhl, Toru Hatsukade, Etosha R Cave, David N Abram, Jakob Kibsgaard, and Thomas F Jaramillo. Electrocatalytic conversion of carbon dioxide to methane and methanol on transition metal surfaces. *Journal of the American Chemical Society*, 136(40):14107–14113, 2014.

[199] Ichiro Oda, Hirohito Ogasawara, and Masatoki Ito. Carbon monoxide adsorption on copper and silver electrodes during carbon dioxide electroreduction studied by infrared reflection absorption spectroscopy and surface-enhanced raman spectroscopy. *Langmuir*, 12(4):1094–1097, 1996.

[200] Nienke J Firet and Wilson A Smith. Probing the reaction mechanism of CO_2 electroreduction over Ag films via operando infrared spectroscopy. *Acs Catalysis*, 7(1):606–612, 2017.

[201] Shangqian Zhu, Tiehuai Li, Wen-Bin Cai, and Minhua Shao. CO_2 electrochemical reduction as probed through infrared spectroscopy. *ACS Energy Letters*, 4(3):682–689, 2019.

[202] Kun Jiang, Han Wang, Wen-Bin Cai, and Haotian Wang. Li electrochemical tuning of metal oxide for highly selective CO_2 reduction. *ACS nano*, 11(6):6451–6458, 2017.

[203] Toru Hatsukade, Kendra P Kuhl, Etosha R Cave, David N Abram, and Thomas F Jaramillo. Insights into the electrocatalytic reduction of CO_2 on metallic silver surfaces. *Physical Chemistry Chemical Physics*, 16(27):13814–13819, 2014.

[204] Toru Hatsukade, Kendra P Kuhl, Etosha R Cave, David N Abram, Jeremy T Feaster, Anna L Jongerius, Christopher Hahn, and Thomas F Jaramillo. Carbon dioxide electroreduction using a silver–zinc alloy. *Energy Technology*, 5(6):955–961, 2017.

[205] Nagahiro Hoshi, Makiko Kato, and Yoshio Hori. Electrochemical reduction of CO_2 on single crystal electrodes of silver Ag(111), Ag(100) and Ag(110). *Journal of electroanalytical chemistry*, 440(1-2):283–286, 1997.

[206] Jonathan Rosen, Gregory S Hutchings, Qi Lu, Sean Rivera, Yang Zhou, Dionisios G Vlachos, and Feng Jiao. Mechanistic insights into the electrochemical reduction of CO_2 to CO on nanostructured Ag surfaces. *Acs Catalysis*, 5(7):4293–4299, 2015.

[207] Ezra L Clark, Stefan Ringe, Michael Tang, Amber Walton, Christopher Hahn, Thomas F Jaramillo, Karen Chan, and Alexis T Bell. Influence of Atomic Surface Structure on the Activity of Ag for the Electrochemical Reduction of CO_2 to CO. *ACS catalysis*, 9(5):4006–4014, 2019.

[208] Da Hye Won, Hyeyoung Shin, Jaekang Koh, Jaehoon Chung, Hee Sang Lee, Hyungjun Kim, and Seong Ihl Woo. Highly efficient, selective, and stable CO_2 electroreduction on a hexagonal Zn catalyst. *Angewandte Chemie*, 128(32):9443–9446, 2016.

[209] Binhao Qin, Yuhang Li, Hongquan Fu, Hongjuan Wang, Shengzhou Chen, Zili Liu, and Feng Peng. Electrochemical reduction of CO_2 into tunable syngas production by regulating the crystal facets of earth-abundant Zn catalyst. *ACS applied materials & interfaces*, 10(24):20530–20539, 2018.

[210] Jing Xiao, Min-Rui Gao, Subiao Liu, and Jing-Li Luo. Hexagonal Zn nanoplates enclosed by Zn(100) and Zn(002) facets for highly selective CO_2 electroreduction to CO. *ACS applied materials & interfaces*, 12(28):31431–31438, 2020.

[211] Jong Suk Yoo, Rune Christensen, Tejs Vegge, Jens K Nørskov, and Felix Studt. Theoretical insight into the trends that guide the electrochemical reduction of carbon dioxide to formic acid. *ChemSusChem*, 9(4):358–363, 2016.

[212] William J Durand, Andrew A Peterson, Felix Studt, Frank Abild-Pedersen, and Jens K Nørskov. Structure effects on the energetics of the electrochemical reduction of CO_2 by copper surfaces. *Surface Science*, 605(15-16):1354–1359, 2011.

[213] Maxime Van den Bossche, Christoph Rose-Petruck, and Hannes Jonsson. Competing HCOOH and CO Pathways in CO_2 Electroreduction at Copper Electrodes: Calculations of Voltage-Dependent Activation Energy. *The Journal of Physical Chemistry C*, 125(25):13802–13808, 2021.

[214] Michael T Tang, Xinyan Liu, Yongfei Ji, Jens K Norskov, and Karen Chan. Modeling hydrogen evolution reaction kinetics through explicit water–metal interfaces. *The Journal of Physical Chemistry C*, 124(51):28083–28092, 2020.

[215] Manfred Eigen. Proton transfer, acid-base catalysis, and enzymatic hydrolysis. Part I: elementary processes. *Angewandte Chemie International Edition in English*, 3(1):1–19, 1964.

[216] R Parthasarathi, V Subramanian, and N Sathyamurthy. Hydrogen bonding in protonated water clusters: an atoms-in-molecules perspective. *The Journal of Physical Chemistry A*, 111(51):13287–13290, 2007.

[217] Amin Salehi-Khojin, Huei-Ru Molly Jhong, Brian A Rosen, Wei Zhu, Sichao Ma, Paul JA Kenis, and Richard I Masel. Nanoparticle silver catalysts that show enhanced activity for carbon dioxide electrolysis. *The Journal of Physical Chemistry C*, 117(4):1627–1632, 2013.

[218] Xingyi Deng, Dominic Alfonso, Thuy-Duong Nguyen-Phan, and Douglas R Kauffman. Resolving the Size-Dependent Transition between CO_2 Reduction Reaction and H_2 Evolution Reaction Selectivity in Sub-5 nm Silver Nanoparticle Electrocatalysts. *ACS Catalysis*, 12(10):5921–5929, 2022.

[219] Seoin Back, Min Sun Yeom, and Yousung Jung. Active sites of Au and Ag nanoparticle catalysts for CO_2 electroreduction to CO. *Acs Catalysis*, 5(9):5089–5096, 2015.

[220] Mireille Ghoussoub. *First principles investigation of heterogeneous catalysis on metal oxide surfaces*. University of Toronto (Canada), 2016.

[221] Andrew A Peterson, Frank Abild-Pedersen, Felix Studt, Jan Rossmeisl, and Jens K Nørskov. How copper catalyzes the electroreduction of carbon dioxide into hydrocarbon fuels. *Energy & Environmental Science*, 3(9):1311–1315, 2010.

[222] Vladimir Tripkovic, Marco Vanin, Mohammedreza Karamad, Mårten E Björketun, Karsten W Jacobsen, Kristian S Thygesen, and Jan Rossmeisl. Electrochemical CO_2 and CO reduction on metal-functionalized porphyrin-like graphene. *The Journal of Physical Chemistry C*, 117(18):9187–9195, 2013.

[223] Federico Calle-Vallejo and Marc TM Koper. Theoretical considerations on the electroreduction of CO to C_2 species on Cu(100) electrodes. *Angewandte Chemie*, 125(28):7423–7426, 2013.

[224] Paolo Giannozzi, Stefano Baroni, Nicola Bonini, Matteo Calandra, Roberto Car, Carlo Cavazzoni, Davide Ceresoli, Guido L Chiarotti, Matteo Cococcioni, Ismaila Dabo, et al. QUANTUM ESPRESSO: a modular and open-source software project for quantum simulations of materials. *Journal of physics: Condensed matter*, 21(39):395502, 2009.

[225] Paolo Giannozzi, Oliviero Andreussi, Thomas Brumme, Oana Bunau, M Buongiorno Nardelli, Matteo Calandra, Roberto Car, Carlo Cavazzoni, Davide Ceresoli, Matteo Cococcioni, et al. Advanced capabilities for materials modelling with Quantum ESPRESSO. *Journal of physics: Condensed matter*, 29(46):465901, 2017.

[226] Georg Kresse and Jürgen Hafner. Ab initio molecular dynamics for liquid metals. *Physical review B*, 47(1):558, 1993.

[227] Georg Kresse and Jürgen Hafner. Ab initio molecular-dynamics simulation of the liquid-metal–amorphous-semiconductor transition in germanium. *Physical Review B*, 49(20):14251, 1994.

[228] Georg Kresse and Jürgen Furthmüller. Efficient iterative schemes for ab initio total-energy calculations using a plane-wave basis set. *Physical review B*, 54(16):11169, 1996.

[229] John P Perdew, Kieron Burke, and Matthias Ernzerhof. Generalized gradient approximation made simple. *Physical review letters*, 77(18):3865, 1996.

[230] Kevin F Garrity, Joseph W Bennett, Karin M Rabe, and David Vanderbilt. Pseudopotentials for high-throughput dft calculations. *Computational Materials Science*, 81:446–452, 2014.

[231] J Oviedo and MJ Gillan. The energetics and structure of oxygen vacancies on the SnO_2(110) surface. *Surface science*, 467(1-3):35–48, 2000.

[232] Ralph Walter Graystone Wyckoff and Ralph WG Wyckoff. *Crystal structures*, volume 1. Interscience publishers New York, 1963.

[233] Hendrik J Monkhorst and James D Pack. Special points for brillouin-zone integrations. *Physical review B*, 13(12):5188, 1976.

[234] J Oviedo and MJ Gillan. Energetics and structure of stoichiometric SnO_2 surfaces studied by first-principles calculations. *Surface Science*, 463(2):93–101, 2000.

[235] Francesca Risplendi, Michele Re Fiorentin, and Giancarlo Cicero. Unravelling electrocatalytic properties of metal porphyrin-like complexes hosted in graphene matrices. *2D Materials*, 7(2):025017, 2020.

[236] David Vanderbilt. Soft self-consistent pseudopotentials in a generalized eigenvalue formalism. *Physical review B*, 41(11):7892, 1990.

[237] Alejandra Rendón-Calle, Santiago Builes, and Federico Calle-Vallejo. Substantial improvement of electrocatalytic predictions by systematic assessment of solvent effects on adsorption energies. *Applied Catalysis B: Environmental*, 276:119147, 2020.

[238] BHLB Hammer, Lars Bruno Hansen, and Jens Kehlet Nørskov. Improved adsorption energetics within density-functional theory using revised perdew-burke-ernzerhof functionals. *Physical review B*, 59(11):7413, 1999.

[239] Javed Hussain, Hannes Jónsson, and Egill Skúlason. Calculations of product selectivity in electrochemical co_2 reduction. *Acs Catalysis*, 8(6):5240–5249, 2018.

[240] Guisen Liu, Jian Wang, and Yao Shen. Density functional theory study of $\{10\bar{1}n\}$ twin boundaries of Zn under high pressure. *Computational Materials Science*, 151:106–116, 2018.

APPENDIX A

Theoretical methods

In Section A.1, the method employed to correct the electronic energy of molecules is presented, while Section A.2 discusses the estimation of the solvation energy by explicit solvent for the calculation of the Gibbs free energy. Section A.3 introduces the estimation of the chemical potential of both biatomic and poliatomic molecules. In Sections A.4 and A.5 show the calculations used to determine the surface phase diagram and the relative surface energy stability, respectively.

A.1 CO_2, CO and OCO-molecules energy correction

In Density Functional Theory, some functionals, such as PBE and RPBE, introduce systematic errors in the total energies of species containing double and triple bonds between carbon and oxygen, such as CO, CO_2, esters and carboxylic acids (OCO-molecules) [220–223]. To overcome this issue, we adopted a statistical correction strategy [221] based on reaction enthalpies (ΔH^r) and applied it to CO, CO_2, and OCO-species. We have chosen to compute the theoretical reaction enthalpy (ΔH^r_{theo}) of a set of reactions (r) which encloses reactions with: (i) CO and no OCO-molecules, (ii) CO_2 only, (iii) CO and an OCO-molecule,and (iv) CO_2 and an OCO-molecule. These reactions are reported below.

Reaction pathways with CO:

$$3\,H_2 + CO \longrightarrow CH_4 + H_2O \tag{A.1a}$$
$$2\,H_2 + CO \longrightarrow \frac{1}{2}C_2H_4 + H_2O \tag{A.1b}$$
$$\frac{5}{2}H_2 + CO \longrightarrow \frac{1}{2}C_2H_6 + H_2O \tag{A.1c}$$
$$\frac{7}{3}H_2 + CO \longrightarrow \frac{1}{3}C_3H_8 + H_2O \tag{A.1d}$$
$$\frac{7}{4}H_2 + CO \longrightarrow \frac{1}{4}CH_2CHCHCH_2 + H_2O \tag{A.1e}$$
$$2\,H_2 + CO \longrightarrow CH_3OH \tag{A.1f}$$
$$2\,H_2 + CO \longrightarrow \frac{1}{2}CH_3CH_2OH + \frac{1}{2}H_2O \tag{A.1g}$$
$$\frac{5}{3}H_2 + CO \longrightarrow \frac{1}{3}CH_3CH_2CHO + \frac{2}{3}H_2O \tag{A.1h}$$

Reaction pathways with CO_2:

$$4\,H_2 + CO_2 \longrightarrow CH_4 + 2\,H_2O \tag{A.2a}$$
$$3\,H_2 + CO_2 \longrightarrow \frac{1}{2}C_2H_4 + 2\,H_2O \tag{A.2b}$$
$$\frac{7}{2}H_2 + CO_2 \longrightarrow \frac{1}{2}C_2H_6 + 2\,H_2O \tag{A.2c}$$
$$\frac{10}{3}H_2 + CO_2 \longrightarrow \frac{1}{3}C_3H_8 + 2\,H_2O \tag{A.2d}$$
$$\frac{11}{4}H_2 + CO_2 \longrightarrow \frac{1}{4}CH_2CHCHCH_2 + 2\,H_2O \tag{A.2e}$$
$$3\,H_2 + CO_2 \longrightarrow CH_3OH + H_2O \tag{A.2f}$$
$$3\,H_2 + CO_2 \longrightarrow \frac{1}{2}CH_3CH_2OH + \frac{3}{2}H_2O \tag{A.2g}$$
$$\frac{8}{3}H_2 + CO_2 \longrightarrow \frac{1}{3}CH_3CH_2CHO + \frac{5}{3}H_2O \tag{A.2h}$$

Reaction pathways with CO and OCO-molecules:

$$H_2O + CO \longrightarrow HCOOH \tag{A.3a}$$
$$H_2 + CO \longrightarrow \frac{1}{2}C_2H_3COOH \tag{A.3b}$$
$$\frac{4}{3}H_2 + CO \longrightarrow \frac{1}{2}CH_3CH_2COOH + \frac{1}{3}H_2O \tag{A.3c}$$
$$\frac{3}{2}H_2 + CO \longrightarrow \frac{1}{4}CH_3CH_2CH_2COOH + \frac{1}{2}H_2O \tag{A.3d}$$
$$H_2 + CO \longrightarrow HCOOCH_3 \tag{A.3e}$$
$$\frac{4}{3}H_2 + CO \longrightarrow \frac{1}{3}HCOOCH_2CH_3 + \frac{1}{3}H2O \tag{A.3f}$$
$$\frac{4}{3}H_2 + CO \longrightarrow \frac{1}{3}CH_3COOCH_3 + \frac{1}{3}H_2O \tag{A.3g}$$
$$\frac{3}{2}H_2 + CO \longrightarrow \frac{1}{4}CH_3COOCH_2CH_3 + \frac{1}{2}H_2O \tag{A.3h}$$

Reaction pathways with CO_2 and OCO-molecules:

$$H_2 + CO_2 \longrightarrow HCOOH \tag{A.4a}$$
$$2H_2 + CO_2 \longrightarrow \frac{1}{2}C_2H_3COOH \tag{A.4b}$$
$$\frac{7}{3}H_2 + CO_2 \longrightarrow \frac{1}{3}CH_3CH_2COOH + \frac{4}{3}H_2O \tag{A.4c}$$
$$\frac{5}{2}H_2 + CO_2 \longrightarrow \frac{1}{4}CH_3CH_2CH_2COOH + \frac{3}{2}H_2O \tag{A.4d}$$
$$2H_2 + CO_2 \longrightarrow \frac{1}{2}HCOOCH_3 + H_2O \tag{A.4e}$$
$$\frac{7}{3}H_2 + CO_2 \longrightarrow \frac{1}{3}HCOOCH_2CH_3 + \frac{4}{3}H2O \tag{A.4f}$$
$$\frac{7}{3}H_2 + CO_2 \longrightarrow \frac{1}{3}CH_3COOCH_3 + \frac{4}{3}H_2O \tag{A.4g}$$
$$\frac{5}{2}H_2 + CO_2 \longrightarrow \frac{1}{4}CH_3COOCH_2CH_3 + \frac{3}{2}H_2O \tag{A.4h}$$

We considered all molecules in their gas phase. For each reaction, we compared the $\Delta H^r_{theo,i}$ of the *i*th-reaction to the respective experimental result ($\Delta H^r_{exp,i}$) and calculated the absolute error $|\Delta H^r_{exp,i} - \Delta H^r_{theo,i}|$.
To compensate for these systematic errors, we introduced a correction to the total energy of CO (γ_{CO}), CO_2 (γ_{CO2}) and OCO-molecules (γ_{OCO}). The value of these

corrections can be obtained by

$$\Omega(\gamma_{CO}, \gamma_{CO2}, \gamma_{OCO}) = \sum_{i}^{N_r} |\Delta H^r_{exp,i} - \Delta H^r_{theo,i}(\gamma_{CO}, \gamma_{CO2}, \gamma_{OCO})| \tag{A.5}$$

where is required the minimisation of the total absolute error of the whole set of reactions. According to the theoretical investigation performed, the corrections values calculated depend on both the functional and the pseudopotentials employed.

A.2 Evaluation of solvation energy

For the calculations performed in Chapter 4, since all reactions take place in an aqueous environment, the contribution of the interaction with the solvent to the energy of the catalyst surface and its adsorbates, named solvation energy (E^{solv}), was computed by means of DFT simulations. In order to estimate this quantity, we used an explicit solvent model, calculating the binding energy of the bare surface and the adsorbate with the maximum number of water molecules that can bind through hydrogen bonds, both in the acceptor and donor configurations. For each system studied, the first and second hydration shells were recreated by the addition of n water molecules (n·H2O) which surround the active site and adsorbates. During the geometry optimization, only water molecules were free to fully relax, and the solvation correction for configuration i (E^{solv}_i) was calculated as:

$$E^{solv}_i = E^{DFT}_{i+n\cdot H2O} - (E^{DFT}_i + E^{DFT}_{n\cdot H2O}) \tag{A.6}$$

where $E^{DFT}_{i+n\cdot H2O}$ is the total energy DFT of the system including the solvent, while E^{DFT}_i and $E^{DFT}_{n\cdot H2O}$ are energies of the active site (or adsorbate) and the water cluster, respectively.

A.3 Computed chemical potential of polyatomic molecules

The chemical potential of a poliatomic molecule (μ_S) in gas phase can be theoretically predicted based on the ideal model, when experimental values are not tabulated. The

μ_S is defined as

$$\mu_S = \mu_S^\circ + \Delta\mu_S \tag{A.7}$$

where μ_S° is the chemical potential at standard conditions (T°298 K, p°=1 atm), while $\Delta\mu_S$ is the relative chemical potential. The expressions of these two last terms are

$$\mu_S^\circ = \mu_S^{ele} + \mu_S^{vib} + \mu_S^{tran} + \mu_S^{rot}, \tag{A.8}$$

$$\Delta\mu_S = RT \ln \frac{p_{vap}}{p\circ}, \tag{A.9}$$

where p is the vapor pressure, while μ_S^{ele}, μ_S^{vib}, μ_S^{tran}, and μ_S^{rot} represent the electronic, vibration, translational, and rotational chemical potentials, respectively.
The μ_S^{ele} corresponds to the electronic energy of the molecule estimated performing DFT calculations (E_S^{DFT}), while the remaining contributions to the standard chemical potential μ_S° were evaluated according to the following equations

$$\mu_S^{vib} = \sum_{i=1}^{M} \{\frac{\hbar\omega_i}{2} + K_B T \ln[1 - \exp(-\frac{\hbar\omega_i}{K_B T})]\}, \tag{A.10}$$

$$\mu_S^{tran} = K_B T \ln[(\frac{2\pi m}{h^2})^{\frac{3}{2}} \frac{(K_B T)^{\frac{5}{2}}}{p}], \tag{A.11}$$

$$\mu_S^{rot} = -K_B T \{\log \frac{\pi^2}{\sigma} + \frac{1}{2} \log[(\frac{8\pi^2 K_B T}{h^2})^3 \cdot I_A \cdot I_B \cdot I_C]\}. \tag{A.12}$$

H>ere the h, $\hbar$, ω_i, and K_B are the Planck constant, reduced Planck constant, normal modes, and Boltzmann constant, respectively. The σ term is the symmetry group of the molecule S and corresponds to the number of indistinguishable orientations of the chemical species. Finally, I is the moment of inertia $I = \sum_{j=1}^{n} m_j d_j^2$, where d_j is the distance of the j-th nucleus from the centre of mass of the molecule.

A.4 Calculation of surface phase diagram

The construction of the phase diagram requires relative surface energies calculated respect to a reference surface ($\Delta\gamma$), considering only charge neutral surface terminations.
In the case of ZIF-8(110) facet, the surface relative energies have been calculated for

the outermost terminations labeled as '$surf_{n/m}$', where (n) and (m) are the number of organic and solvent linkers, respectively. All the surfaces investigated are characterized by the same surface area (A). The reference surface corresponds to the one which exposes both one Im/Im^- pair and one H_2O/OH^- couple, that is the $surf_{2/2}$.

In the gas-phase, the relative surface energy ($\Delta\gamma(g)$) is

$$\Delta\gamma(g) = \frac{1}{A}(G_{surf_{n/m}} - G_{surf_{2/2}} - \Delta N_{Im} \cdot \mu_{Im}(g) - \Delta N_{H_2O} \cdot \mu_{H_2O}(g)), \tag{A.13}$$

where $G_{surf_{n/m}}$ and $G_{surf_{2/2}}$ are the Gibbs free energy of the investigated and reference surfaces, respectively, computed by adding zero-point and entropy contributions. The excess of Im and H_2O molecules with respect to $surf_{2/2}$ are represented by ΔN_{Im} and ΔN_{H_2O}, and μ_{Im}/μ_{H_2O} are the Im and H_2O chemical potentials.

To obtain the solution phase relative surface free energies ($\Delta\gamma(aq)$), a dilute aqueous solution was considered, where the majority species is H_2O and its aqueous chemical potential is approximated to a water solution 55 M $\mu_{H_2O}(aq, 55M)$ computed with the experimental vapor pressure

$$\mu_{H_2O}(aq, 55M) = \mu_{H_2O}(p = 1atm) + RT \ln \frac{p_{vap}}{p^\circ}, \tag{A.14}$$

where p_{vap} is measured liquid water pressure at 298 K equal to 0.031 atm.

The expression for $\Delta\gamma(aq)$ is

$$\Delta\gamma(aq) = \frac{1}{A}(G_{surf_{n/m}} - G_{surf_{2/2}} - \Delta N_{Im} \cdot \mu_{Im}(aq) - \Delta N_{H_2O} \cdot \mu_{H_2O}(aq, 55M)), \tag{A.15}$$

where the Im chemical potential $\mu_{Im}(aq)$ is defined as

$$\mu_{Im}(aq) = \mu^\circ_{Im}(c = 1M) + \Delta\mu_{Im}(c), \tag{A.16}$$

namely the sum of the contribution coming from the the standard chemical potential in aqueous solutions (μ°_{Im}(c = 1 M)), calculated as presented in section A.3 using a p_{vap} equal to $1.97 \cdot 10^{-5}$ atm, and the relative chemical potential ($\Delta\mu_{Im}(c)$).

A.5 Calculation of relative surface energy stability

In Chapter 3, the surface energies (γ) are computed for different surface structures and compositions of SnO_2. These γ are functions of the chemical potential (μ) and are expressed as

$$\gamma(\mu_i) = \frac{1}{2A}(G_{surf} - \sum N_i \mu_i(T,p)) \tag{A.17}$$

where G_{surf} is the total DFT energy of the symmetric slab with surface area A. The factor $\frac{1}{2A}$ is the reciprocal of the total in-plane surface area of the model taking into account a symmetric slab. The term $\mu_i(p_i,T)$ is the chemical potential of the species i present in the surface, while N_i is the respective number of i atoms belonging to the system. Precisely, species i are Sn and O. Consequently, Eq. A.17 becomes

$$\gamma(\mu_{Sn},\mu_O) = \frac{1}{2A}(G_{surf} - N_{Sn}\mu_{Sn} - N_O\mu_O) \tag{A.18}$$

where μ_O is

$$\mu_O = \frac{1}{2}\mu_{O_2} \tag{A.19}$$

and assuming the thermodynamic equilibrium with SnO_2 bulk, the following relationship is yielded:

$$\mu_O + \mu_{Sn} = g_{SnO_2}. \tag{A.20}$$

In Eq. A.20, g_{SnO_2} is the Gibbs free energy for the bulk oxide and Eq. A.18 is finally rewritten as

$$\gamma(\mu_{Sn},\mu_O) = \frac{1}{2A}(G_{surf} - N_{Sn}(g_{SnO_2} - 2\mu_O) - N_O\mu_O). \tag{A.21}$$

APPENDIX B

Computational details

Section B.1 presents a short introduction about the two software employed in this work, that is QUANTUM ESPRESSO and VASP packages, followed by the computational details of the performed DFT calculations. Section B.2 reports the theoretical method used in Chapter 3, while Sections B.3 and B.4 discuss the methods of Chapters 4 and 5, respectively.

B.1 Quantum ESPRESSO and VASP software

The QUANTUM ESPRESSO (QE) package [224, 225] is an integrated tool of computer codes for the calculations of electronic-structure and materials modeling at the nanoscale. The QE code is based on DFT, PWs and PPs, and its acronym ESPRESSO stands for *opEn Source Package for Research in Electronic Structure, Simulation, and Optimization*.
the package is divided into several executable, performing different types of calculations and one of its functionalities is the *Plane-Wave Self-Consistent Field* (PWscf) package, developed to simulate periodic systems by the expansion of Bloch functions in PWs, whose number is defined fixing the energy cutoff (E_{cutoff}). The employment of periodic boundary conditions allows for straightforward treatment of infinite crystalline systems, and an efficient convergence to the thermodynamic limit for aperiodic but extended systems, such as liquids or amorphous materials, whereas supercells allow to study finite systems. For a given periodic crystal defined by a Bravais lattice

and space group symmetry, the *PWscf* code computes its total energy, electronic band structure, and electronic charge density. During the development of this thesis, we have employed *PWscf* to predict the structures of simulating electrode surfaces, starting from their respective bulk optimization, and the adsorption of molecules involved in electrochemical reactions, while the computation of band structures and charge densities allow to predict the electronic properties of the materials.

Part of the DFT calculations carried out in this work have been performed with the Vienna *Ab-initio* Simulation Package (VASP) [226–228]. This computer tool was employed to perform DFT simulations, where the crystalline orbitals are represented as linear combination of plane wave basis set. Plane waves cannot describe properly core electrons, so the projector-augmented wave (PAW) pseudopotentials were used to describe inner electron shells and plane waves for valance electrons. Static simulations, such as geometry optimization, dimer and frequency calculations have been performed including implicit solvent effect by means of VASPsol module [134, 135] as well as NEB calculations to investigate transition state along reaction pathways.

B.2 Calculation of SnO_2 surfaces

The theoretical predictions about SnO_2 electrode modeling are based on DFT calculations performed with the QE package (section B.1). The Kohn-Sham equations are solved employing the Perdew-Burke-Ernzerhof (PBE) functional [229] to describe the exchange-correlation effects and ultrasoft pseudopotentials [230] to describe the electron-ion interaction. A plane-wave basis set with 38 Ry (380 Ry) cutoff was employed to represent the electronic wave functions (densities). All structures were relaxed by minimizing the atomic forces; the convergence threshold of energy and forces was set to 10^{-5} Ry and 10^{-4} Ry/Bohr, respectively. The rutile bulk of cassarite SnO_2 belongs to the P42/mnm tetragonal space group ($a = b \neq c$, $\alpha = \beta = \gamma$), corresponding to the number 136 in the standard listing. In the bulk, Sn atoms are hexacoordinated by O atoms, whose four *equatorial* lie in the same plane of Sn species, while the two *apical* are placed at the vertices of the octahedron. The final bulk-optimized lattice cell parameters are $a = b = 4.83$ Å and $c = 3.24$ Å, in agreement with previously published experimental and theoretical data within

2% variations [231, 232]. The Brillouin zone was sampled employing a 6×6×6 Monkhorst-Pack mesh [233] for the bulk calculations and reduced grids for surface calculations (4×3×1). From the crystal bulk structure, crystalline periodic slab models for nonpolar (110) surface was built, which is known from the literature as the thermodynamically most stable low-index SnO_2 surface [234]. The analysis of the computed surface energies showed that the 7-layer slab model is the best compromise between accurancy and computational costs. Each layer corresponds to one SnO_2 unit. The (110) facet presents a flat morphology with pentacoordinated Sn atoms and bivalent O species in the outermost positions of the slab, which correspond to Lewis acidic and Brônsted basic sites, respectively, whereas the internal portion of the slab present bulk structure. To study the electrode reactivity, the asymmetric 2×2 supercell (a = 13.67 Å and b = 6.48 Å) of SnO_2(110) slab composed of four atomic layers was employed, where the atoms belonging to the two bottom layers were kept fixed at their bulk positions. A vacuum layer in the direction perpendicular to the surface of 15 Åwas employed. To investigate the behavior of the proposed electrocatalyst, the Gibbs free energy profiles were calculated for the CO_2RR and compared with the competing HER and catalyst self-reduction reaction. Free energy profiles display the ΔG along the reduction reaction, from the reactants to the final products, through different intermediate states. The CHE proposed by Nørskov and collaborators was employed. The free energy profile determination and CHE method are discussed in Chapter 2, Section 2.5.2. The total energy calculation of species which contains double and triple bonds between carbon and oxygen contains systematic errors due to PBE functionals. Therefore, statistical corrections (γ_i) to CO_2, CO and OCO-molecules (reactants, intermediates, and products) were calculated according to the procedure presented in section A.1). The corrections applied are: -0.34 eV to CO, 0.19 eV to CO_2, and 0.17 eV to OCO-molecules. We assume that all reactions take place in an aqueous environment. In this perspective, we employed the contribution of the interaction with the solvent to the energy of the surface and its adsorbates including the solvation values of previous works [235].

B.3 Calculation of ZIF-8 and ZIF-8/CNT

The QE package (section B.1) was employed to perform the theoretical calculations based on DFT to investigate ZIF-8 electrocatalyst. To investigate ZIF-8 bulk and the corresponding (110) surface, all the calculations have been carried out with the PBE functional [229] and ultrasoft pseudopotentials [236] have been used to describe the electron–ion interaction. The cubic bulk of ZIF-8 belongs to the I-43m space group ($a = b = c$, $\alpha = \beta = \gamma$), corresponding to the number 217 in the standard listing. The final bulk-optimized lattice cell parameters are $a = b = c = 17.31$ Å and includes 276 atoms. The optimized ZIF-8 bulk was obtained by a full relaxation of both cell parameters and atom positions. The 2D slab ZIF-8(110) facet The ZIF – 8(110) surface ($a = 24.48$ Å and $b = 17.31$ Å) was built introducing a vacuum layer of 20 Å along the direction perpendicular to the surface to avoid undesired interactions between periodic replicas. The electrochemical performances of ZIF-8 compounds towards the CO_2RR were predicted determing the Gibbs free energy profiles of the reaction pathways according to the mechanisms proposed. The calculation of reaction ΔG were computed within the Computational Hydrogen Electrode (CHE) method proposed by Nørskov (Chapter 2, Section 2.5.2). For all the calculations, periodic boundary conditions are imposed and the Brillouin zone was sampled at the Γ point. A plane-wave energy cutoff of 28 Ry and 280 Ry were assumed for the wave functions and the electron densities, respectively, for all the calculations. The convergence of forces was set to 10^{-4} Ry/Bohr, while for the energy to 10^{-5} Ry. Because of PBE funcionals, systematic errors occur in the total energies of CO_2, CO and OCO-molecules. Therefore, statistical corrections to reactants, intermediates, and products containing OCO-species (single and triple bonds) were computed. The corrections applied are: -0.33 eV to CO, 0.092 eV to CO_2, and 0.066 eV to OCO-species. Finally, solvation energies were estimated for the ImH/Im^- and its adsorbates as reported A.2, while for the other species the solvation values were taken from previous works in literature [235, 237]. The final solvation energies for the bare ZIF-8 surface exposing ImH/Im^- pair, *COOH and *COO are -0.92 eV, -1.22 eV, and -1.16 eV, respectively, where the active site is represented by the *, that is the Im ligand belonging to the surface.

B.4 Calculation of metal Ag and Zn surfaces

The VASP package was employed to perform DFT electronic structure calculations coupled to the implicit solvation model described as a continuous polarizable medium by VASPsol extension of the VASP software (Section B.1). To investigate CO_2 reduction reaction (CO_2RR) and hydrogen evolution reaction (HER), the Kohn-Sham equations are solved employing the revised Perdew-Burke-Ernzerhof (RPBE) approximation [238]. A plane wave basis set is used with a kinetic energy cutoffof 350 eV and the standard set of projector augmented-wave 39 setups for H, C, O, Ag and Zn. The effect of counterions is included by a linearized Poisson-Boltzmann equation [133] and Debye length of 3 Å. The saddle points search was performed by the employment of the NEB and dimer methods (Section 2.5.3). Local energy minimization of are performed until the magnitude of the atomic forces drops below 0.05 eV/Å. The control of the applied potential was carried out employing the CEP model (Section 2.5.4). The crystal structure of Ag bulk is face-centerd cubic (fcc) and belongs to the $Fm\bar{3}m$ space group, corresponding to the number 225 in the standard listing. Each bulk Ag atom is surrounded by twelve equivalent Ag atoms placed ate the edge, face and corners of the crystal structure resulting in a $AgAg_{12}$ system. The optimized lattice constant ($a = b = c$) is 4.21 Å, in agreement with previous studies [239]. On the other hand, Zn crystallizes in a hexagonal-close packed lattice with space group $P6_3/mmc$ (number 194 of the standard list) with bulk coordination number 12: each Zn atom has six nearest neighbors in its own plane and six others out its own plane. The optimized lattice constants are $a = b = 2.63$ Å and $c = 5.14$ Å ($\alpha = \beta 90\circ$ and $\gamma = 120\circ$), in agreement with previously experimental and theoretical data [240]. Starting from the optimized silver bulk structure, the (111), (100) and (110) low index surfaces of Ag metal were generated, with 3×4, 3×3 and 2×4 supercells, respectively, of slab with a thickness of three atomic layers. The respective Monkhorst-Pack grids for the Brillouin zone integration are (4×3×1), (4×4×1), and (4×3×1). Regarding to zinc system, the 3×4 supercells for (0001) and $(10\bar{1}0)$ facets were built with a slab thickness of three atomic layers and the Monkhorst-Pack grid for the Brillouin zone integration is (4×3×1) for both surfaces. Generally, for all the surfaces, the atoms belonging to the two bottom layers were kept fixed at their bulk positions.